



Development of an image reconstruction method based on the detected X-ray fluorescence for sample analysis

Lara Hamawy

► To cite this version:

Lara Hamawy. Development of an image reconstruction method based on the detected X-ray fluorescence for sample analysis. Chemical and Process Engineering. Université de Grenoble; Université Libanaise, 2014. English. NNT : 2014GRENI080 . tel-01154253

HAL Id: tel-01154253

<https://theses.hal.science/tel-01154253>

Submitted on 21 May 2015

HAL is a multi-disciplinary open access archive for the deposit and dissemination of scientific research documents, whether they are published or not. The documents may come from teaching and research institutions in France or abroad, or from public or private research centers.

L'archive ouverte pluridisciplinaire **HAL**, est destinée au dépôt et à la diffusion de documents scientifiques de niveau recherche, publiés ou non, émanant des établissements d'enseignement et de recherche français ou étrangers, des laboratoires publics ou privés.



THÈSE

Pour obtenir le grade de

DOCTEUR DE L'UNIVERSITÉ DE GRENOBLE

Spécialité **Mécanique des Fluides, Procédés, Energétique**

Arrêté ministériel : 7 août 2006

Et de

LIU, LEBANESE INTERNATIONAL UNIVERSITY

Spécialité **Génie Biomédicale**

Présentée par

Lara HAMAWY

Thèse dirigée par « **Walid HASSAN** » et
codirigée par « **Stéphane BARRE** et **Samuel LEGOUPIL** »

préparée au sein du **Laboratoire des Ecoulements Géophysique et Industriel (LEGI)**
dans l'École Doctorale **IMEP2 Ingénierie, Matériaux, Mécanique, Énergétique, Environnement, Procédés, Production** et de **LIST-CEA**.

Développement d'une méthode de Reconstruction d'Image basée sur la Détection de la Fluorescence X pour l'Analyse d'Echantillon

Thèse soutenue publiquement le « **23 Octobre 2014** »,
devant le jury composé de :

Dr, Laurent, ORGEAS

Chercheur, CNRS/UDG, (Président)

Dr, Walid, HASSAN

Chercheur, Lebanese International University, (Membre)

Dr, Stéphane, BARRE

Chercheur, CNRS/UDG, (Membre)

Dr, Samuel, LEGOUPIL

Chercheur, CEA-Saclay, (Membre)

Prof, Françoise, PEYRIN

Chercheur, CREATIS-INSALyon, (Rapporteur)

Prof, Jamal, CHARARA

Chercheur, Université Libanaise-Liban, (Rapporteur)

Prof, Mahmoud, ELKOREK

Chercheur, Université Arabe de Beyrouth, (Membre)



Dedication:

This thesis is dedicated to my parents Georges & Mona & my siblings: Michel, Atbir & Hanadi who, from the beginning, shared and encouraged my enthusiasm for academic pursuits.

It is also dedicated to my husband Charbel who supported me each step of the way.

“Limitations live only in our minds. But if we use our imaginations, our possibilities become limitless.”

Jamie Paolinetti

Acknowledgments:

This thesis owes its existence to the help and support of many people. It is a pleasant aspect that I have the opportunity to express my gratitude for everyone who contributes meaningfully in its achievement.

In the first place, I am deeply indebted to my thesis supervisor Dr Walid Hassen, whose instructions and advices inspired my interest in the research and built a foresight capacity. His tremendous support has a major influence on this thesis.

Next, I would like to express my sincere appreciation and gratitude to Dr Stephane Barre for providing the opportunity to engage in this project. I am very grateful for his effort.

I also extend my appreciation for Dr Samuel Legoupil for his valuable assistance & collaboration in the research.

Besides, I would definitely like to thank the Reporters Prof Jamal Charara and Dr Françoise Peyrin for their valuable guidance in thesis writing. Also I would like to offer special thanks for the cooperation of the Jury members Dr Roland Orgeas & Prof Mahmoud Elkorek.

Finally, special recognition goes out to the "LIU, Lebanese International University", "UDG, Grenoble University" & "CEA, Atomic Energy Commission" for providing the optimum working environment.

Last but not least, "thanks be to God" who enlightens my ways and gives me the strength of will to accomplish this work.

Abstract

A new technique that localizes and identifies fluorescing elements in a sample was developed. This practical imaging modality employs a polychromatic X-ray source to irradiate the sample and prompts the fluorescence emission. Many factors affecting the whole system like attenuation, sample self-absorption, probability of fluorescence and Compton scattering were taken into account. Then, an effective detection system was established to acquire the optimum fluorescence data and discriminate between elements depending on their characteristic fluorescence. This set-up, coupled with an appropriate image reconstruction technique leads to a detailed two-dimensional image. Compared to the conventional image reconstruction techniques, the developed reconstruction method is a statistical technique and has an appropriate convergence toward an image with acceptable resolution. Moreover, it is a simplified technique that allows the imaging of many different applications.

Keywords: X-ray fluorescence, X-ray detection, Simulation code, Image reconstruction algorithm.

Contents:

Chapter 1	Introduction	16
Chapter 2	: X-Ray Physics, Production & Detection.....	22
2.1	Introduction.....	22
2.2	X-Ray physics	22
2.2.1	X-Ray production	23
2.3	Interactions of X-ray with matter	25
2.3.1	Coherent (Rayleigh) scattering.....	26
2.3.2	Photoelectric effect.....	27
2.3.3	Compton scattering.....	27
2.3.4	Pair production	28
2.4	X-Ray Fluorescence	28
2.4.1	X-ray fluorescence features	30
2.4.2	X-ray source and fluorescence energies.....	30
2.5	X-ray detection	32
2.5.1	Gas-filled detector.....	32
2.5.2	Scintillator detector	34
2.5.3	Semiconductor detectors	36
2.6	Detector characteristics.....	37
2.6.1	Detector's resolution and efficiency	37
2.6.2	Detector's response time	40
2.6.3	Detector's operation modes.....	41
2.7	Conclusion.....	43
Chapter 3	Transmission & Fluorescence X-Ray tomography	45
3.1	Introduction.....	45
3.2	Tomography basic principle	46
3.2.1	Transmission tomography	46
3.2.2	Emission tomography	47
3.3	Image reconstruction techniques	48
3.3.1	Reconstruction methods	48
3.3.2	Principle of projection acquisition and Radon Transform	49
3.4	Transmission tomography.....	51

3.4.1 Direct Fourier reconstruction	51
3.4.2 Filtered Back-projection (FBP).....	52
3.5 Emission tomography.....	55
3.5.1 Algebraic Reconstruction Technique	57
3.5.2 Gradient and Conjugate Gradient Algorithm.....	59
3.5.3 Maximum Likelihood Expectation Maximization (MLEM) Algorithm.....	61
3.5.4 Ordered-Subsets Expectation Maximization (OSEM) Algorithm	62
3.5.5 Maximum A Posteriori (MAP) Algorithm	63
3.6 Conclusion.....	64
Chapter 4 Simulation & validation method.....	65
4.1 Introduction.....	65
4.2 Set-up modeling.....	66
4.3 Source definition: Polychromatic source loading.....	68
4.4 Object description: Stereo-Lithography (StL) format.....	69
4.5 Collimator and detector modeling.....	72
4.6 Simulation process.....	74
4.7 Attenuation correction.....	74
4.8 Simulated fluorescence quantitative analysis.....	76
4.8.1 Solid angle.....	78
4.9 Simulated Compton scattering.....	78
4.10 Parameters optimization.....	80
4.11 Image reconstruction of Transmission tomography & Emission tomography	81
4.12 Reconstruction model.....	82
4.13 Attenuation map estimation of transmission tomography	82
4.13.1 Filtered back-projection description, implementation & sinogram creation.....	82
4.14 Fluorescence map estimation of emission tomography.....	84
4.14.1 Probability matrix estimation	85
4.14.2 MLEM implementation.....	90
4.15 Regularization.....	92
4.15.1 Optimization of data acquisition	93
4.15.2 MLEM result with prior.....	94
4.16 Methodology of experimental validation	94

4.16.1 Description of the measurement system used for fluorescence validation	94
4.16.2 Objects used for experimental validation	96
4.17 Conclusion	97
Chapter 5 Results & Discussion	99
5.1 Introduction.....	99
5.2 Simulation results	99
5.2.1 Sinogram validation results	99
5.2.2 Simulated transmission tomography results	100
5.2.3 Simulated fluorescence results.....	102
5.2.4 Filtered Back Projection (FBP) validation.....	105
5.2.5 Maximum Likelihood Expectation Maximization (MLEM) validation.....	106
5.2.6 Parameter impact study	109
5.2.7 Experimental validation of simulation	115
5.3 Experimental Computed Tomography (CT) results	118
5.3.1 CT obtained image	119
5.3.2 Filtered image.....	119
5.3.3 Spatial resolution	120
5.4 Experimental Fluorescence tomography results	122
5.4.1 Spatial resolution	124
5.4.2 Influence of iterations' number	125
5.4.3 Emission Tomography spatial resolution.....	125
5.5 Conclusion	130
Chapter 6 : Conclusion & perspectives	131
Annex A 133	
Annex B 133	
Annex C 134	
Annex D 135	
Annex E 136	
References 139	

List of figures:

Figure 1.1: Schematic of experimental setup used to obtain fluorescence data [2][3].....	17
Figure 1.2: Experimental set-up of X-ray fluorescence element micro-tomography [4].	18
Figure 1.3: Three different imaging modes of X-ray fluorescence tomography [6].	19
Figure 1.4: Work methodology.	20
Figure 2.1: Electromagnetic spectrum [8].	23
Figure 2.2: (a) Old X-ray tube used during 1896 (taken from physik.uibk.ac.at); (b) Modern X-ray tube used beginning of 2000(taken from imactscan.com).	23
Figure 2.3: X-ray tube with rotating anode [10].....	24
Figure 2.4: Bremsstrahlung radiation, relative intensity versus wavelength (taken from: Medical X-rays-Hyperphysics).	24
Figure 2.5: Probabilities of the three main types of interactions [11].....	26
Figure 2.6: Coherent Rayleigh scattering [12].	26
Figure 2.7: Photoelectric effect; Fluorescence effect [12].	27
Figure 2.8: Compton Scattering [12].	27
Figure 2.9: Pair Production [12].	28
Figure 2.10: Fluorescence steps: X-ray absorption and fluorescent photon emission from different shells.	29
Figure 2.11: Jablonski energy diagram: S0 is the ground state; S1 , S2 are the 1 st & 2 nd electronically excited states [13].	29
Figure 2.12: (a) Bohr's atomic shell model, (b) Diagram of energy levels showing the atomic transitions.	31
Figure 2.13: Gas-filled detector consisting of an insulating chamber, an anode and a cathode [16].	33
Figure 2.14: Different voltage regions corresponding to different gas-filled detector [17]	34
Figure 2.15: Scintillation detector [18].	34
Figure 2.16: Diagram showing the ray detection steps.	37
Figure 2.17: Detector resolution; the width is usually measured at half the maximal height of the peak [17].	38
Figure 2.18: Detection efficiency computation [19].	39
Figure 2.19: Inverse Square Law illustration [17].	40
Figure 2.20: Recorded events on a detector for a paralyzable and a non-paralyzable system [17].	41

Figure 2.21: The current mode configuration [17].	42
Figure 2.22: Detector pulse mode [20].	43
Figure 2.23: Counting spectrum defined by <i>E_{min}</i> & <i>E_{max}</i> .	43
Figure 3.1: Data acquired from different views used to reconstruct a cross-sectional image.	45
Figure 3.2: (a) Parallel-Beam Geometry, (b) Fan-Beam Geometry, (c) & (d) Same geometries in different angles [21].	46
Figure 3.3: Physical principle of 1-D tomography [22].	46
Figure 3.4: Transmission tomography	47
Figure 3.5: Emission tomography.	48
Figure 3.6: Reconstruction algorithm classification.	49
Figure 3.7: Parallel beam geometry with coordinate system [21].	49
Figure 3.8: A sinogram <i>gr, θ</i> representing values of each angular position on each detector pixel [21].	50
Figure 3.9: Relation between image space, Radon space and Fourier space according to Fourier slice theorem [27].	51
Figure 3.10: The Back-projection process [28].	53
Figure 3.11: Filtered- back projection [11].	55
Figure 3.12: Fourier transform algorithm.	55
Figure 3.13: A discrete model of the projection process in (a) 'Transmission Tomography' [30]; (b) 'Emission Tomography' [31].	56
Figure 3.14: Flow chart of an iterative image reconstruction scheme [31].	57
Figure 3.15: The Kaczmarz procedure with 2 measurements [32].	58
Figure 3.16: Gradient Algorithm: Difference between estimated and measured projections [26].	60
Figure 3.17: MLEM in the form of the general iterative model [32].	62
Figure 3.18: OSEM representing 8 projections divided into 2 subsets each one consists of 4 projections [33].	63
Figure 4.1: (a) Monte Carlo technique [38]; (b) Ray Tracing technique.	66
Figure 4.2: (a) CT transmission modeling chart; (b) ET fluorescence modeling chart.	67
Figure 4.3: Data entry file.	68
Figure 4.4: A polychromatic X-ray source spectrum representing the number of photons at different working tensions (data file brought from LIST laboratory; CEA-Saclay).	69

Figure 4.5: (a) Adjacent voxels of 12 facets each. (b) Cube of (x=3; y=3; z=5) dimension.	70
Figure 4.6: The facet orientation defined by the right-hand-rule or the counter clock wise orientation.....	70
Figure 4.7: An StL cube with resolution 1; 0.3; 0.1 consecutively.....	70
Figure 4.8: (a) Fluorescence emission illustration; (b) Simulation of source-object-collimator-detector.....	71
Figure 4.9: (a) Sample preparation and implementation; (b) Voxel filename; (c) Material filename.....	72
Figure 4.10: Detector-collimator modeling.....	73
Figure 4.11: (a) Detector and a 1-hole collimator with long septa; (b) Detector and a multi-hole collimator with short septa.	74
Figure 4.12: Energies and their corresponding attenuation coefficients (for Lead <i>Pb</i> element).	75
Figure 4.13: Interaction between source, voxel and detector showing the angles.....	76
Figure 4.14: Solid angle of an incident photon in the direction of a particular pixel [40].	78
Figure 4.15: Compton scattering process	79
Figure 4.16: Compton scattering acquisition.....	80
Figure 4.17: Reconstruction algorithms methodology.....	81
Figure 4.18: Sinogram formation.	84
Figure 4.19: The matrix weights formed by the projections on detector bins.....	86
Figure 4.20: The matrix product (done according to figure 4.19).	87
Figure 4.21: The geometry of photons emission from pixel i reaching detector bin j [44].	88
Figure 4.22: Representation of the common area of a pixel i and the detection zone of a detector j [44].	88
Figure 4.23: Probability matrix values displayed.....	90
Figure 4.24: MLEM implementation procedure.	92
Figure 4.25: Optimization parameters.....	93
Figure 4.26: Implementation of image obtained from FBP in the image reconstruction process.....	94
Figure 4.27: (a) Geometrical arrangement; (b) Experimental detection system.	95
Figure 4.28: X-ray source.	95

Figure 4.29: Scintillator detector.	96
Figure 4.30: (a) Aluminum sample “Al”; (b) Lead sample “Pb”; (c) Lead immersed in Aluminum; (d) Different types of amber.....	97
Figure 5.1: (a, b) 120 projections;(c, d) 10 projections; (a, d) 20 cm detector;(b, d) 40 cm detector.	100
Figure 5.2: Sinogram reflecting 1 object (a); 2 objects (b); 3 objects (c); 4 objects (d)..	100
Figure 5.3: StL image of (a) a sphere; (b) a cube.....	101
Figure 5.4: Simulated image of (a) a sphere; (b) a cube.....	101
Figure 5.5: Corresponding sinograms of (a) a sphere (b) a cube.	101
Figure 5.6: Fluorescence emission with 1 hole collimator.....	102
Figure 5.7: Lead & Germanium fluorescence with respect to X-ray source voltage.	103
Figure 5.8: Emitted fluorescence of different elements at specific energies.....	104
Figure 5.9: Fluorescence counts of lead (Pb) immersed in different medium.	105
Figure 5.10: Reconstructed image of test samples obtained from FBP method.....	106
Figure 5.11: Validation of probability matrix and MLEM algorithm.....	107
Figure 5.12: Reconstructed images reflecting the spatial localization of fluorescence object.....	108
Figure 5.13: Reconstructed images based on same settings for a variety of elements...	109
Figure 5.14: Results according to number of projections.....	110
Figure 5.15: Results according to number of iterations.....	110
Figure 5.16: (a) White wide box inside a black box; (b) White narrow box inside a black box; (c) Close objects.....	111
Figure 5.17: (a) Sinogram of a white wide box; (b) Sinogram of a white narrow box; (c) Sinogram of close objects.	111
Figure 5.18: Reconstructed images through MLEM algorithm.....	112
Figure 5.19: Reconstructed images of sample containing Lead elements with high resolution.....	112
Figure 5.20: Blurred image.....	113
Figure 5.21: MLEM result before and after implementing an image from FBP.	113
Figure 5.22: Reconstructed image of fluorescent samples obtained from FBP method.	114
Figure 5.23: Aluminum fluorescence.....	115
Figure 5.24: Lead fluorescence.	116
Figure 5.25: Lead immersed in Aluminum.....	116

Figure 5.26: Red Amber fluorescence.	117
Figure 5.27: Black Amber fluorescence.	117
Figure 5.28: Comparison between simulated and experimental fluorescence.	118
Figure 5.29: (a) Original sample; (b) Computed Tomography image result.	119
Figure 5.30: (a) Non-filtered image; (b) Filtered Computed Tomography image result; (c) Smoothed image.	120
Figure 5.31: A superimposed grid over the original sample (a) and the CT image (b)...121	
Figure 5.32: Distances between elements in the original sample (a) and the CT image (b).	121
Figure 5.33 : Sinograms comparison between (a) reconstructed and (b) experimental.	122
Figure 5.34: Energy peaks.....	123
Figure 5.35: Emission tomography image result.	123
Figure 5.36: The registered values along the distance.	124
Figure 5.37: MLEM results showing increasing number of iterations.....	125
Figure 5.38: Iron material with diameters ranging from 1 to 5 mm.	126
Figure 5.39: Images of 5 mm diameter of Iron material; (a) original sample;(b)CT image; (c) ET image.....	126
Figure 5.40:Images of 4 mm diameter of Iron material; (a) original sample;(b)CT image; (c) ET image.....	126
Figure 5.41:Images of 3 mm diameter of Iron material; (a) original sample;(b)CT image; (c) ET image.....	127
Figure 5.42:Images of 2 mm diameter of Iron material; (a) original sample;(b)CT image; (c) ET image.....	127
Figure 5.43:Images of 1 mm diameter of Iron material; (a) original sample;(b)CT image; (c) ET image.....	127
Figure 5.44: Fluorescence emission of 5 mm diameter element.	128
Figure 5.45: Fluorescence emission of 4 mm diameter element.	128
Figure 5.46: Fluorescence emission of 3 mm diameter element.	128
Figure 5.47: Fluorescence emission of 2 mm diameter element.	129
Figure 5.48: Fluorescence emission of 1 mm diameter element.	129
Figure 5.49: Fluorescence peaks at different diameters elements.	130
Figure B.1: Simulation code chart.	134
Figure C.1: The mathematical procedure of intersection line-facet.	135

Figure C.2: For each scanning line the distance is computed between 2 intersection points.....136

List of tables:

Table 2.1: X-ray fluorescence spectrum showing the presence of different elements (Image Courtesy of ESRF).	30
Table 2.2: Different Gas-filled detector types.....	33
Table 2.3: Properties of organic and inorganic scintillator.....	36
Table 5.1: Fluorescence energies based on Moseley's law.....	103

List of abbreviations:

Al	Aluminum
ART	Algebraic Reconstruction Technique
ASCII	American Standard Code for Information Interchange
CAD	Computer-Aided Design
CEA	Atomic Energy Commission
CT	Computed Tomography
ET	Emission Tomography
EM	Expectation Maximization
FBP	Filtered- Back Projection
FFT	Fast Fourier Transform
FOV	Field Of View
FT	Fluorescence Tomography
FWHM	Full Width at Half Maximum
Ge	Germanium
IEEE	Institute of Electrical and Electronics Engineers
IFFT	Inverse Fast Fourier Transform
IFT	Inverse Fourier Transform
INSERM	Institut National de la Sante et de la Recherche Médicale
IMEP2	Ingénierie-Matériaux Mécanique Energétique Environnement Procédés Production
LIU	Lebanese International University
MAP	Maximum A Posteriori
MAPEM	Maximum A Posteriori Expectation Maximization
ML	Maximum Likelihood
MLEM	Maximum Likelihood Expectation Maximization
Pb	Lead
PET	Positron Emission Tomography
P-I-N	Positive-Intrinsic-Negative
PMMA	Poly-Methyl-Methacrylate

PMT	Photomultiplier Tube
RC	Resistor-Capacitor
CsI	Caesium Iodide
E-step	Expectation Step
GM	Geiger-Muller
IJIP	International Journal of Image Processing
kV	Kilovolt
MeV	Mega-Electron-Volt
MIRG	Medical Imaging Research Group
M-step	Maximization Step
NaI	Sodium Iodide
OSEM	Order Subset Expectation Maximization
OSL	One Step Late
QDE	Quantum Detection Efficiency
RGB	Red-Green-Blue
SART	Simultaneous Algebraic Reconstruction Technique
SIRT	Simultaneous Iterative Reconstruction Technique
SPECT	Single Photon Emission Computerized Tomography
SPIE	Society of Photo-Optical Instrumentation Engineers
StL	Stereo-Lithography
Ti	Titanium
Tl	Thallium
UHF	Ultra-High Frequency
VHF	Very High Frequency
XAFS	X-Ray Absorption Fine Structure
XFEMT	X-ray Fluorescence Element Micro-tomography
XFET	X-ray Fluorescence Emission Tomography
XRF	X-Ray Fluorescence
XRFT	X-Ray Fluorescence Tomography
γ -Ray	Gamma Ray

Chapter 1 Introduction

Various applications in medical, food, nuclear and petrol industry require thorough investigation of production samples through non-destructive testing procedures. Diverse applications include chemical and environmental analysis. In some applications investigation includes localization and identification of certain metallic particles included in a fluid flow for instance analyzing metals in wastewater, such as silver emulsion from a photo lab. This is usually done through cross-sectional images of slices of the flow.

In some particular applications, liquid samples are flowing in pipes with opaque walls, thus preventing their inspection using optical imaging techniques. In order to overcome this lack of visibility, penetrating radiation-based imaging techniques are used. One of these techniques is the X-ray computed transmission tomography where an X-ray source is used to irradiate the sample from different directions. Radiation detectors are then used to acquire data in all angles around the object. The collected data contain information related to the amount of absorption of radiation in the object. Indeed metallic particles will absorb more radiation as compared to the surrounding liquid due to their high densities. Spatial distribution of metallic particles could be obtained then by applying image reconstruction techniques. However, transmission tomography techniques are unable to identify and discriminate between different types of metals, especially for those who have similar densities due to the minor difference in their attenuation coefficients. Consequently, an accurate qualitative and quantitative analysis is required for the identification of distinct elements especially for samples including a large number of elements. The objective of this thesis project is to detect and quantify the elemental composition of a sample based on the fluorescence data emission. A distribution map with acceptable precision can be obtained.

In order to overcome the lack of information obtained through transmission tomography, few studies investigated the use of emission tomography to deal with this problem.

In 1989, Cesareo and Mascarenhas [1] attempted to localize spatially distributed elements by acquiring fluorescence data from a sample irradiated by an X-ray tube. The fluorescence photons were detected at 90° from the incident X-ray and the absorption effect was corrected. In order to obtain a sample distribution, the sample was moved in the x - y plane. The obtained results were useful for mapping medium of high atomic number elements; however the used technique did not permit to identify the types of

elements included in the sample and no information about the “reconstruction technique” used was communicated. In addition, in order to analyze a sample volume smaller than 1 mm^3 , a very intense and highly collimated radiation such as a synchrotron radiation is necessary.

In 1991, Hogan et al. [2] proposed adapting one of the algorithms used in transmission tomography, which is the classical back-projection, in order to reconstruct fluorescence data. Two detectors placed at 0° (for transmission) and at 90° (for fluorescence emission) of the incident beam were used in the experiment. They applied corrections to absorption before and after the fluorescing element. For each pixel of the reconstructed image, the correction factor was evaluated essentially as the mean correction factor averaged over all angular views. The solution proposed provided a compromise between image quality and reconstruction speed.

In 2001, Brunetti & Golosio [3] performed a complete implementation of Hogan’s algorithm, together with some new simulations with and without the correction of self-absorption. In order to be more realistic, Brunetti & Golosio developed Hogan’s technique [2] in 1991 as follows:

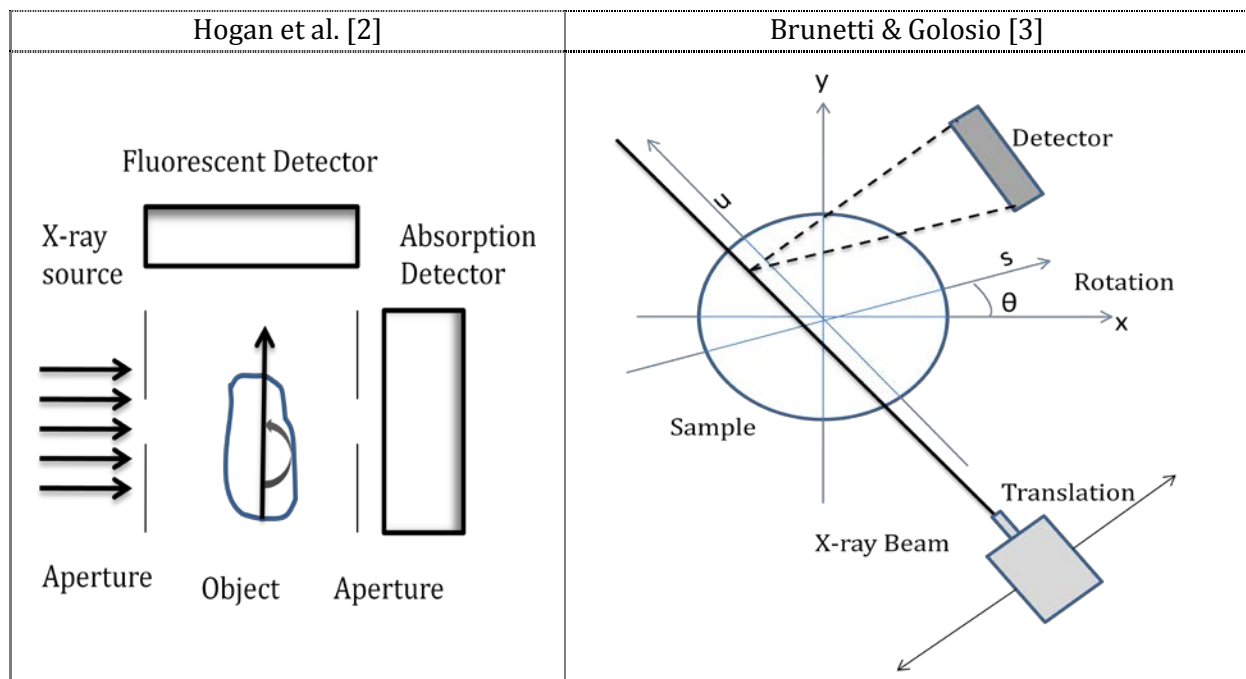


Figure 1.1: Schematic of experimental setup used to obtain fluorescence data [2][3].

- As a geometrical arrangement (see figure 1.1), a detector of infinite length was presupposed with its surface perpendicular to the X-ray pencil beam. The X-ray source and the detector were held fixed, while the sample was rotated and translated.
- As for image reconstruction, the input data set is represented by the count rates measured for a complete set of rotational and translational steps using a monochromatic X-ray source. In addition, the noise problem coming from the total counts of all beam directions was considered as artifact in Hogan’s work.

This problem was solved by applying a convolution to the projections with a filter suitable for the back-projection in order to remove such noise.

In Brunetti & Golosio's work [3], the fluorescence probability was well established but there was no identification of the elements. At the same period, the field of micro-analysis has been improved. Thus, most of the established techniques are micro-tomography fluorescence for which a synchrotron is required.

In 2003, Schroer et al. [4] used X-ray fluorescence element microtomography (XFEMT) to determine the distribution of elements on a virtual section across the sample with a resolution in the micrometer range (see figure 1.2). They demonstrated the possibility to map physiologically relevant ions, trace elements, and heavy metal pollutants at the cellular level. Attenuation effects inside the plant were corrected by a self-consistent tomographic reconstruction technique. A major advantage of the method is the reduced amount of sample preparation required to obtain the element distribution. However, the acquisition time to obtain a tomogram needs to be reduced significantly.

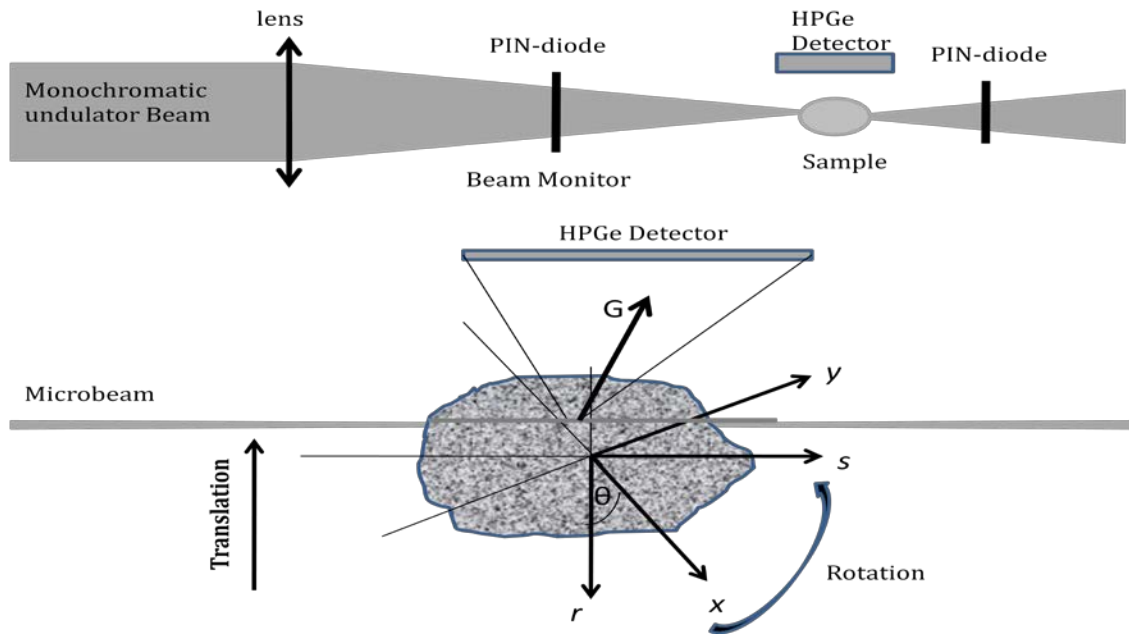


Figure 1.2: Experimental set-up of X-ray fluorescence element micro-tomography [4].

Consequently, an iterative image reconstruction technique was required. Many reconstruction algorithms for tomography have been developed and applied on X-ray fluorescence tomography. In 2011, Miqueles et al. [5] proposed a source code for the following reconstruction techniques: Filtered back-projection, Novikov's inversion and Hogan's formula. The input data set was represented by a complete sinogram covering a determined angular range. Users were allowed to set solid angle range for fluorescence emission on any adopted algorithm. Depending on the data size, the running time of Miqueles program was as an average 1 second to 15 minutes.

Recently in December 2011, Meng et al. [6] performed many feasibility studies on X-ray fluorescence emission tomography (XFET) using synchrotron X-ray and Monte Carlo simulation. As shown in figure 1.3, the object was illuminated with synchrotron X-

ray beams of various cross-sectional dimensions (the object was either irradiated by a parallel-beam or a pencil-beam of synchrotron X-rays). The three different imaging geometries were compared using Monte Carlo simulations and an analytical system performance index. In the first approach (figure 1.3 (a)) a line-by-line scanning was applied on a rotating sample. Fluorescence photons were collected by non-position-sensitive X-ray spectrometer. A correction for the attenuation of both incident and fluorescent photons was considered. Using modified filtered back-projection (FBP) and “penalized” Maximum-Likelihood (ML) algorithms a 3-D distribution of trace elements was reconstructed. One of the major limitations of this approach was the long imaging time required for 3-D imaging studies. They proposed two other approaches (see figure 1.3 (b) & (c)). In the second one, a thin sheet-beam of synchrotron photons was used. This produced a stronger signal that increased the fluorescence photons emission. While the detection system consisted of several X-rays imaging-spectrometers, each coupled to a multiple pinhole apertures. In this geometrical approach the 2-D spectral detectors had lower detection efficiency, and consequently the resolution capability was limited. A compensation for low resolution could be done by using small pinholes in the detectors but this would required also longer imaging time. In the third approach (figure 1.3(c)), a pencil-beam of the synchrotron source was used and the detection system consisted of position sensitive detectors coupled to multiple-slit-apertures in order to provide greater geometrical efficiency. It is a simplified scanning process where the object was static and scanned line by line but the sample rotation was needed to improve the image quality. This mode has a potential of providing a greatly improved imaging speed. In the last two approaches, more imaging information was provided by the detected fluorescence photons and in an appropriate speed, but at the cost of reduced detection efficiency and huge radiation dose-rate to the object.

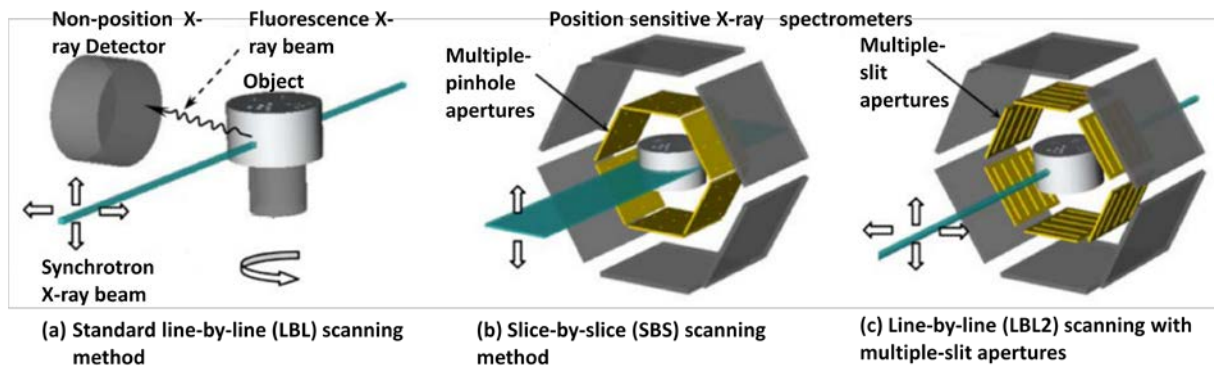


Figure 1.3: Three different imaging modes of X-ray fluorescence tomography [6].

To overcome the hurdle of using synchrotron X-ray source and to perform an imaging technique far from slow data collection or complicated simulations, a new approach is proposed within this thesis project. This approach allows localizing elements inside complex and heterogeneous samples. The sample, being excited by a polychromatic X-ray beam, is analyzed depending on the emitted fluorescence acquired by the detection system. Thus, in addition to localization, this system is able to provide a quantitative analysis and qualitative elements identification.

Usually, the inverse problem of finding a cross-sectional image from fluorescence data requires a computational effort. This is due mainly to three main limitations. First, the fluorescence emission is probabilistic which makes its detection a hard task. Second, the obtained fluorescence counts are of low energy, which complicates the detection efficiency. Third, the sample that requires analysis is often a mixture of many components in a complex matrix; hence the self-absorption effect inside the sample must be taken into account. Based on these data, the scope of this thesis is to adapt this technique and develop an image reconstruction method to provide a good material characterization.

The research methodology consists of three main parts as shown in figure 1.4.

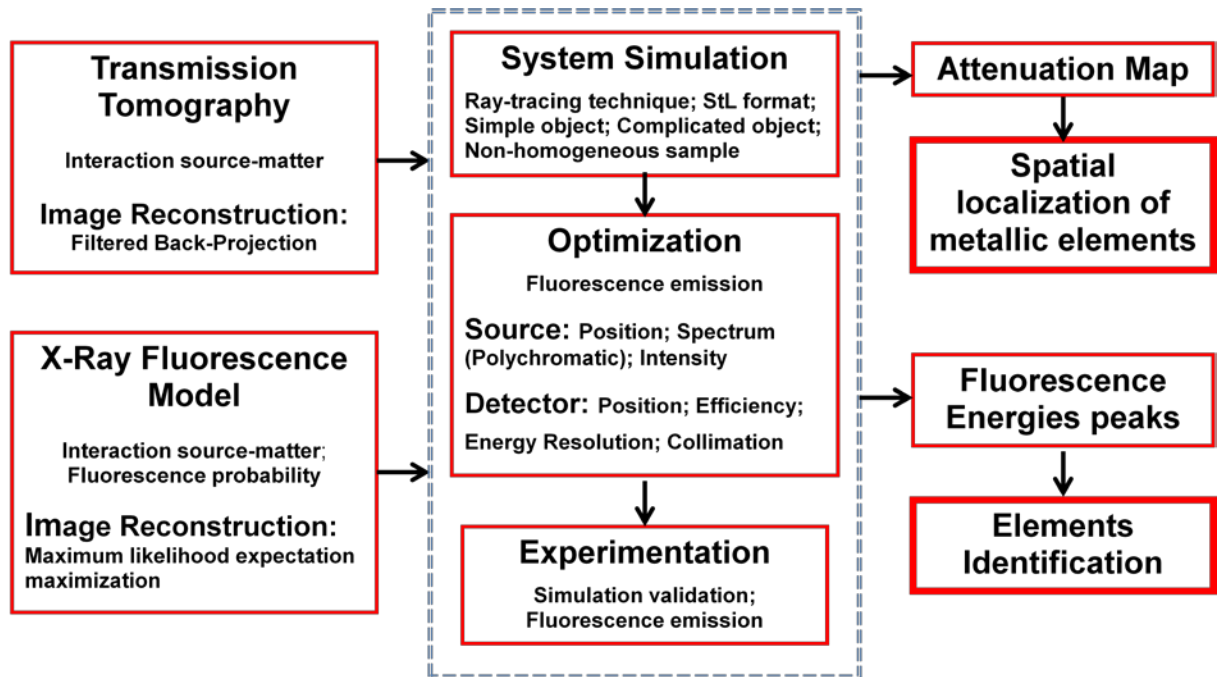


Figure 1.4: Work methodology.

More specifically, the transmission tomography is established in order to obtain an attenuation map; whereas, the fluorescence emission tomography will lead to the identification of the elements along with their spatial distribution in the sample. The first part is a simulation of the tomography technique itself in which the imaging components and the transmission phenomena with the fluorescence emission are simulated. Then, from the established simulation code having a specific technique and format, an optimization of the parameters takes place. At the same time, an experimentation phase is done to validate the simulation code. Once the simulated or experimental validations are acquired; an image reconstruction technique is developed according to the optimized parameters. When all parameters, including the image reconstruction algorithm, are developed and identified; many tests are performed with a dedicated experimental set-up. Consequently, the obtained results reveal a detailed cross-sectional image of the sample.

Starting by a background for the system, chapter 2 is devoted to present a physical basis of X-ray production and detection; whereas transmission and fluorescence X-ray tomography are presented in chapter 3. Chapter 4 is dedicated to the simulation code of the fluorescence properties and the tomographic technique in addition to the implementations of transmission and emission tomography. The experimental validation is covered in chapter 5 which comprises also a detailed experiment acquisition set-up. The results of localization, emission and identification are addressed. The last chapter presents the conclusion derived from this research work in addition to the perspectives for future work in this domain.

Chapter 2 : X-Ray Physics, Production & Detection

2.1 Introduction

In this chapter a background about the main components of X-ray tomography system are addressed. The X-ray tube used for X-ray production as well as the interaction of X-rays with matter and the concept of fluorescence are presented in details. An explanation of the detection process constitutes one of the key materials discussed in this chapter.

2.2 X-Ray physics

The X-rays, discovered by the German physicist Wilhelm Conrad Von Roentgen in 1895, are an electromagnetic radiation of high penetrating power. They are high-energy photons whose wavelength ranges from 0.01 to 10 nm and they have medical and industrial applications. Figure 2.1 represents the whole electromagnetic spectrum from the longer wavelength to the shorter. For each spectral region, the wavelength, the frequencies and the energy of one photon in addition to the common usage are displayed. For instance, “Radio waves (VHF & UHF)” are used for “Nuclear Magnetic Resonance & Electron Paramagnetic Resonance”; “Microwaves” are used for “Rotational Transitions”; “Infrared” for “Vibrational Transitions”; “Visible Light and Ultraviolet” for electronics transitions, “X-rays” for “Ionization” and “ γ -rays” for “Nuclear effects” [7].

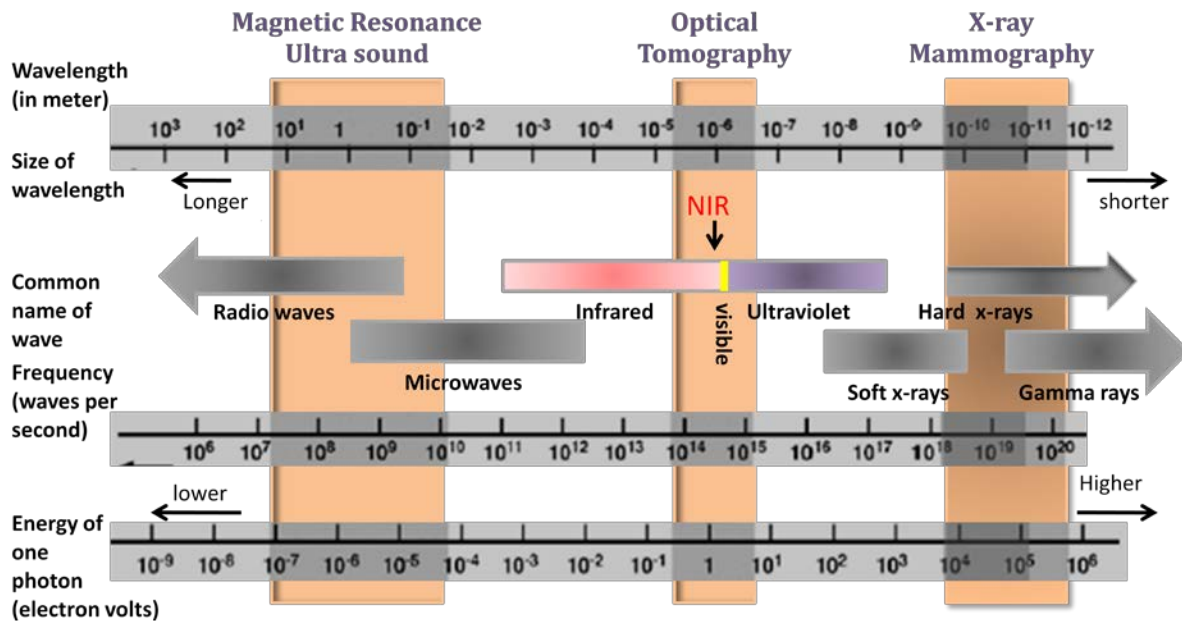


Figure 2.1: Electromagnetic spectrum [8].

2.2.1 X-Ray production

X-rays are produced in an apparatus called the X-ray tube. As shown in Figure 2.2, it is a vacuum tube containing a cathode and a target anode. Most of the X-ray tubes envelopes are made of glass instead of metals.

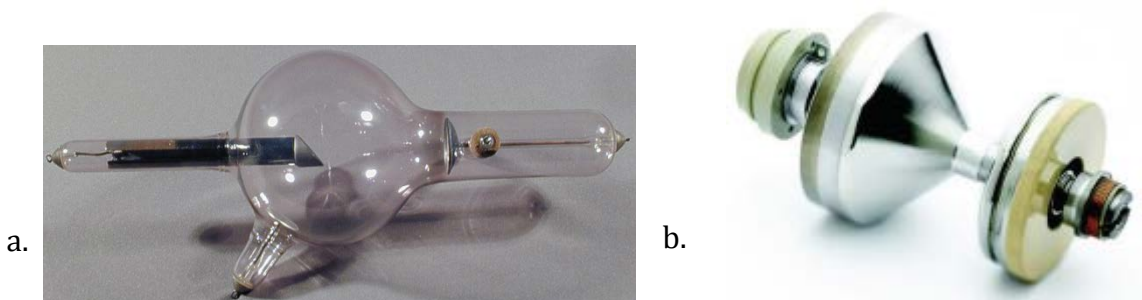


Figure 2.2: (a) Old X-ray tube used during 1896 (taken from physik.uibk.ac.at); (b) Modern X-ray tube used beginning of 2000 (taken from imactscan.com).

The X-ray production, represented in figure 2.3, involves accelerating a beam of electrons to strike the surface of a metal target. A filament mounted in the groove of the cathode is heated by a relatively low voltage supply. Electrons are emitted from the filament when their acquired thermal energy overcomes their binding energy. These electrons are then accelerated toward the anode by applying a high potential difference across the tube from the high voltage power supply[9].

The target is usually made of a heavy metal like the tungsten or copper. Incident electrons hitting the target approach the nucleus but do not penetrate due to the strength of the target nuclear force. Hence at any tension applied, a deflection of the electron occurs. This deflection or slow down causes a loss of energy that is released as a "Bremsstrahlung" or braking X-rays. These X-ray photons have a new direction and a continuous distribution of energies. As much as the electron is close to the nucleus, higher energy and less number of photons are produced. The other case of interaction is

when the incident electron energy is higher than the binding energy of the anode target atom. Hence, an orbital electron is ejected leaving a hole. An outer-shell electron fills the vacancy. If the energy gap between the levels is great enough, then characteristic X-ray photon is released.

As shown in figure 2.4, the two sharp peaks represent the characteristic X-ray lines and are superimposed on the continuous Bremsstrahlung X-ray spectrum. k_α is a characteristic X-ray produced when the electron transition is from L-level to K-level while K_β is from M-level to K-level. The Bremsstrahlung radiation shows a range of energy values corresponding to the loss of incident kinetic energy when interacting with target nucleus.

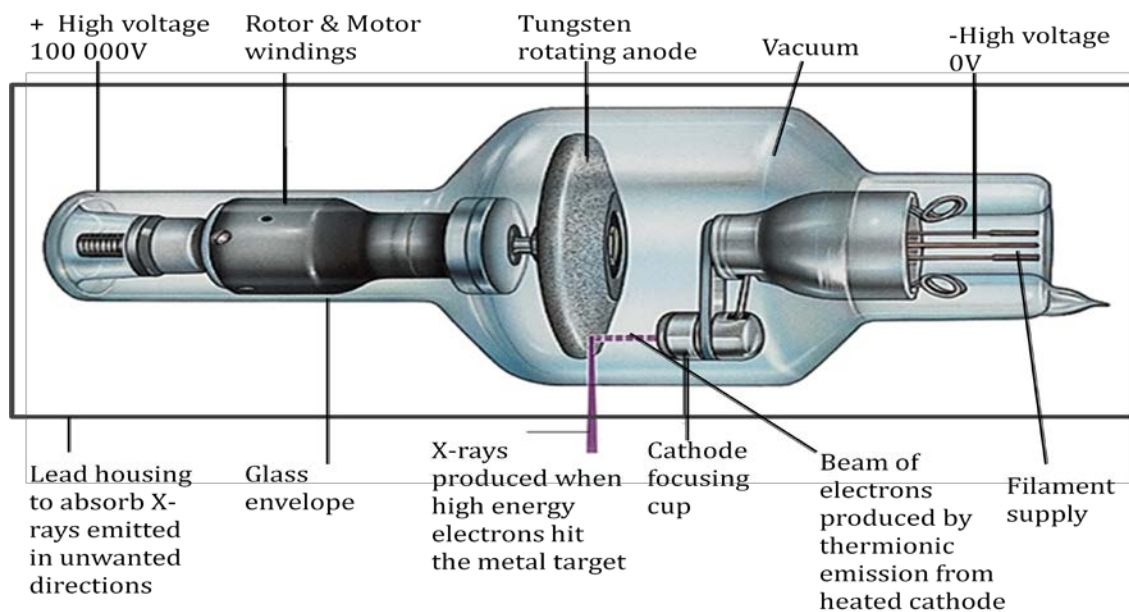


Figure 2.3: X-ray tube with rotating anode [10].

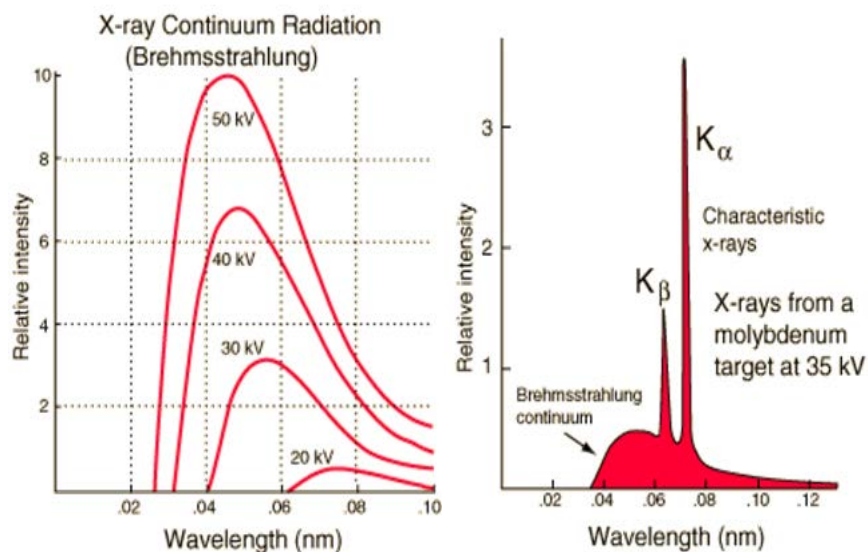


Figure 2.4: Bremsstrahlung radiation, relative intensity versus wavelength (taken from: Medical X-rays-Hyperphysics).

The efficiency of the produced X-rays depends on their energy, which determines its penetrating power. As the kinetic energy of the incident electron increases, the intensity and the energy increase. In general, 99% of the kinetic energy is converted into thermal energy. Therefore, the target material must have a high melting point and a great heat-dissipating capacity. Most of them have large focal spot area and in some cases a rotating anode in order to have a greater effective area exposed to the beam.

The energy of the characteristic X-ray photons is specific and corresponds to the difference of energies between transition shells. The energy of Bremsstrahlung X-rays photons ranges from zero to an energy equivalent to the incident kinetic energy of the projectile electron. The photon energy, a specification of the tube voltage, is derived from the electron wave combination:

$$E = h f_r = \frac{h c}{\lambda} \quad (2.1)$$

where λ is the wavelength; the output radiation contains a spread of wavelength;

c is the speed of light that is equal $3 \times 10^8 \text{ m/s}$;

f_r is the frequency of the radiation;

h is the Planck's constant that is equal to $4.1356 \times 10^{-15} \text{ electron-volt} \cdot \text{seconds}$.

The high penetrating power of the X-rays or the high energy varies with the tube settings. The beam quality is directly related to the energy. Also, it depends on the acceleration voltage, the beam current and the tube target material. These factors affect the intensity of the beam. For instance, by increasing the tube voltage, the X-ray beam will be more energetic and thus more penetrating photons are produced. This control is usually expressed in "keV". Another control of the output of the X-ray tube is the milliamperage "mA" control. Higher current will result in a greater flux of photons. Consequently, no photons at energies higher than the applied high voltage could be found in the X-ray spectrum. The low energies found in the spectrum with longer wavelength are called the soft X-rays and are usually unwanted as they are totally absorbed in the sample. Harder X-ray beam could be obtained by applying a filter (usually a thin metallic film) that absorbs low energy photons while photons at higher energies will be able to continue their way out of the filter [9].

2.3 Interactions of X-ray with matter

The interaction of X-ray with matter induces resonance in the atom electrons. This is due to an electromagnetic force that interferes as an oscillating magnetic and electric fields. Among the different types of interactions, we distinguish four principal

attenuation mechanisms that are classical or coherent (Rayleigh) scattering, Compton (scattering) effect, photoelectric effect, pair production.

The interaction of X-ray with matter is governed by quantum theory. Relative probabilities of the three absorption mechanisms, discussed in previous section, versus energy expressed in mega-electron-volt (MeV) are shown in figure 2.5.

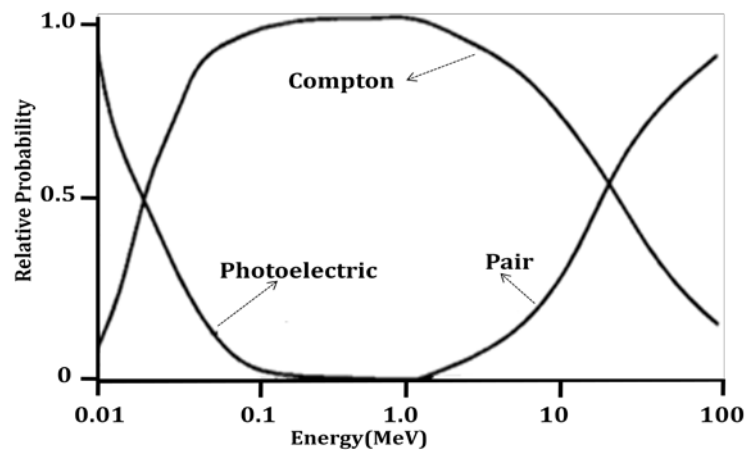


Figure 2.5: Probabilities of the three main types of interactions [11].

Low energy photons are absorbed primarily by photoelectric mechanism, high energy photons by pair production, and mid-level energy photons by Compton scattering. The energies represent the size of pulses at the detector [11].

2.3.1 Coherent (Rayleigh) scattering

Also called, Thomson scattering, it occurs when a photon approaches the specimen with insufficient energy to ionize the atom. Its energy is usually about 10 to 70 keV. The incident photon is deflected into a new direction without any loss of energy. It keeps its same wavelength and penetrating power. The coherent scattering (figure 2.6) is of little importance in medical imaging and has a minor contribution to the absorption coefficient.

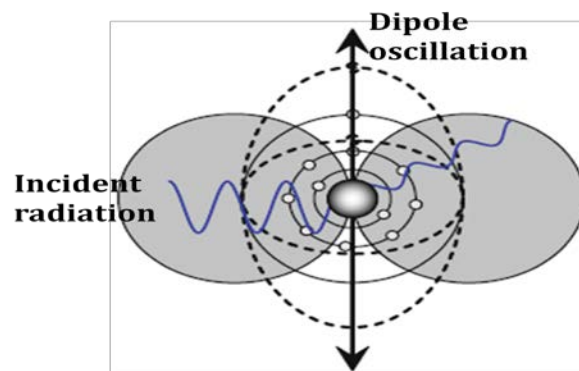


Figure 2.6: Coherent Rayleigh scattering [12].

2.3.2 Photoelectric effect

As the incident photons are completely absorbed, the photoelectric effect is known as “true absorption”. It is the dominant process for X-rays absorption up to energies of about 500 keV (figure 2.7). When the incident energy is equal or greater to the atom binding energy then the photon will “kick-out” one of the shell electrons. As a consequence, the ionized atom needs to return to the neutral space. An electron from a higher energy level will move to the unfilled energy level. This can happen as a cascade from the L-shell to the K-shell and from the M-shell to the L-shell. This moving electron has an excess energy to get rid of it. Hence, during the transition a photon is produced. The emission of this photon is called the fluorescence or the characteristic radiation. This process is frequent for atoms with high atomic number.

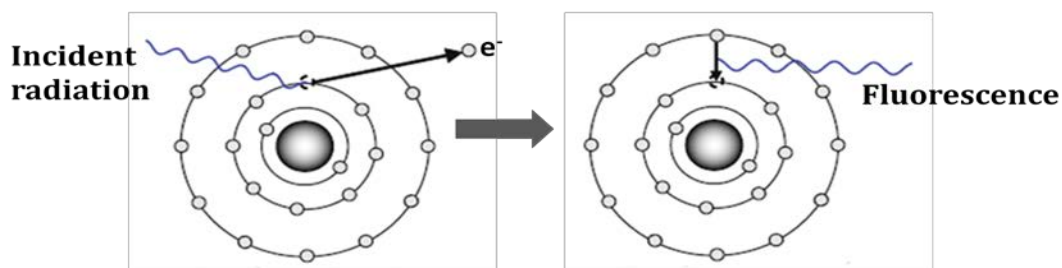


Figure 2.7: Photoelectric effect; Fluorescence effect [12].

2.3.3 Compton scattering

When the incident X-ray photons are of moderate energy, ionization of the target atom occurs. A part of the incident energy is transferred to the electron of an outer shell which leads to its ejection from the orbital position. The incident photon continues its path but is deflected. This scattered photon has lower energy and thus longer wavelength than the incident photon. Because it is not always consistent and systematic, the phenomenon is known as incoherent scattering. In medical radiography Compton scattering (figure 2.8) is the source of background noise in X-ray images while in industrial imaging it is important for low atomic number specimens.

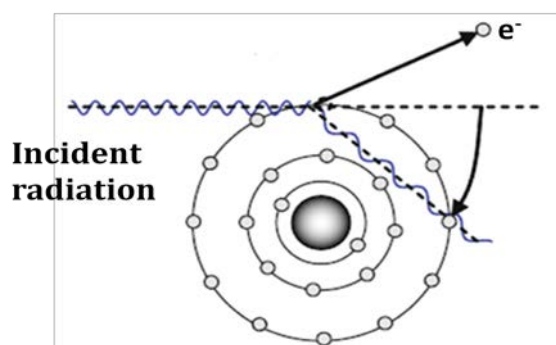


Figure 2.8: Compton Scattering [12].

2.3.4 Pair production

The pair production requires incident photons with energy greater than 1.02 MeV and it is significant at 10 MeV with high atomic number materials. During interaction, the high energy photon is absorbed by the nucleus and creates 2 particles with opposite electrostatic charges. They consist of an electron and a positron called pair production. The positrons disappear due to their short life. This positron annihilation releases 2 photons each possesses energy of 0.51 MeV (figure 2.9). The pair production is usually used in radiation therapy application and not in radiography.

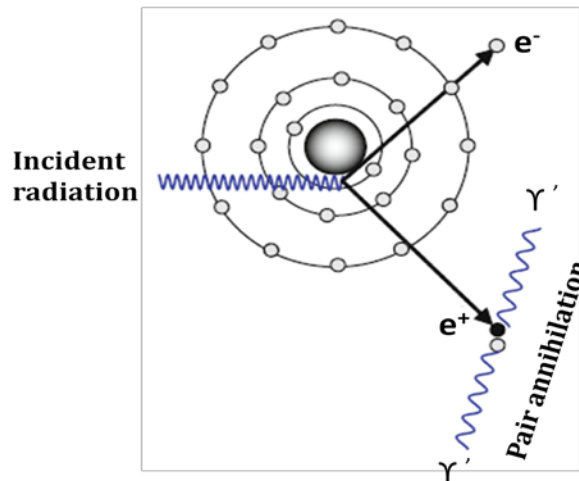


Figure 2.9: Pair Production [12].

2.4 X-Ray Fluorescence

As a result of X-rays interaction with matter, either a disturbance of the atom electron orbitals occurs or photons emission takes place. Fluorescence is a type of luminescence emitted when a substance absorbs an electromagnetic radiation. During emission, three events occur (figure 2.10); first, the excitation or the ionization of the substance; then, a vibrational relaxation of the excited state electrons. The final process is the emission of a photon and the return of the substance molecule to the ground state.

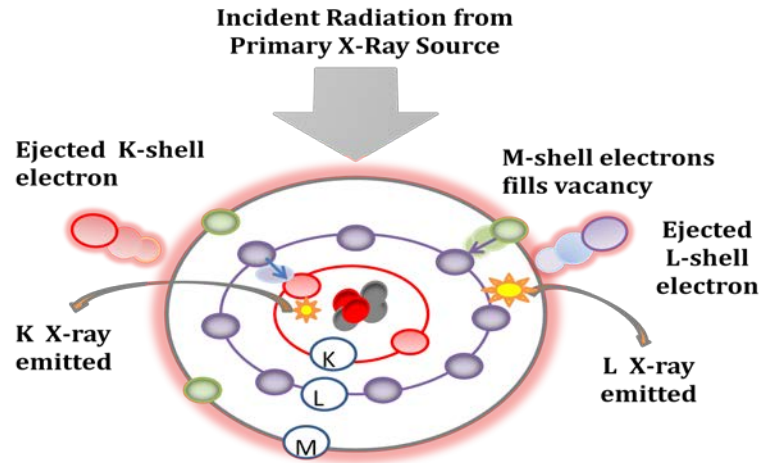


Figure 2.10: Fluorescence steps: X-ray absorption and fluorescent photon emission from different shells.

These three states, shown also in figure 2.11, represents what is known as “Jablonski energy diagram”, that is, the quantum mechanical process of fluorescence.

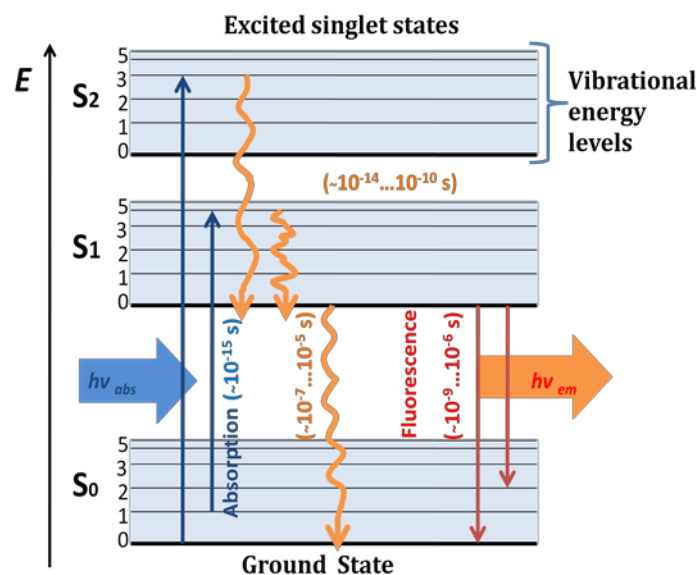


Figure 2.11: Jablonski energy diagram: S_0 is the ground state; S_1 , S_2 are the 1st & 2nd electronically excited states [13].

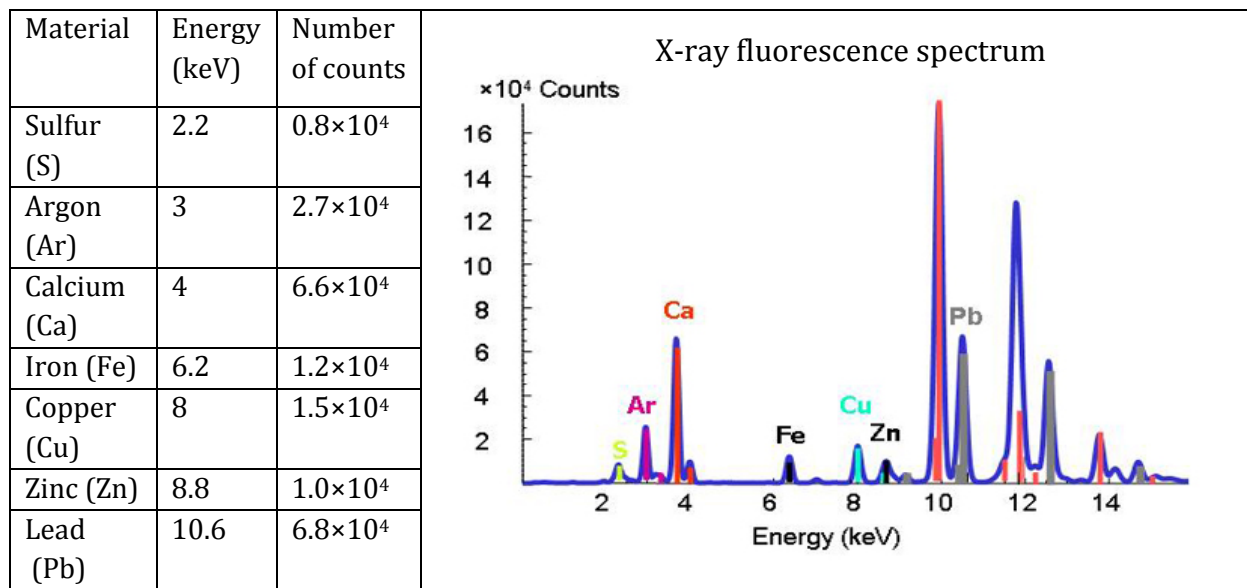
In the Jablonski energy diagram, the orange arrow represents the relaxation state from excited single states. Upon ionization, an electron is ejected from the atom leaving a vacancy in the inner shell. An electron from higher energy orbital makes a transition to fill the vacancy. This excess energy is given off by fluorescence emission. A combination of many transitions is possible. The emitted radiation is labeled K_α and k_β upon specific transition from L-shell and M-shell respectively. The emitted fluorescence, $h\nu_{em}$, has longer wavelength and therefore lower energy than the absorbed radiation $h\nu_{abs}$. In some cases the energy is transferred to another electron in the same atom. When the energy is sufficient enough this electron will be ejected. This phenomenon is called the Auger effect or the Auger electron and is considered as a “second fluorescence” [13], [14].

2.4.1 X-ray fluorescence features

The emitted X-ray fluorescence energies are considered as low energies but they are characteristics of the sample and reveal the element presence. Table 2.1 represents the X-ray fluorescence of few different materials with their corresponding ray paths. Each element has an X-ray fluorescence peak at a specific energy. These peaks constitute the data for the elemental composition analysis of the material.

As X-ray fluorescence (XRF) affects the inner shells of the element atoms, the XRF spectra shows that each element has an identifiable spectrum even if mixed with other elements.

Table 2.1: X-ray fluorescence spectrum showing the presence of different elements (Image Courtesy of ESRF).



2.4.2 X-ray source and fluorescence energies

The X-ray source energy is known from the type and working tension of the X-ray tube; while the fluorescence energy is computed based on Moseley's law. The principle is that the strength of the electrons bonds to the positively charged nucleus depends on the level they occupy. This is described by Bohr's atomic model in figure 2.12. The shells labeled K, L, M, and N with the innermost being K level and having the highest binding energy. In order to release an electron from the atom a minimum amount of energy is required.

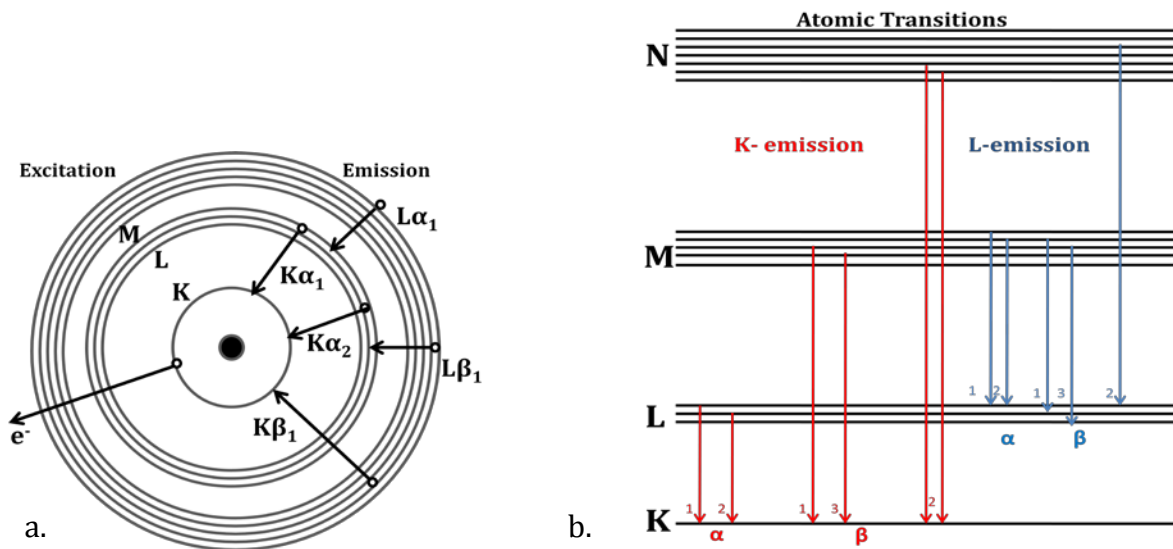


Figure 2.12: (a) Bohr's atomic shell model, (b) Diagram of energy levels showing the atomic transitions.

As described before, the emission of X-ray fluorescence is a characteristic radiation that depends on the element atomic number. This radiation contains information about the element type and the shell in which the electron-hole filling occurs. That's why it is specified as K-radiation, L-radiationetc, and the α , β with the numbering are used to differentiate between the shells and the sublevels of each shell as shown in figure 2.12(b).

In 1913, Henry Moseley discovered the relationship between the wavelength (energy) of the X-rays produced and the atomic number of the target metal used in the X-ray tube. He found also the proportionality between the energy of transition and the number of shells; for instance the radiation $K\alpha$ is less energetic than $K\beta$. Moseley's Law describes the relationship between wavelength of a spectral line and atomic number:

$$\lambda = \frac{K}{(Z - \sigma)^2} \quad (2.2)$$

For a given spectral line, K and σ are constants. For the K-lines σ is equal to 1 and for L-lines 7.4. The same expression is approximated for energy, it is equivalent to:

$$E(\text{keV}) = K(Z - 1)^2 \quad (2.3)$$

where Z is the atomic number;
 $K = 1.042 \times 10^{-2}$ for the K shell;
 $K = 1.494 \times 10^{-3}$ for the L shell;
 $K = 3.446 \times 10^{-4}$ for the M shell.

The importance of this determination is that this later equation is used to calculate the fluorescence energy for any atom [15].

2.5 X-ray detection

For a given application, a specific type of radiation detector is selected. It depends on the photons energy range and the needed efficiency and resolution. Many physical parameters are used to characterize and identify the X-ray detector such as detection efficiency, short response time, stability of operation and counting rate capability. In what follows, the function of each type of detector is defined and a detailed description of the detectors characteristics is explained.

2.5.1 Gas-filled detector

The gas-filled detector contains typical gases such as argon and helium. The principle is that when radiation passes through a specific gas, ionization of the molecules occurs. In order to accomplish a pulsed operation, a variable high voltage is applied between the two areas of the gas filled space. The free electrons will be attracted to the positive anode and the positive ions will travel through the negative cathode. A small current is produced from the collected charges (see figure 2.13). This current depends on the radiation quantity entering the chamber.

The electrical current measuring device consists of a resistor and a capacitor in parallel to the detector walls so that the anode will be at a positive voltage. The collected charges are reduced across the capacitor and a pulse is produced across the resistor. Depending on the amount of incident radiation and the voltage applied between 2 electrodes, we distinguish between 3 types of gas-filled detector detailed in table 2.2:

- The ionization chambers;
- The proportional counters;
- The Geiger-Muller (GM) counters.

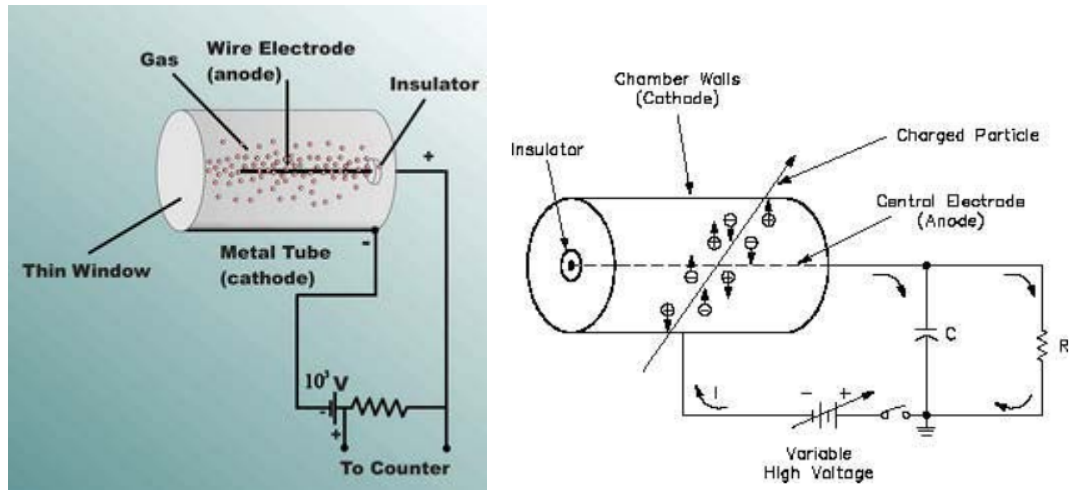


Figure 2.13: Gas-filled detector consisting of an insulating chamber, an anode and a cathode [16].

Table 2.2: Different Gas-filled detector types.

Ionization Chambers	Proportional Counters	The Geiger-Muller (GM) counter
<p>There is a wide range of shapes for the ionization chambers, but the effectiveness depends on the similarity between the material atomic number of chamber walls and the gas used.</p> <p>Usually the used gases are of low density and of low atomic number which leads to reduced intrinsic efficiency.</p> <p>But the produced current is efficaciously used for portable survey meters, diagnostic and therapeutic X-ray detectors.</p>	<p>Usually a single photons event is counted.</p> <p>The enclosed gas volume has a small diameter anode wire.</p> <p>They have a high output counting rate about 10^6 counts per second and a resolution about 20 % at 6 keV.</p> <p>They are used when moderate energy resolution is required.</p>	<p>The gas contained has specific properties, but the GM detectors are not usually used for X-rays and γ-rays due to its low count rate.</p> <p>The output pulse is independent of initial ionization and it is large enough to avoid amplification.</p>

The relationship between the ions collected and the applied voltage is shown in figure 2.14. When the voltage at the anode is low, a recombination phase between the electrons and the ions may occur. At a sufficient high voltage, primary ions are collected and the detector is considered in the ionization chamber region. In the proportional region, the higher voltage increases the ionization. Hence, the detector, known as proportional counter, creates larger number of electrons. In the GM region, higher voltage is applied and the gas around the anode is completely ionized. The detector is known as Geiger-Mueller counter and the large output pulse created is independent of the incident energy of radiation.

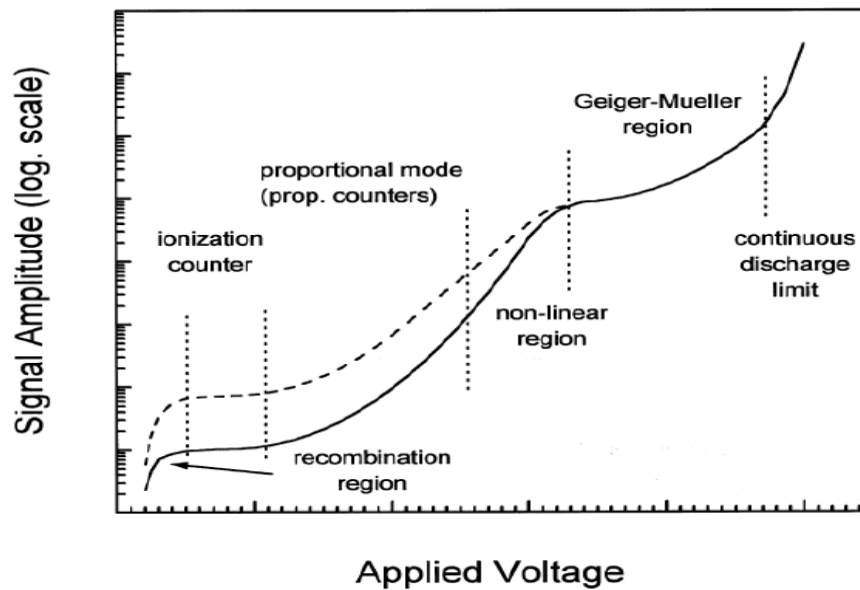


Figure 2.14: Different voltage regions corresponding to different gas-filled detector [17] .

2.5.2 Scintillator detector

The scintillation detector consists of a scintillator coupled optically with a photomultiplier tube (PMT) placed inside an evacuated tube as shown in figure 2.15. When X or γ -photons, as well as low energy β -particles, strike the scintillation crystal, a visible light is produced. The emitted visible light photons encounter a photocathode that generates electrons. The photocathode is also considered a focusing grid that transmits electrons to the PMT.

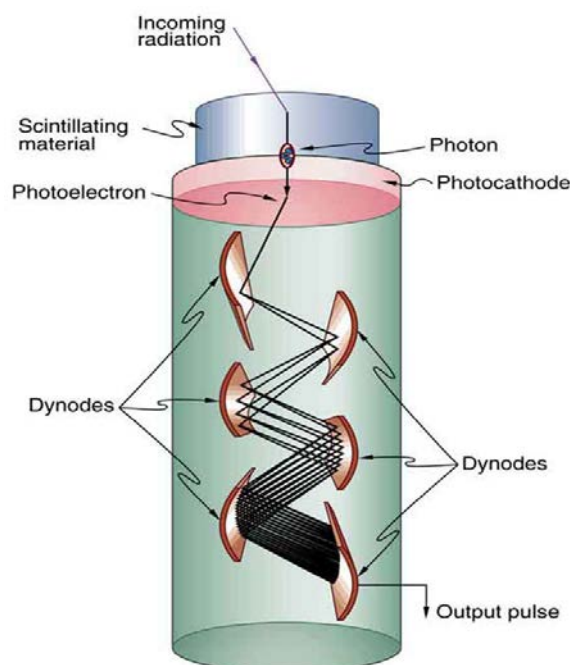


Figure 2.15: Scintillation detector [18].

The PMT function is to convert the ultraviolet and the visible light photons into an electrical signal and then amplify the signal. The evacuated glass tube holds 10 to 12 electrodes called dynodes and 1 anode. The potential difference between the

photocathode and the first dynode is equal to a kinetic energy that attracts all the photocathode emitted electrons. When an electron reaches the first dynode, about 5 electrons are emitted from the dynode. This process is repeated for each single electron through the chain of dynodes. At the end, the anode, which is the collection electrode, produces a voltage pulse. For each photon a voltage pulse is created. The output signal is amplified and counted. To ensure proper response of the PMT many variables are considered:

- The thickness of the photocathode must be sufficient to absorb photons and not too much thick in order to eject electron from its surface.
- The dynodes surface composition and geometry influence the process of electron multiplication. Total amplification of the PMT is the product of the individual amplifications at each dynode.
- The sensitivity of the photocathode must have a good quantum efficiency. The quantum efficiency is defined as the probability for the conversion of light to an electrical signal.
- High conversion efficiency produces superior energy resolution. The quantum efficiency is given as:

$$\text{Quantum Efficiency} = \frac{\text{number of photoelectrons emitted}}{\text{number of incident photons}} \quad (2.4)$$

The scintillation detector produces a large light output in the visible range. It can be in the pulse mode or in the continuous mode. Ionizing radiation causes effective scintillations in several crystals, liquids and plastics.

The variables of the detector that should be considered are:

- The material should be transparent at the wavelength of the emitted scintillation light.
- The spectral response of the photomultiplier tube must be in correlation with the spectrum emission.
- The light decay time constant must be as small as possible when the detector is used in the pulse mode.
- The linearity, which reflects the detector response. The emitted light must be directly proportional to the energy of the ionizing particle.
- Good efficiency of the material response in converting the excitation energy into fluorescence energy.

Depending on the intended applications, the scintillation materials or the detector type is selected. We distinguish between organic and inorganic materials as follows (table 2.3):

Table 2.3: Properties of organic and inorganic scintillator.

Organic Scintillator	Inorganic Scintillator
<ul style="list-style-type: none"> - The mechanism that occurs is the fluorescence of a single molecule and independent from the physical state. - Decays are within few nanoseconds. - Three types are distinguished: <ul style="list-style-type: none"> - Pure organic crystals. - Liquid organic solutions: by dissolving an organic scintillator in a solvent. - Plastic scintillator: by dissolving and polymerizing. It is characterized by its fast timing work. 	<ul style="list-style-type: none"> - The mechanism depends on the structure of the crystal lattice of inorganic material. - Usually absorption of radiation lifts electrons from valance to conduction band. In a pure crystal, electrons can never be found in a band gap of energies. In order to emit photons efficiently, small amounts of impurities are added to the crystal. The impurities, called activators, create energy state in the forbidden band of the crystal. Hence the energy levels become narrower, the emitted photons have longer wavelengths and are in the visible range. For instance, trace amounts of Tl are added to the NaI as an impurity for better detector efficiency. - The inorganic materials can be solid, liquid and gaseous. The popular ones are: <ul style="list-style-type: none"> - Alkali-halide: <i>NaI(Tl)</i>, <i>CsI(Tl)</i>; these are the commonly used crystals due to their good energy resolution. - Cerium-activated; - Glass-activators like boron and lithium; - Gases like noble gas.

2.5.3 Semiconductor detectors

Among detectors the semiconductors have the highest performance and the highest resolution. The constituents' materials act either as an insulator or as a conductor. Its principle is similar to the gas-filled detectors where electron-hole pairs are produced. They are made of single crystals that are highly purified like *Germanium* and *Silicon*. The semiconductor detector is also known as "solid-state detector" or "solid scintillator" due to the solid band gap that the compound crystal has. It is usually between 1 to 5 eV.

The structure of the semiconductors detectors is a "P-I-N" diode. It is an arrangement of three layers referring to "Positive doped area - Intrinsic area - Negative doped area". When a reverse bias is applied across the diode, a depletion region is created. When a photon interacts within the region, electrons and holes of the depletion region act as charge carriers. Then, they are swept and collected by their respective electrodes. A resultant charge is amplified and converted into a voltage pulse that is proportional to the incident photon energy. To ensure high counting efficiency, especially when we have high-energy photons, a large amount of pure material is needed.

2.6 Detector characteristics

Most radiation detectors have the same concept; an incident ray strikes the transducer part of the detector producing an excitation or an ionization effect (figure 2.16). The ionization effect depends on the initial energy of the incident beam. Two phases represent the detecting transducer. A physical phase of detection coupled with an electronic phase. Hence, during the electronic phase the transducer converts the physical product into a useful electrical signal.

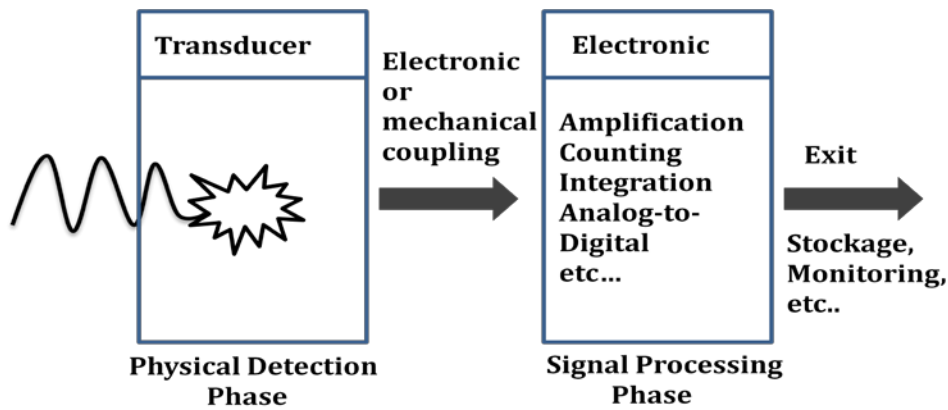


Figure 2.16: Diagram showing the ray detection steps.

In order to determine the occurrence of radiation striking the transducer, the detector must have a high absolute efficiency, a good resolution and a capability of beam stopping. These characteristics are defined in details.

2.6.1 Detector's resolution and efficiency

The detector's resolution is quoted as a measure of the width of a single energy peak at a specific energy. To be more specified, it is the '*Full Width of a peak at its Half Maximum height*' known as FWHM. It refers to the separation of peaks within a spectrum and it is expressed in absolute keV or as a percentage. The lower the FWHM, the better the resolution a detector has in resolving peaks [16].

Moreover, the ability to differentiate between photons of different energies and between close energies is called the energy resolution. Ideally, if we send a monochromatic beam to the detector we should observe a delta impulse. In fact, we have a Gaussian one as shown in figure 2.17 and it is given by:

$$\text{Energy Resolution} = \frac{FWHM}{\text{Pulse Height at center of peak}} \times 100\% \quad (2.5)$$

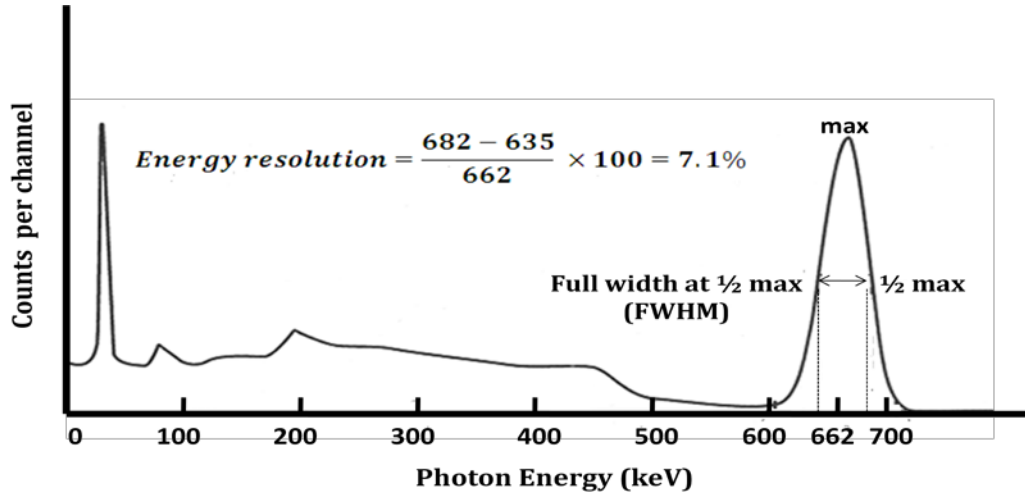


Figure 2.17: Detector resolution; the width is usually measured at half the maximal height of the peak [17].

The detector's efficiency, is a measure of how many pulses occur for a given number of incident photons. We distinguish between absolute efficiency, intrinsic efficiency and relative efficiency.

The absolute efficiency, referred to as the total efficiency. It is the ratio of the number of counts produced by the detector to the number of rays emitted by the source during the same time interval. Practically, sources emit rays in an isotropic manner. Among the whole incident beam only a fraction interacts with the detector and the remaining are either absorbed before reaching the detector or continue their way without being detected.

$$\text{Absolute efficiency} = \frac{\text{Number of photons Detected}}{\text{Number of photons Emitted}} \quad (2.6)$$

Accordingly, it depends on:

- The detector geometry and its orientation with respect to the source.
- The probability of interaction within the detector or the detector capability of beam stopping.

The detection probability is given as follows:

$$P_{\text{detection}} = P_{\text{interaction with object}} \cdot P_{\text{geometrical}} \cdot P_{\text{intrinsic}} \quad (2.7)$$

To perceive the geometrical probability, consider a cylindrical detector with a point source at a distance d on the detection axis (see figure 2.18). If the source is emitting the radiation isotropically, the probability that a particle emitted at an angle θ reaches the detector is:

$$P(\theta)_{\text{geometrical}} = \frac{\Omega}{4\pi} \quad (2.8)$$

where Ω is the solid angle under which the detector is seen from the source.

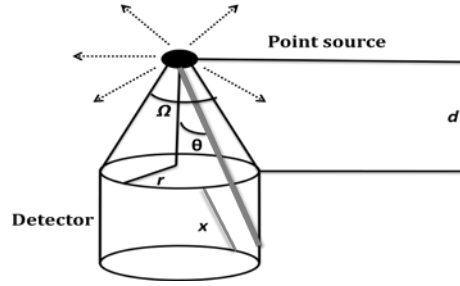


Figure 2.18: Detection efficiency computation [19].

The probability that a particle hitting the detector will have an interaction within the detector is given by the intrinsic probability:

$$P_{intrinsic} = \left[1 - e^{\left(\frac{-dt}{dl} \right)} \right] \quad (2.9)$$

where dt is the traveled distance within the detector; dl is the averaged traveled distance of an X-ray photon. The total efficiency is found by integrating the previous relation over the surface of the detector. It is divided into 2 parts: the intrinsic efficiency ε_{int} and the geometric efficiency ε_{geom} :

$$\varepsilon_{tot} = \varepsilon_{int} \cdot \varepsilon_{geom} \quad (2.10)$$

The intrinsic efficiency is the fraction of the number of photons entering the detector which interact in the detector material. It is determined by the detector ability to stop the ray of interest. The intrinsic efficiency is also called the '*quantum detection efficiency*' or QDE. It is determined by the detector thickness, density and atomic number. For mono-energetic and parallel beam photons detection, the intrinsic efficiency is the interaction probability and is given by:

$$P_{\gamma(interaction)} = 1 - e^{-\mu \cdot dt} \quad (2.11)$$

where dt is the detector thickness and μ is the attenuation coefficient.

This probability depends on the efficient section of interaction of the incident radiation inside the reaction medium of the detector. Hence, the intrinsic efficiency depends on type of radiation, its energy and the material of the detector.

However, the geometric efficiency is defined as the number of incident photon rays reaching the detector in a time interval over the number of photon rays emitted from the source at the same time interval. For a point source detected by a simple cylindrical detector, as shown in figure 2.19, the geometric efficiency decreases with longer distance between the source and the detector depending on the inverse square

law. The inverse square law is: $I = \zeta/4\pi r^2$, where ' I ' is the intensity of radiation per unit area, ' ζ ' is the source emission rate and ' r ' is the radius.

The inverse square law is illustrated as follows in figure 2.19.

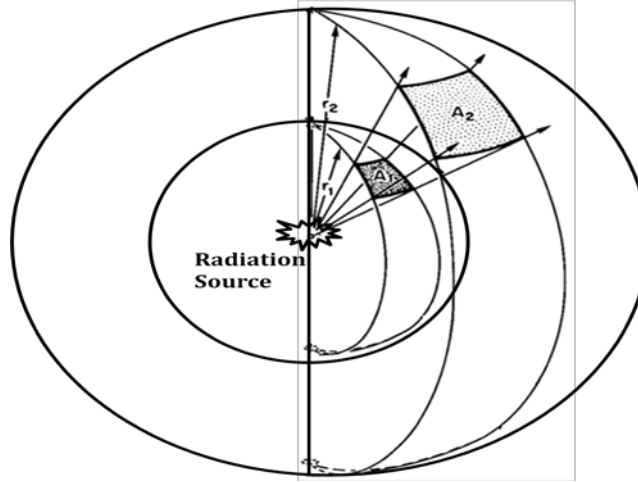


Figure 2.19: Inverse Square Law illustration [17].

As the distance from the radiation source increases from r_1 to r_2 , the radiations passing through A_1 are spread out over a larger area A_2 . So ' A ', which is the unit area, is proportional to r^2 and the intensity of radiation per unit area drops to $1/r^2$.

For a point source the detector efficiency is $g_p = \frac{a}{4\pi r^2}$, where ' a ' is the detector surface area and ' r ' is the distance from the point source. In the case when we have a small distance r between the source and the detector, the area of the detector is $S = \Omega r^2$ where $\Omega = 2\pi (1 - \cos \theta)$.

The geometric efficiency is then:

$$\varepsilon_{geom} = \frac{S}{4\pi r^2} = \frac{\Omega r^2}{4\pi r^2} \quad (2.12)$$

2.6.2 Detector's response time

The "detector's response time" or "dead time" is the time taken by the detector to produce a signal after receiving the radiation. More specifically, when an event is recorded the dead time is the time during which the signal is unable to record another event. This process is also called pulse resolving time that is expressed as τ . Usually, the counting system comprises many components; the detector, the pulse amplifier, the pulse height analyzer, the scalar which counts the pulses and the computer interface. Hence, one of these components or more can contribute a dead time to the system. The main causes of dead time are either an overlap pulses or counting losses.

In general, common X-ray detectors have different modes of operation. In order to determine the occurrence of radiation striking the detector, they either count single photons or provide measurements of count rate or total flux, and some of them measure the energy of radiation, the position of each X-ray and the time of radiation arrival. The counting system is characterized by two different behaviors; the paralyzable type and the non-paralyzable type. A diagram of recording events is shown in figure 2.20. In a non-paralyzable detector if an event occurs during the dead time τ of a preceding event, the second event will be ignored and the detector will reach a saturation rate. For a paralyzable system, a recorded event produces a dead time τ whether counted or not. Hence, for a very high interaction rate, after the first interaction the detector will indicate a zero count rate. In the non-paralyzable system, events are lost when they occur within a time τ of a preceding recorded event; whereas in the paralyzable system they are lost if they occur within a time τ of a preceding recorded event whether or not this event is recorded.

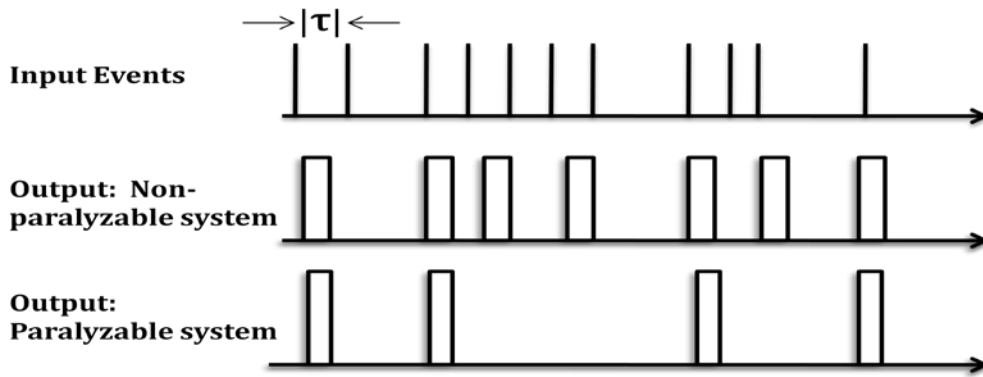


Figure 2.20: Recorded events on a detector for a paralyzable and a non-paralyzable system [17].

2.6.3 Detector's operation modes

As a result from the energy deposited in the detector we distinguish two modes of operation; the current-integration mode and the pulse-counting mode.

The current-integration mode measures average rate of photons flux. The generated electrical signal in the current mode is coupled with an ammeter circuit as shown in figure 2.21. The ammeter has a response time T during it the signal is generated. When we have a sequence of events the acquired signal can be expressed as a function of time:

$$I(t) = \frac{1}{T} \left(\int_{t-T}^t i(t') dt' \right) \quad (2.13)$$

Expressed also in function of the energy 'E' as:

$$I = \int_0^{\infty} \mu(E) E dE \quad (2.14)$$

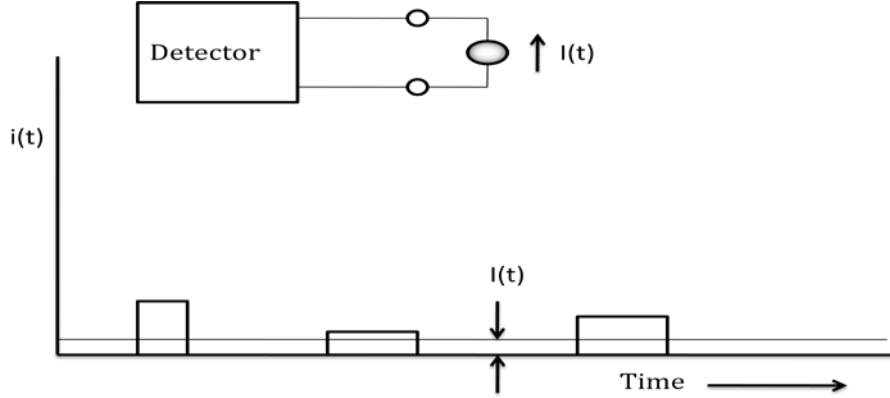


Figure 2.21: The current mode configuration [17].

Consequently, the current is the mean rate of these impulses and is proportional to the interactions frequency and to each interaction charge. The current is represented by:

$$I_0 = r \cdot Q = r \cdot \frac{E}{W} \cdot q \quad (2.15)$$

where E is the average energy deposited per event; W is the average energy required to produce a unit charge pair; q is the electron charge; r is the interaction rate.

A net current signal is therefore formed from the average signals of individual interactions, and this will avoid dead time losses and can be used in very intense radiation field.

Concerning the pulse-counting mode, a separate electrical pulse is generated and the signal from each interaction is processed individually. The generated electrical signal is coupled to an RC circuit. The detector electrical voltage pulse has amplitude V_{max} which depends on the total charge Q during the collection time. It is expressed by $V_{max} = Q/C$. In figure 2.22 (A), an equivalent circuit of an impulse at the detector output is represented where R and C are the resistance and the capacitance of the circuit. $V(t)$ is the time (t) dependent voltage produced. In (B), a current pulse resulting from the interaction of a single quantum of the detector. The total charge Q is the integration of the area current $I(t)$ over the collection time. The resulting voltage pulse is drawn in (C). The time constant ' RC ' is chosen to be higher from the charge collection time and less than the average time that separates the arrival of photons to the detector. This mode is most popular as it has higher sensitivity and carries useful information [17].

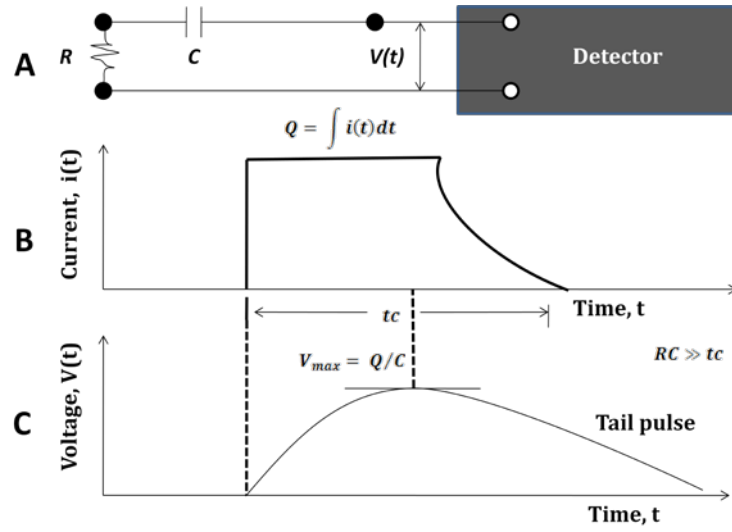


Figure 2.22: Detector pulse mode [20].

The pulse-counting mode is expressed by:

$$N = \int_{E_{min}}^{E_{max}} N_{(E)} dE \quad (2.16)$$

Where $N_{(E)}$ is the number of photons at specific energy E .

As illustrated in figure 2.23, the polychromatic spectrum can be defined by the counting spectrum window formed by $[E_{min} - E_{max}]$. This window can be narrowed to select an X-ray fluorescence beam.

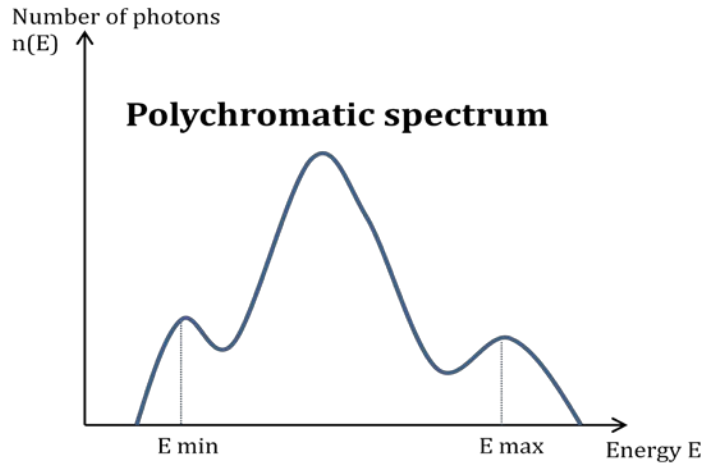


Figure 2.23: Counting spectrum defined by E_{min} & E_{max} .

2.7 Conclusion

X-ray, used in many fields, is a form of radiation whose wavelength is on the order of Angstrom and corresponding photon energy on the order of keV. As it can be generated with specific spectrum and known parameters, it can be employed in tomography

systems. Many reasons prompt the use of X-ray to obtain fluorescence tomography application. X-rays have sufficient energy to cause atom ionization and subsequent characteristic fluorescence. They can penetrate most opaque and thick matter. The penetration depth and the interaction type vary over the X-ray spectrum. This allows the photon energy to be adjusted for the application. Through X-rays, high resolution images can be acquired. All of these characteristics have a strong impact on the system settings optimization.

Chapter 3 Transmission & Fluorescence X-Ray tomography

3.1 Introduction

This chapter is dedicated to describe transmission and emission tomography, being necessary for X-ray Fluorescence Tomography. In general, tomography is a non-invasive imaging technique and has a widespread application in many scientific fields. It refers to a cross-sectional imaging of a sample as shown in figure 3.1. The origin of the word 'tomography' comes from the Greek words 'tomos' meaning to cut or section and 'graphein' meaning to write. It is based on the acquisition of projections resulting from emission or transmission of X-rays. In conventional X-ray transmission tomography, these projections correspond to the attenuation of X-rays through the sample. However, in emission tomography the projections represent the amount of radiation released or given off by the sample itself.

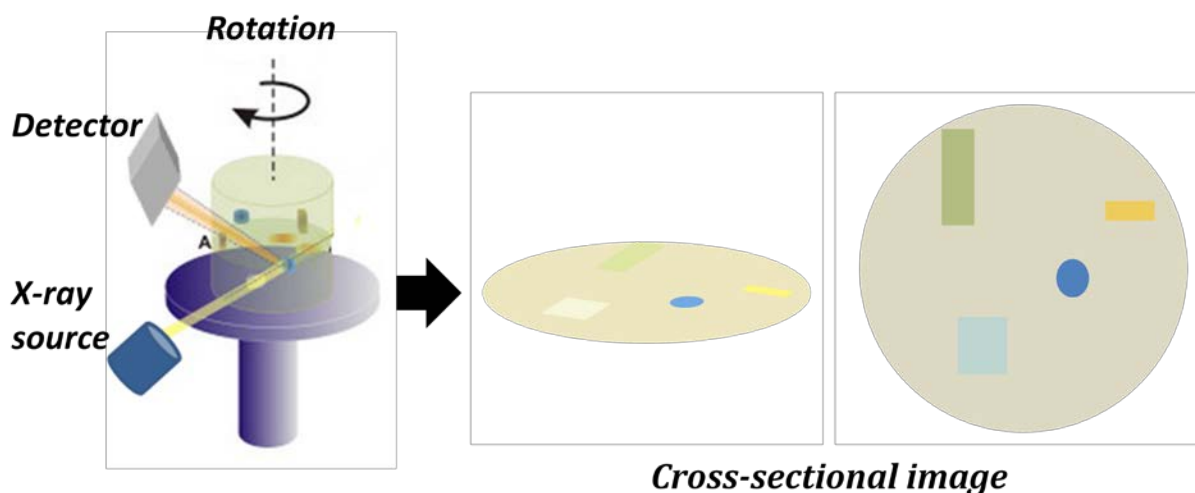


Figure 3.1: Data acquired from different views used to reconstruct a cross-sectional image.

3.2 Tomography basic principle

3.2.1 Transmission tomography

For the scanning procedure using X-rays beams, a set of lines is covering the entire field of view either in parallel-beam geometry (figure 3.2(a)) or in fan-beam geometry (figure 3.2 (b)). This process is repeated for a large number of angles (figure 3.2 (c & d)). The basic principle during the scanning is based on Beer's Lambert Law. Normally, the sample contains different materials and is considered a heterogeneous absorber. The X-ray source employed in this project is polychromatic. Therefore, for each wavelength of the X-ray source the emerging beam can be expressed as:

$$N_{(E)} = N_{0(E)} e^{[-\mu(E)x]} \quad (3.1)$$

where E and N_0 are the energy and the the incident beam number of photons respectively. x represents the path crossed by the radiation. μ is the linear attenuation coefficient. The linear attenuation coefficient typically expressed by cm^{-1} is a function of:

- The energy of incident radiation.
- The atomic number of different components.
- The physical density of different components.

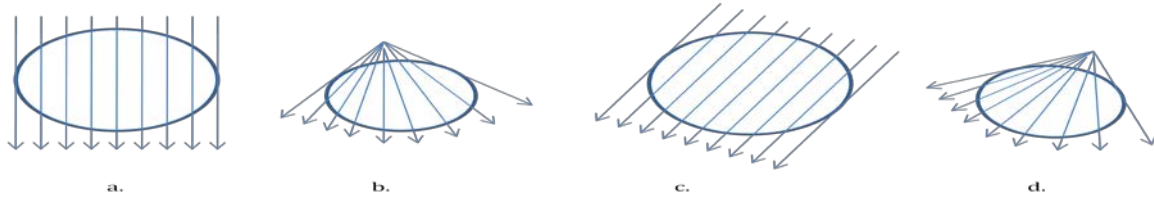


Figure 3.2: (a) Parallel-Beam Geometry, (b) Fan-Beam Geometry, (c) & (d) Same geometries in different angles [21].

In tomography, the attenuation coefficient characterizes each volume element (voxel) of the sample. These are shown in figure 3.3 along a single scan line or a radiation path.

μ_1	μ_2	μ_3	μ_4	$N = N_0 e^{-(\mu_1+\mu_2+\mu_3+\mu_4)x}$
---------	---------	---------	---------	---

Figure 3.3: Physical principle of 1-D tomography [22].

For a physical density distribution, the integral attenuation is involved in every single measurement. A space of interaction is shown in figure 3.4.

In the case of heterogeneous absorber, the sample becomes a distribution of the various materials expressed as $\mu(x, y)$. When the beam is polychromatic, called also multi-energetic, the scanning model will be:

$$N_i = \int N_{i0}(E) e^{(-\sum \mu_{ij}(E)\Delta x_{ij})} dE \quad (3.2)$$

where E is the specific energy of the incident beam.

After a number of measurements, the single μ_{ij} values are obtained. For each angle or projection, a complete series of data is automatically obtained, and only rotations are required [22][23]. This is illustrated in figure 3.4.

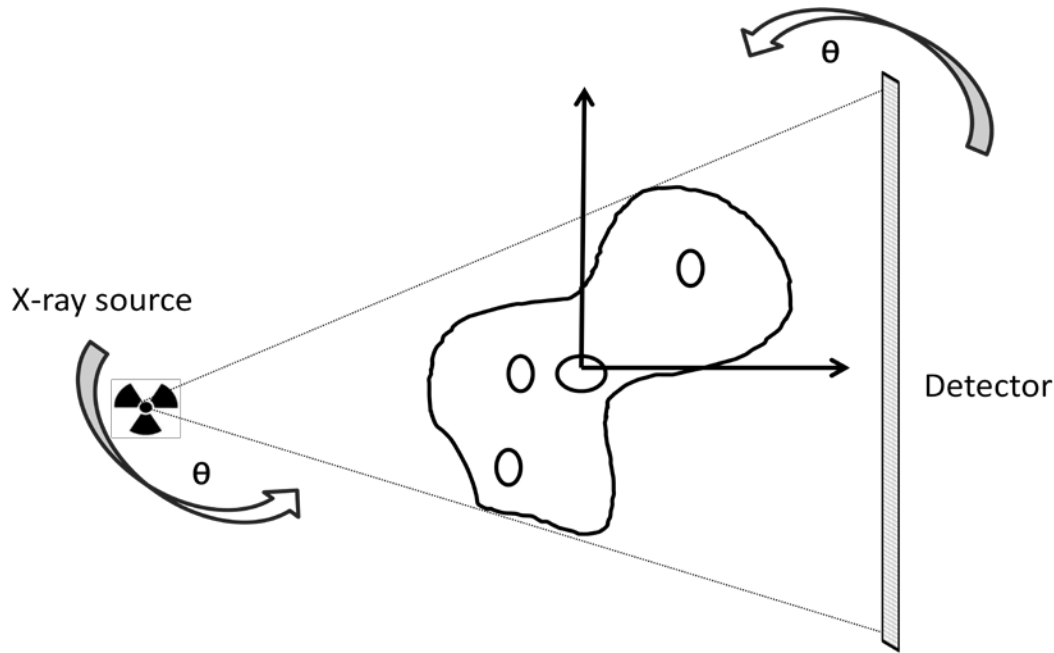


Figure 3.4: Transmission tomography

3.2.2 Emission tomography

As described in the previous chapter, when an incident X-ray photon gives all of its energy to an electron of the material, the photoelectric absorption occurs. The emitted fluorescence photons are characteristics of the material. Specific detectors are used to count the number of these fluorescent photons. The technique consists of collecting data from many equidistant angles. There are two experimental setups for scanning. Either the system source, collimator and detector rotate around the sample or the sample itself will be rotating (see figure 3.5). On both cases projections are well acquired and the accuracy depends on the efficiency of the detector. The detector crystals are considered as an array of pixel where each one corresponds to a different area of the object. The detector collimator contributes in reflecting accurately the originating location of the X-ray fluorescence.

Before reaching the detector, the radiation encounters the collimator. This latter is a pattern of holes and absorbing materials like lead or tungsten that allows the projections traveling along certain directions to be detected. The measurement of the intensities is converted into numbers. This digital data constitutes the basics for

applying an image reconstruction algorithm. The obtained result is a well-defined image reflecting elements inside the sample [24].

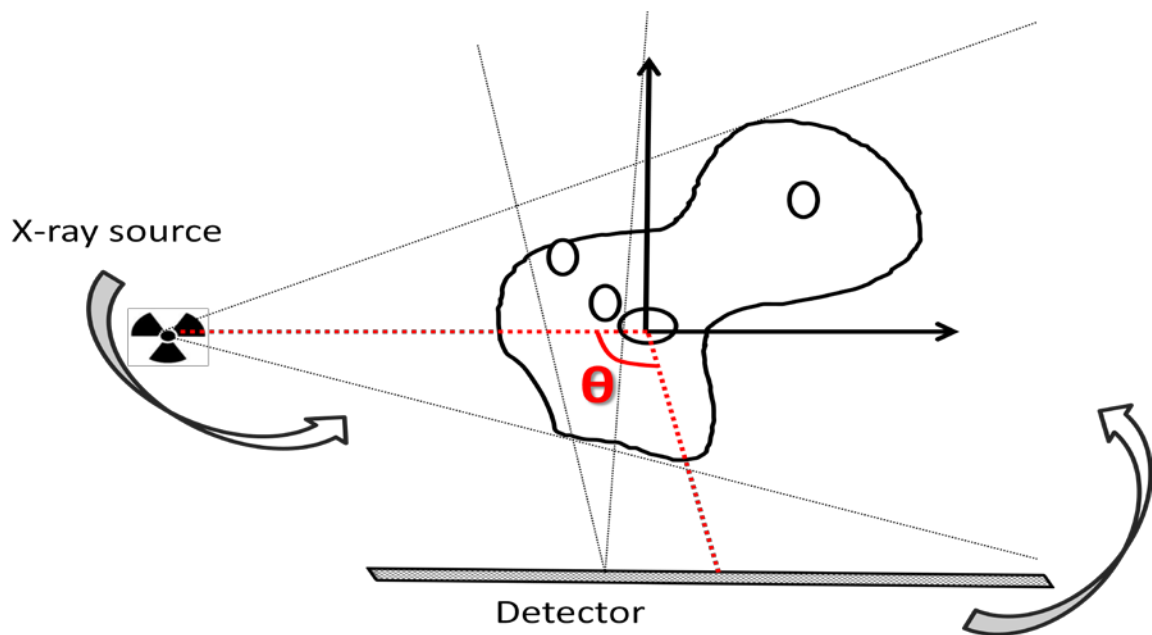


Figure 3.5: Emission tomography.

3.3 Image reconstruction techniques

This section is dedicated to describe what a numerical image is and how an image is reconstructed. Based on values measured by the detector, image reconstruction comprises the collection of a series of data around the sample in order to reconstruct a cross-sectional view image of the specimen [25].

3.3.1 Reconstruction methods

The different reconstruction algorithms are classified into two main sets, analytical and iterative as shown in figure 3.6.

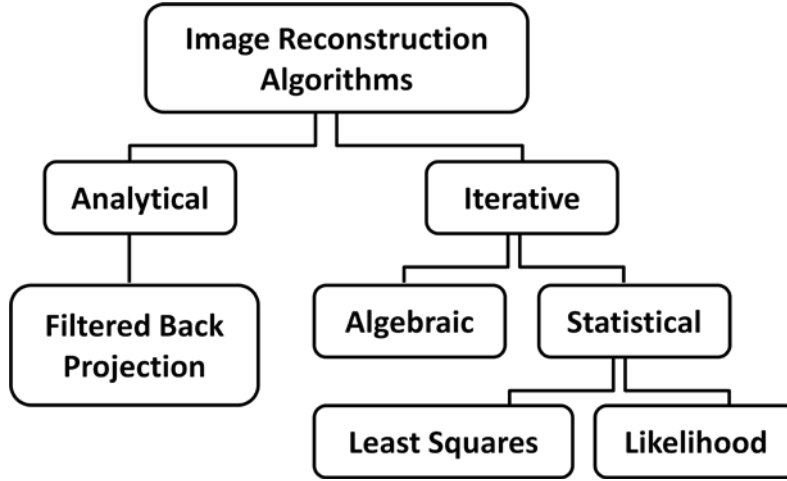


Figure 3.6: Reconstruction algorithm classification.

The more widely used algorithms are Filtered Back Projection (FBP), Conjugate Gradient (CG), Maximum Likelihood Expectation Maximization (MLEM) and the Maximum A Posteriori Expectation Maximization (MAPEM).

3.3.2 Principle of projection acquisition and Radon Transform

A 2-D image represents a slice distribution of a continuous space that is reconstructed independently. In figure 3.7, a distribution of linear attenuation coefficient is represented by $\mu(x, y)$. In this slice, the distribution is zero outside $\mu(x, y)$ whose diameter is 'FOV' the field of view. The X-rays beams make an angle θ with the y -axis.

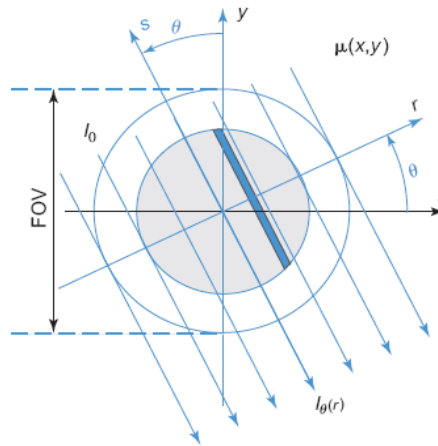


Figure 3.7: Parallel beam geometry with coordinate system [21].

The incident or the un-attenuated intensity of the X-ray beams is $I_0(r)$ at angle θ . By rotating the (x, y) plane by an angle θ , a new coordinate system (r, s) is defined according to:

$$\begin{bmatrix} x \\ y \end{bmatrix} = \begin{bmatrix} \cos \theta & -\sin \theta \\ \sin \theta & \cos \theta \end{bmatrix} \begin{bmatrix} r \\ s \end{bmatrix} \quad (3.3)$$

Each intensity profile $I_\theta(r)$ is a function of an attenuation profile and is given by:

$$I_\theta(r) = I_0 \cdot e^{-\int_{L_{r,\theta}} \mu(x,y) ds} \quad (3.4)$$

$$= I_0 \cdot e^{-\int_{L_{r,\theta}} \mu(r \cdot \cos \theta - s \cdot \sin \theta, r \cdot \sin \theta + s \cdot \cos \theta) ds} \quad (3.5)$$

where $L_{r,\theta}$, also called line of response, is the line that makes an angle θ with the y -axis at distance r from the origin.

Mathematically, the projection operator which is the transformation of any function $\mu(x,y)$ into its sinogram $g(r,\theta)$ is defined by the Radon Transform. This is defined as follows:

$$g(r,\theta) = -\ln \frac{I_\theta(r)}{I_0} \quad (3.6)$$

$$= \int_{L_{r,\theta}} \mu(r \cdot \cos \theta - s \cdot \sin \theta, r \cdot \sin \theta + s \cdot \cos \theta) ds \quad (3.7)$$

The Radon Transform is the line integral of the values of $\mu(x,y)$ along the line $L_{r,\theta}$.

$$g(r,\theta) = \Re \{ \mu(x,y) \} \quad (3.8)$$

$$= \int_{-\infty}^{\infty} \mu(r \cdot \cos \theta - s \cdot \sin \theta, r \cdot \sin \theta + s \cdot \cos \theta) ds \quad (3.9)$$

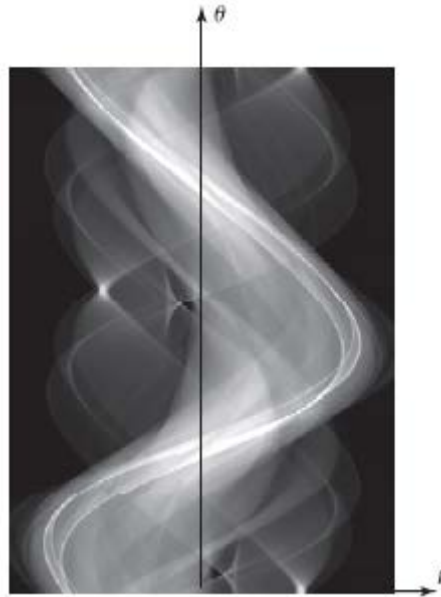


Figure 3.8: A sinogram $g(r,\theta)$ representing values of each angular position on each detector pixel [21].

When all the projections are stacked in a 2D dataset $g(r, \theta)$, a sinogram is obtained (see figure 3.8). The origin of the name “sinogram” corresponds to the sinusoidal shape formed by the set of projections.

The sinogram horizontal axis (r -axis) represents the pixels quantity of the detector and the vertical axis (θ -axis) corresponds to the angular position of the detector. In the sake of finding the distribution of μ in the slice of interest from the sinogram, analytical or iterative algorithms are applied [21][26].

3.4 Transmission tomography

3.4.1 Direct Fourier reconstruction

The direct Fourier reconstruction is an algorithm that calculates $\mu(x, y)$ based on the Fourier transform, Fourier slice theorem and inverse of Fourier transform.

For each projection profile “Fourier Transform (FT)” and “Inverse Fourier Transform (IFT)”, described in Annex A, are applied as follows:

- 1- Calculate the 1D FT noted by ' F_1 ' of all projections $g(r, \theta)$: $F_1\{g(r, \theta)\} = G_\theta(L)$.
- 2- Put all the values of the 1D function $G_\theta(L)$ on a polar grid to obtain the 2D function $G_\theta(L, \theta)$. The data samples need to be interpolated to a Cartesian rectangular grid in order to obtain $F(L_x, L_y)$.
- 3- Calculate the 2D IFT F_2^{-1} of $F(L_x, L_y)$.

In order to generate values on a polar grid in step 2 the ‘Central Slice Theorem’, also called the ‘Fourier slice theorem’ is needed. As illustrated in figure 3.9, the Fourier transform of the projection at angle θ is equal to the two-dimensional Fourier transform of the object, evaluated in the direction θ in Fourier transform space.

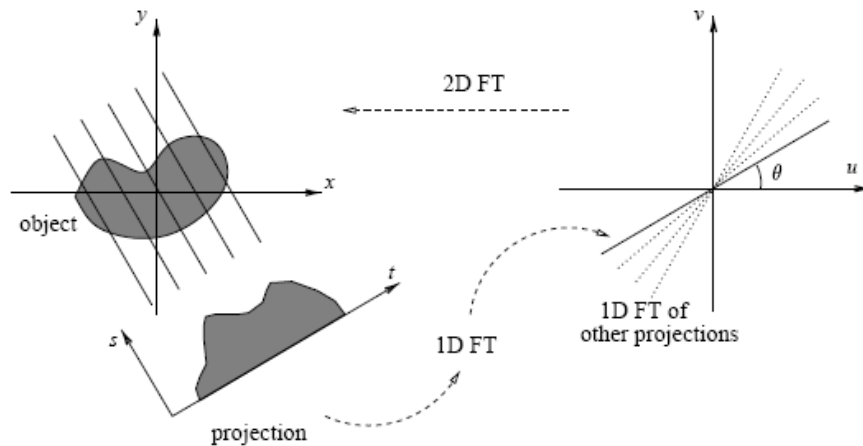


Figure 3.9: Relation between image space, Radon space and Fourier space according to Fourier slice theorem [27].

The drawback of this latter method is that the interpolation leads to image artifact. Thus, another reconstruction approach which is the 'Filtered Back Projection' is more popular.

3.4.2 Filtered Back-projection (FBP)

The Back-Projection operator reconstructs the distribution $\mu(x, y)$ or, more specifically, the function $f(x, y)$ from the sinogram $g(r, \theta)$ as follows. Along a particular scanning line (r, θ) (shown in figure 3.10) the value of the projection $g(r, \theta)$ is assigned to all points (x, y) along that line. This is integrated or repeated for all θ ranging from 0 to π because projections acquired between π and 2π do not provide new information, as they are symmetric. This is given by:

$$f_{Back\ Projection}(x, y) = B \{g(r, \theta) \quad (3.10)$$

$$= \int_0^\pi g(x \cdot \cos \theta + y \cdot \sin \theta, \theta) d\theta \quad (3.11)$$

To better understand the filtered back-projection, a specific situation is illustrated in figure 3.10. An object shown as a 2-dimensional image consists of a group of points. Projections of this object are taken from different angles and the sum of all intensity along each projection path is presented (figure 3.10(a)). In order to reconstruct the image, from each projection we re-distribute the activity in equal amount back to its original path (figure 3.10 (b)). This is called the summation algorithms as we are applying back-projection to projection data. The last step is the accumulation of ray-sums from all angles over 360° of all the rays passing by this point.

As shown in figure 3.10 (b), the approached image is unsatisfactory as it is blurred and has a cone like shape. Therefore, a simple back projection is not sufficient to reach a good image. In order to obtain and sharpen the image, a filter must be applied to the projections as illustrated in figure 3.10 (c).

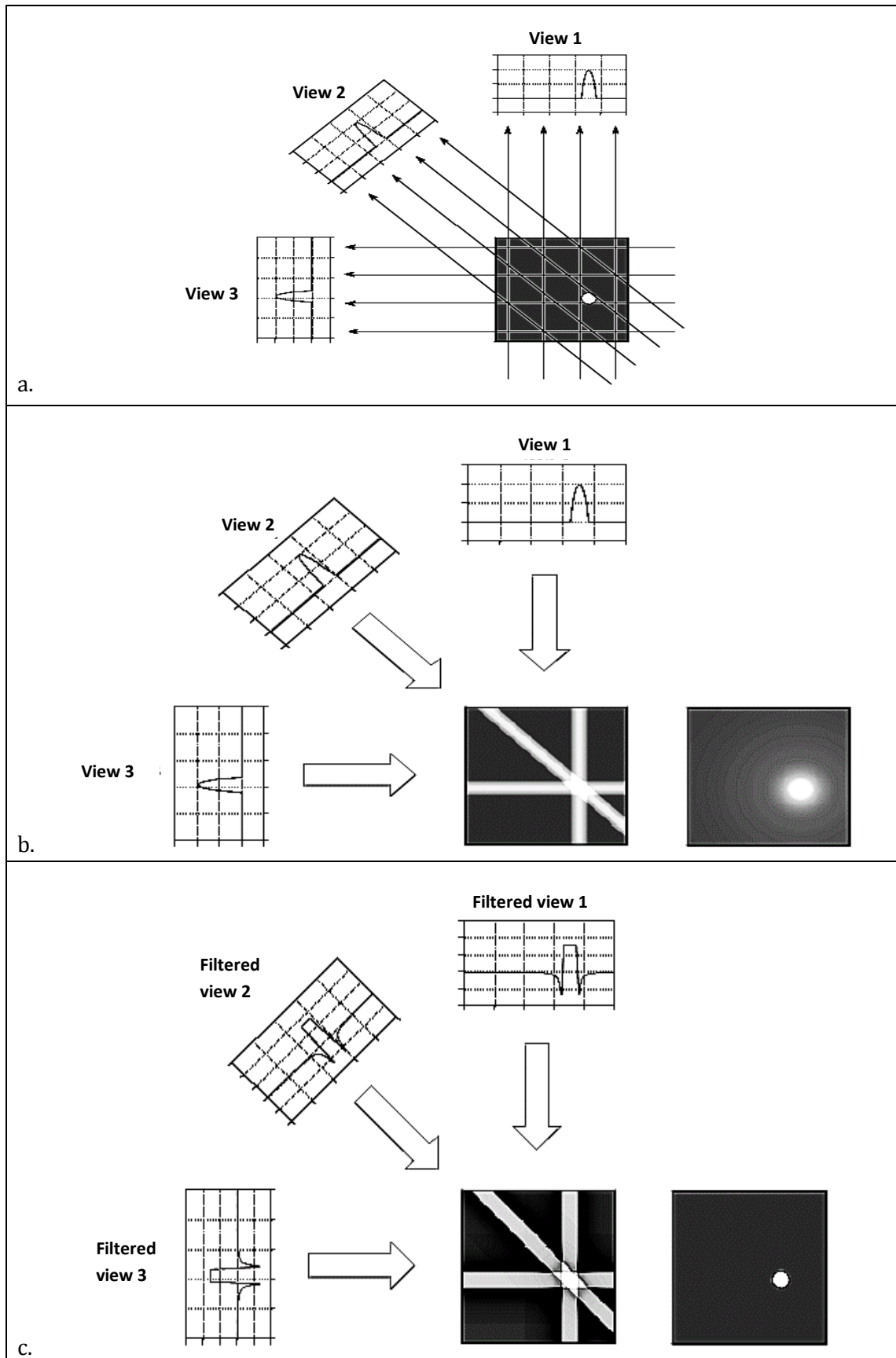


Figure 3.10: The Back-projection process [28].

Replacing the integral value in the equation 3.8 by a sum, a discrete version of back-projection is obtained. It is given by:

$$f_{Back\ Projection}(x_i, y_i) = B \{g(r_n, \theta)_m\} \quad (3.12)$$

$$= \sum_{m=1}^M g(x_i \cdot \cos \theta_m + y_i \cdot \sin \theta_m, \theta_m) \Delta \theta \quad (3.13)$$

Let $s_m = x_i \cdot \cos \theta_m + y_i \cdot \sin \theta_m$ so

$$f_{Back\ Projection}(x_i, y_i) = \sum_{m=1}^M p(s_m, \theta_m) \Delta \theta \quad (3.14)$$

where M is the number of projections acquired, θ_m is the angular position of the detector, $(x_i \cdot \cos \theta_m + y_i \cdot \sin \theta_m)$ is the location along the detector and $\Delta \theta$ is the angular step between 2 successive projections.

Several frequencies are usually included in any image. Using the Fourier Transform, an image can be split up in several components, each corresponding to a given frequency. Once the data has been transformed to the frequency domain it can be filtered efficiently. Data filtering is necessary to obtain the final image. Each filter has its specific characteristics. They slightly differ in their function. When there are sharp edges, some filters will smooth very heavily but degrade the final image resolution. Other filters will smooth slightly and maintain a high resolution. Many typical filters are available such as Hamming filter, Butterworth filter, low pass cosine filter, Weiner filter, Ramp filter, etc. No matter which filter is applied on the data, the purpose is to have an image pleasing to the eye and relatively free from noise. The end result is to get out the (x, y, z) information regarding the spatial distribution. As the filtered data or the smoothed data is in the frequency domain, the Inverse Fourier Transform (IFT) is applied to transform it back to the spatial domain [29]. Using the Ram-Lak or the ramp filter, the FBP can be formulated as follows:

$$f(x, y) = \int_0^\pi \int_{-\infty}^\infty G(k, \theta) |k| e^{i2\pi k r} dk d\theta \quad (3.15)$$

with $r = x \cos \theta + y \sin \theta$

$|k|$ is the frequency response of the ramp filter.

The function $G^*(K, \theta)$ is obtained by multiplying $G(k, \theta)$ by the ramp filter $|k|$:

$$G^*(K, \theta) = G(k, \theta) \cdot |k| \quad (3.16)$$

The function $G^*(r, \theta)$ is the inverse Fourier Transform '1D FT' with respect to K of $G^*(K, \theta)$:

$$G^*(r, \theta) = \int_{-\infty}^{\infty} G^*(K, \theta) e^{i2\pi kr} dk \quad (3.17)$$

So the function $f(x, y)$ can be reconstructed by back-projecting $G^*(r, \theta)$:

$$f(x, y) = \int_0^\pi G^*(r, \theta) d\theta \quad (3.18)$$

Usually, the ramp filter has the effect of filtering out low frequencies and passing high frequencies with a linear behavior in between. Thus, with this filter contrasting features (high frequencies) are accentuated, while blurring (low frequencies) is minimized. It works well for reconstructing projections but it has an undesirable effect which is sensitivity to noise that is in the projections. For this reason other filters are preferable. Thus, the ramp filter is multiplied by a window that de-emphasizes the high frequencies. Most of these filters are described in section 5.3.

Thus, using direct Fourier or FBP reconstruction algorithms, multiples routes are employed to reach the final image as shown in figure 3.11 and 3.12 [21][27].

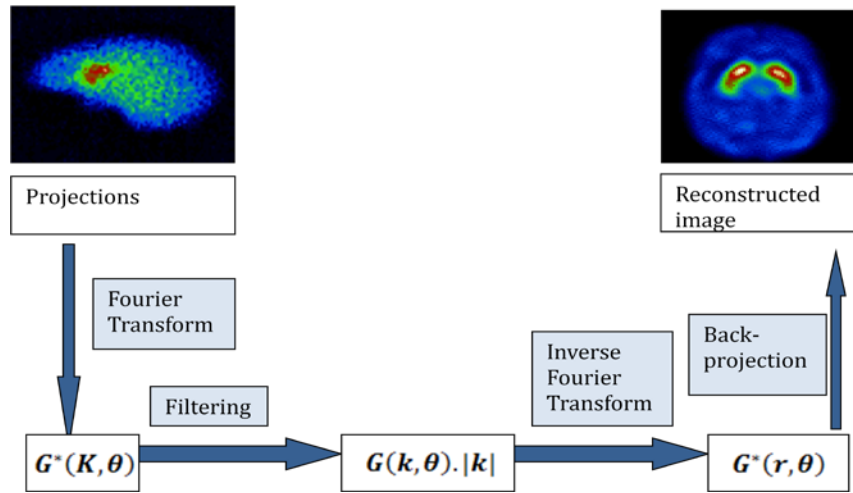


Figure 3.11: Filtered- back projection [11].

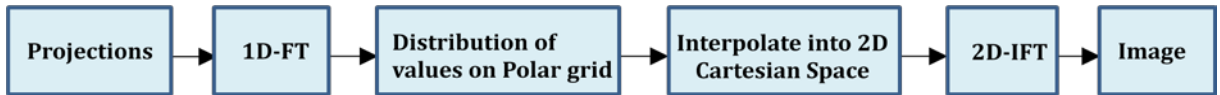


Figure 3.12: Fourier transform algorithm.

3.5 Emission tomography

Iterative-reconstruction algorithms are the most popular in emission tomography for the following reasons:

- The projection noise is easier to be modeled and handled, especially when the detector counts are low;
- The imaging physics, such as geometry, non-uniform attenuation, scatter, etc, are easier to be modeled.

The process of iterative reconstruction is based on image discretization into pixels (see figure 3.13). Then, each pixel value is treated as an unknown. According to the imaging geometry and physics, a system of linear equations can be set-up. An iterative algorithm is finally implemented to solve the system of equations. The setup of equations is illustrated in figure 3.13.

In the following discrete model, f_j is the object distribution given a set of projections measurements g_i . A_{ij} represents information about the imaging system that produced the measurements, and, possibly, a statistical description of the data and of the object.

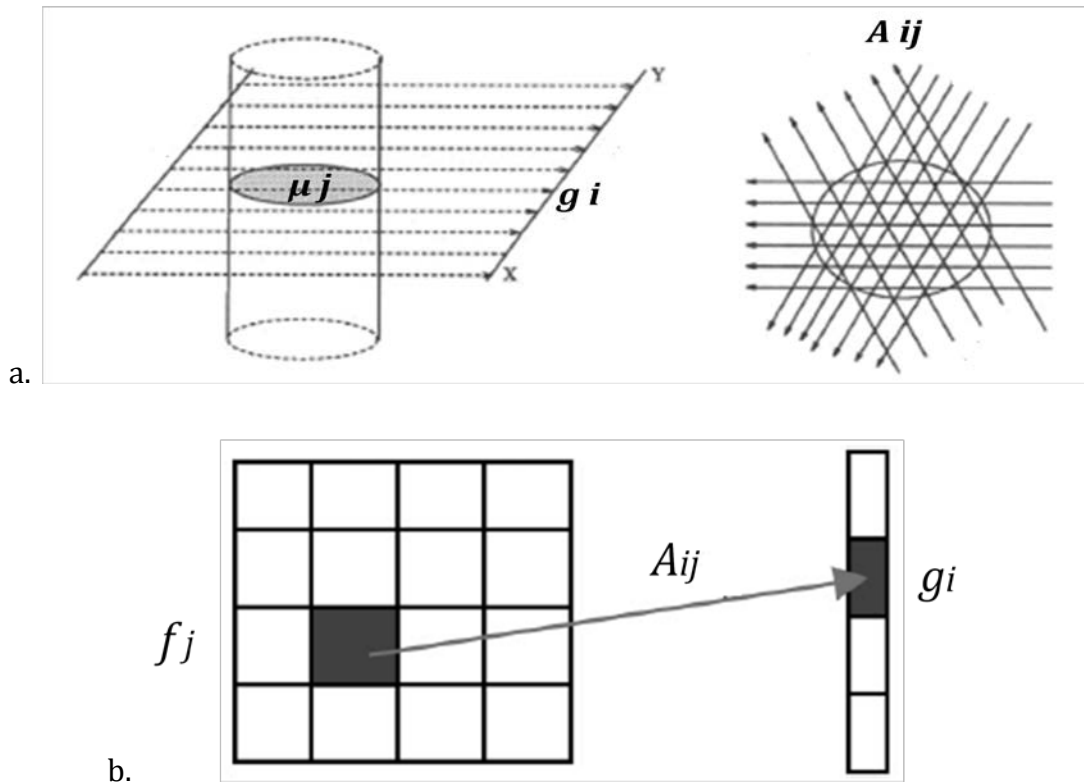


Figure 3.13: A discrete model of the projection process in (a) 'Transmission Tomography' [30]; (b) 'Emission Tomography' [31].

In emission tomography, the system of linear equations can be represented in the matrix form as $g = Af$, where each element (f_j) in f is a pixel value, each element (g_i)

in g is a projection measurement, and A_{ij} in A is a coefficient that is the contribution from pixel j to the projection bin i .

The diagram in figure 3.14 shows the basic procedure for using an iterative algorithm. Each loop in the chart represents a single iteration. Starting from an initial guess, the image is updated iteratively so that its projections through A match better the measured projections.

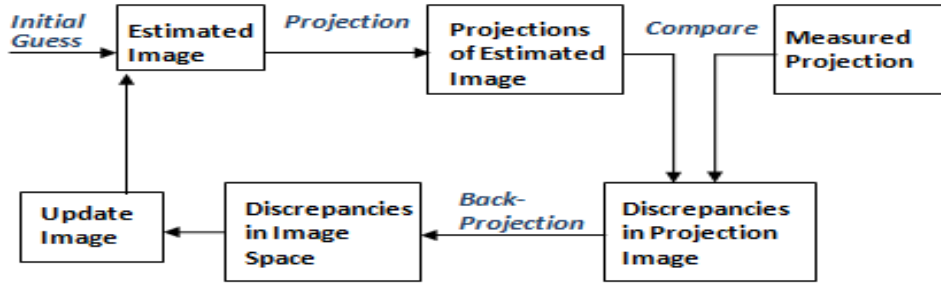


Figure 3.14: Flow chart of an iterative image reconstruction scheme [31].

In most cases, projection data contain noise. What happens during the progress of the iterative procedure is that the reconstruction simulation converges to a recognizable image and then “diverges” to noise. For this reason, noise regularization is an important factor in an iterative algorithm. For instance, stopping the iteration at a certain point is a simple regularization method [31] [32].

3.5.1 Algebraic Reconstruction Technique

Assuming that the cross section of a sample is an array of unknowns; establishing algebraic equations for the unknowns referring to the measured projection data is an entirely different approach for tomographic imaging. This algebraic reconstruction technique (ART) is an iterative procedure. In the iterative technique there are two approaches for reconstructing the image.

In the first approach, the projections of an initial estimate are taken and compared with measured projections. This is done instead of back-projecting the average ray value. After that, the comparison result is used to modify the current estimate. Therefore, the goal is to push the new estimate closer to the true solution. In the second approach, a set of simultaneous equations represents the reconstruction problem. The unknown cross-section image is considered as a 2-D matrix. Within each cell of the matrix, the image values are assumed to be constant. Then for each ray, a set of linear equations is formed as:

$$\sum_{j=1}^N A_{ij} f_j = g_i \quad (3.19)$$

where $i = 1, 2 \dots N$

The i^{th} numbers represent the projections rays and g_i are the projection data along these rays. A_{ij} is the function area of j image cell intercepted by i^{th} ray. The values of the matrix elements which are the pixels are represented by f_j . The total number of rays in all projections is M and the number of grid cells is N .

When M and N are large values, a specific iterative method is needed to solve equation 3.19. One of the famous existing methods is the Kaczmarz method. It is a one iteration step method elaborated from the work of the Polish mathematician Stefan Kaczmarz. It is a known method in numerical linear algebra that solves linear systems of equations $Af = g$. From the projections, this method is rediscovered and used in the field of image reconstruction where it is called the Algebraic Reconstruction Technique (ART). The approximation solution of the linear system of equation is computed as in the following formula:

$$f_j^{(i)} = f_j^{(i-1)} + \lambda \cdot \frac{g_{k-} \overrightarrow{A_K f^{i-1}}}{\sum_{i=1}^N A_{kj}^2} \cdot A_{kj} \quad (3.20)$$

where $f_j^{(i)}$ is the new pixel value. Apparently, it is considered the correction factor for the i^{th} ray that updates the j^{th} pixel on every ray equation. $f_j^{(i-1)}$ is the former pixel value. λ is the relaxation parameter, $\sum_{i=1}^N A_{kj}^2$ is applied to normalize the difference and A_{kj} is a “weight” for the correction [27]. This equation is used to project a point onto a hyperplane.

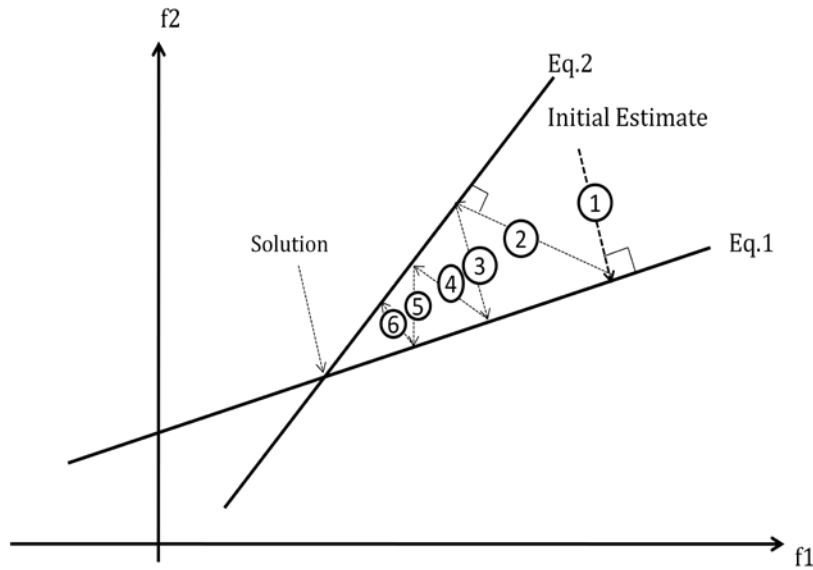


Figure 3.15: The Kaczmarz procedure with 2 measurements [32].

In the Kaczmarz method, each linear equation in the imaging model defines a hyper plane in the vector space. Therefore, the solution is any point that lies in the

intersection of all hyper planes. An example of this procedure and of Kaczmarz situations are illustrated in figure 3.15. In order to find the solution point, an initial estimate is taken. From this point, perpendicular projections are taken successively onto each line or hyper plane. Each step is preceded by finding the closest point to the current estimate.

Due to the noise resulted from the ART technique, two different algebraic reconstruction algorithms were introduced as an improvement of the ART. The SIRT, “Simultaneous Iterative Reconstruction Technique” and the SART, “Simultaneous Algebraic Reconstruction Technique.”

The simple principle algorithm of ART is that the densities spread over the reconstruction space are modified after each iteration. The drawback of this method is that during one iteration, a pixel may be crossed by many rays and this will lead to noise and to a stripped result image.

In order to solve this problem, a technique called simultaneous iterative reconstruction technique (SIRT) is established. In the SIRT, the pixel is updated after going through all the equations and not after only one ray. Thereby, the change on each pixel is an average value of all the computed changes of this specific cell.

However, the SIRT has not gain much popularity due to the long time for convergence and hence for generating the image. Therefore, another technique called the SART, simultaneous algebraic reconstruction technique, is developed. The computational advantage of SART is that the update of pixels is done at a certain angle after a computation of the whole projection image. In this way, a single iteration can reconstruct a fairly good image.

The Algebraic Reconstruction Technique (ART) is a class of iterative algorithms for the reconstruction of an image from a series of angular projections (the sinogram). In the following sections, other algorithms and optimization methods like the CG Conjugate Gradient Algorithm, MLEM Maximum Likelihood Expectation Maximization Algorithm, MAP Maximum A Posteriori Algorithm, are discussed.

3.5.2 Gradient and Conjugate Gradient Algorithm

The gradient or the conjugate gradient algorithm is also named the steepest-descent algorithm. Its target is to avoid lengthy and tedious process of image reconstruction. Therefore, instead of that, the projections of each image are computed and then these projections are compared to the measured projections. This difference is estimated and plotted. As shown in figure 3.16, the plot is like a mountainous terrain. The plot dimensions number is equal to the number of pixels in the image. It is clear that the minimal difference is at the point of the lowest altitude. By finding the location of

that point, the solution is reached. This is because the coordinates of that point are the pixel values of the solution image.

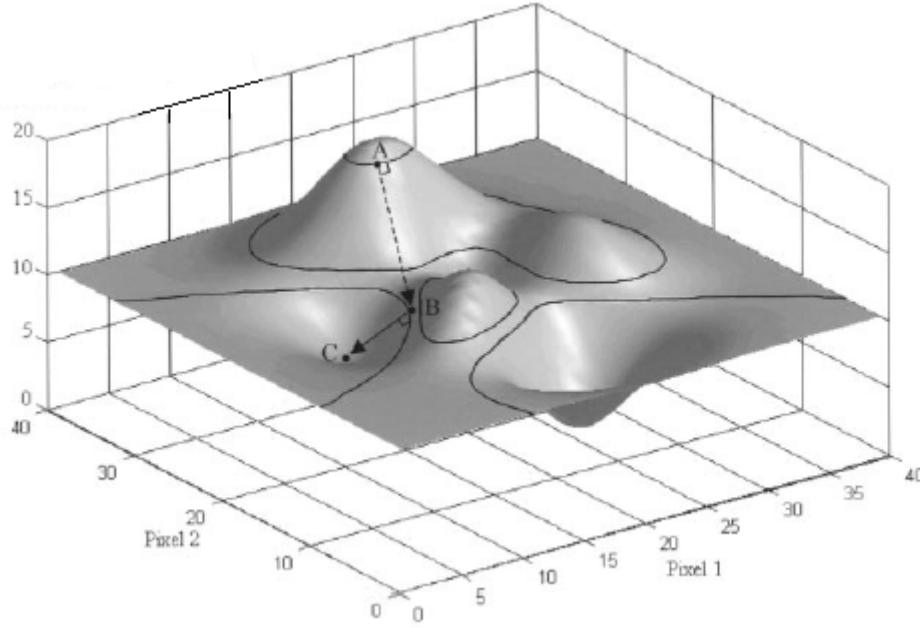


Figure 3.16: Gradient Algorithm: Difference between estimated and measured projections [26].

The process of “steepest descent step” is illustrated by the dashed and the solid arrow shown in figure 3.16. More specifically, starting from an initial estimate (like point A in figure 3.16), we jump to a lower altitude point. The points of same altitude have one common contour, so the process of descent steps is repeated until the lowest altitude is reached. Location C in the figure gives solution for the 2 pixels image. In order to get minimal number of steps, the direction and the length of the steps are optimized by curving the gradient lines perpendicular to the contours. Mathematically, searching for the solution is upon:

$$f^{(k+1)} = f^{(k)} + \alpha^{(k)}p^{(k)} \quad (3.21)$$

This equation is an iterative algorithm in which $f^{(k+1)}$ is equal to the previous estimate $f^{(k)}$ plus a vector $p^{(k)}$. The vector indicates the new chosen direction that must be opposite to the local gradient and in this way directed toward the steepest descent. The step length is represented by the weight $\alpha^{(k)}$. This coefficient is chosen to optimize the convergence of the process.

Theoretically, the number of equations of the system, in this example the number of pixels, is equal to the number of iterations needed for the conjugate gradient algorithm to converge. Actually, it is applied to $g = Af$ but the determination of the conjugate directions leads to errors before reaching the solution in a specified number of iterations. Therefore, this method is not absolutely efficient [26].

3.5.3 Maximum Likelihood Expectation Maximization (MLEM) Algorithm

The name Maximum Likelihood Expectation Maximization refers to the fact that there is an expectation step that uses current estimates of the unknowns to perform the reconstruction, followed by a maximum likelihood step to update the estimates. The popularity of MLEM is due to the high degree of accuracy in the compensation of non-uniform attenuation.

In the case of Emission Tomography, which is relevant to our project, the emitted and the detected photons are assumed to be Poisson random variables, a statistical criterion is needed. This is in the case of MLEM where the noise is also modeled as Poisson. Hence, in the statistical reconstruction algorithms, the emission data is modeled first and then an estimate of the source distribution is derived. Accordingly, the statistical criterion is to determine the source distribution that most likely gave the emission data using the expectation-maximization (EM) algorithm.

The vector “ f ” that is a solution for “ $g = A f$ ” using MLEM is derived as follows. The Poissonian probability of detecting “ g ” photons emitted from the pixel j by bin i is:

$$P(g_i) = \frac{e^{-\bar{g}_i} \bar{g}_i^{g_i}}{g_i!} \quad (3.22)$$

The conditional probability $P(g/\bar{f})$ of observing the vector g when the emission map is \bar{f} is the product of the individual probabilities $P(g_i)$. Then the highest value for the likelihood $L(\bar{f}) = P(g/\bar{f})$ is found by computing its derivative. By applying the natural logarithm to the previous result, we can maximize the expectation. This leads to the following iterative scheme:

$$f_i^{k+1} = \frac{f_j^k}{\sum_{i=1}^N A_{ij}} \sum_{j=1}^{Det} \frac{A_{ij} g_i}{\sum_{i=1}^M A_{ij'} f_{j'}^k} \quad (3.23)$$

where f_i^{k+1} is the value of pixel i in iteration k ;
 A_{ij} , represents the elements of matrix A ;
 $f_{j'}$ is the probability that bin i detects a photon emitted from pixel j ;
 $A_{ij'} f_{j'}^k$ is the mean number of photons emitted from pixel j' and detected by bin i ;
as for $\sum_{i=1}^M A_{ij'} f_{j'}^k$, the mean number of photons g_i detected by bin i is the sum of the mean number of photons emitted from each pixel;
 N, M are the numbers of rows and columns, respectively.

So, for each iteration k , a current estimate f_j^k of the image is available. Thus, the algorithm is divided into 2 steps: the expectation step (E-step), and the maximization step (M-step). In the E-step we simulate what projections of this current estimate should look like. In the M-step the measured projections of this current estimate are then compared with the simulated projections. So, the denominator of the right side represents projections by summing the current estimate of the mean number of counts,

and the numerator represents the measured number of counts. The target is to produce an accurate estimate. The process is that in each iteration k the ratio between these simulated and measured projections is updated and it becomes iteration $k+1$. This will be repeated many times until an image with the greatest likelihood is found.

As shown in figure 3.17, each iteration requires one forward projection and one back-projection, so it needs more processing time than the FBP, thus it converges slowly and may require 50-200 iterations. In order to accelerate the reconstruction process using MLEM, the ordered-subsets expectation maximization (OSEM) has been proposed by Hudson and Larkin [26][33].

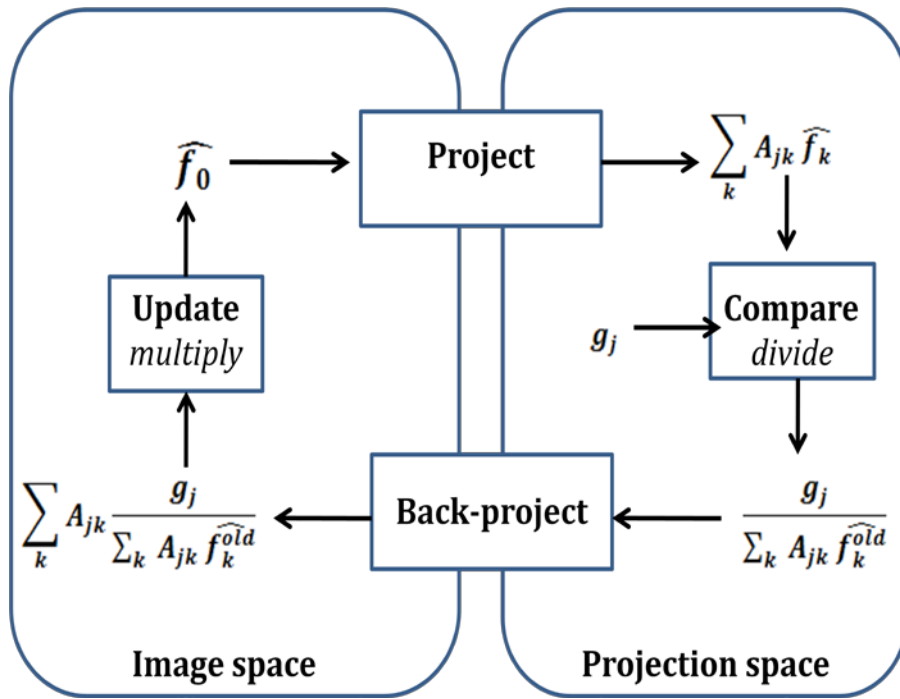


Figure 3.17: MLEM in the form of the general iterative model [32].

3.5.4 Ordered-Subsets Expectation Maximization (OSEM) Algorithm

The OSEM is a statistical method that yields accurate images for the following reasons:

- 1- In the Maximum Likelihood “ML” problems, the OSEM has a higher order-of-magnitude acceleration than the MLEM.
- 2- The reconstructed images are well defined after completing only a few iterations.
- 3- The implementation of OSEM is based on slight modification of the well-known and well-established EM algorithm.
- 4- The OSEM can be applied to any algorithm that updates its parameters simultaneously [34].

In the OSEM method, the set of projections is separated into subsets called also blocks, as illustrated in figure 3.18. The projections of each subset are equally

distributed around the sample. By updating the estimate of the source distribution, using only the projections within a given subset, the OSEM converges quickly toward the solution. For example, if there were 64 projections (acquired at 64 angles around the sample), they might be divided as into 16 subsets as follows, each containing 4 images:

Subset 1: Projections 1, 17, 33, 49

Subset 2: Projections 2, 18, 34, 50

.

.

.

Subset 16: Projections 16, 32, 48, 64

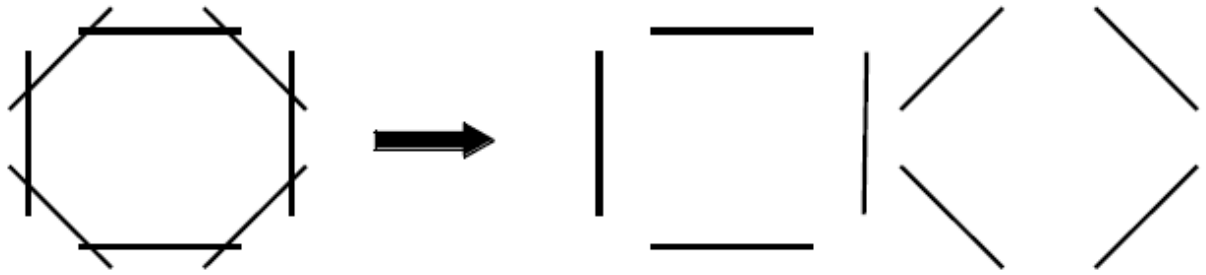


Figure 3.18: OSEM representing 8 projections divided into 2 subsets each one consists of 4 projections [33].

Then, the MLEM, previously described, is applied on each subset separately. This process is considered as a sub-iteration. When all subsets (16 subsets) are treated, the first full iteration is completed. Thus the convergence is accelerated [27] [32][35].

3.5.5 Maximum A Posteriori (MAP) Algorithm

In the MLEM algorithm there is a compromise between the number of iterations and image noise. The criterion of MLEM stating that “The estimated projections have to be as close as possible to the measured projections” does not lead to high-quality images. Noisy or blurred images are obtained while increasing the number of iterations. That’s why this criterion must be considered simultaneously with another one stating that “The reconstructed images have to be not too noisy”. Actually, the solution is the regularization or what we call the penalization of the noise. It is based on a prior image that gives an assumption or knowledge of what the true image is. This is known as a constraint that may favor convergence of the EM process. The aim is to find “ \bar{f} ” which must be a smooth and well defined image. This convergence is done when the prior and the two criterions listed above are maximized. Using Bayes’ theorem the prior knowledge is implemented in the EM algorithm. It is the conditional probability to have \bar{f} when the projections estimate g . It states that:

$$P(\bar{f}/g) = \frac{P(g/\bar{f}) P(\bar{f})}{P(g)} \quad (3.24)$$

where $P(g/\bar{f})$ as defined in the MLEM, it is the likelihood function;

$P(\bar{f})$ is the prior function, it expresses a prior knowledge of the reconstructed image;
 $P(g)$ defines a priori probability distribution of the measurements;
 $P(\bar{f}/g)$ defines a posteriori probability distribution of the image.

The logarithm of both sides of this equation is taken, and then we add the common Bayesian prior to enforce smoothness which is the Gibbs prior. Consequently, the maximization using Gibbs prior leads to an iterative scheme called the one-step-late (OSL) algorithm, described by Green:

$$f_j^{(k+1)} = \frac{f_j^k}{\sum_{i=1}^N A_{ij} + \beta \frac{\partial}{\partial f_j} U(f_j^k)} \sum_{j=1}^{Det} \frac{A_{ij} g_j}{\sum_{i=1}^N A_{ij} f_i^k} \quad (3.25)$$

where $\frac{\partial}{\partial f_j} U(f_j^k)$ is the prior term; it consists of U . For instance, U could be an energy function that enforces the smoothing and β a factor that modulates the importance of the prior. β is also called the weight of the prior, multiplied by the derivative of U , it constitutes the modification in the EM algorithm. This new approach leads to the MAPEM algorithm: “Maximum A Priori Expectation Maximization Algorithm” [26] [37].

3.6 Conclusion

In general, the iterative techniques can incorporate the physical factors more accurately than the analytical techniques. In addition, the efficiency of MLEM and MAP has already been proved in reducing image artifacts and beam hardening. Our interest for the fluorescent data is to get an image with a high spatial resolution and at the same time in an acceptable convergence time. Due to the statistical nature of the fluorescence emission and acquisition, an optimization phase is processed first and then a combined reconstruction algorithm is developed and implemented.

Chapter 4 Simulation & validation

method

4.1 Introduction

In this chapter, a simulation code of X-ray fluorescence tomography developed for this thesis is presented in details. The aim of the simulation code is to determine the technical parameters of the measurement system in order to perform the data optimization phase and apply an image reconstruction technique. This simulation is not only restricted on identifying the sample. In fact, the physical phenomenon of X-ray interaction with matter, in addition to many geometrical and statistical factors are considered and established. These simulations are realized using the “Visual C++” and the “MATLAB” as programming languages along with specific 3-D triangle-mesh modeling editor. The simulation code has been created from scratch; the chart of the code is represented in Annex B. Previous works on X-ray imaging simulation codes implemented either ‘Monte Carlo’ or ‘Ray Tracing’ technique.

Monte Carlo method is a probabilistic technique. Its main idea is to find a solution for a mathematical problem by performing statistical sampling experiments. The process involves the estimation of a parameter of a true or hypothetical distribution. This parameter will be the answer of the problem and it is approximated by performing many repetitive simulations using random numbers and probability. For this reason it is a statistical simulation method. It is also a precise technique and is considered the closest simulation to real life situation [38]. As illustrated in figure 4.1 (a) the Monte Carlo technique takes into consideration random interactions of particles and scattering photons. Although Monte Carlo is very realistic, it produces noise and requires long-time and powerful computers to perform calculations.

Whereas ray tracing technique, simulates a set of rays from a light source to a detector and reproduces the path followed by this beam (see figure 4.1 (b)). An amount of computation is needed to express how each ray intersects and interacts within an

object in its way. Although ray tracings a deterministic and predictable process, it does not simulate the diffusion process. Usually, ray tracing technique is simple to be implemented in software codes and can be considered an alternative to Monte Carlo. On the other hand, ray tracing technique is faster. Even when we have complex samples and in need for multiple interactions, ray tracing technique has proved effectiveness [39][40].

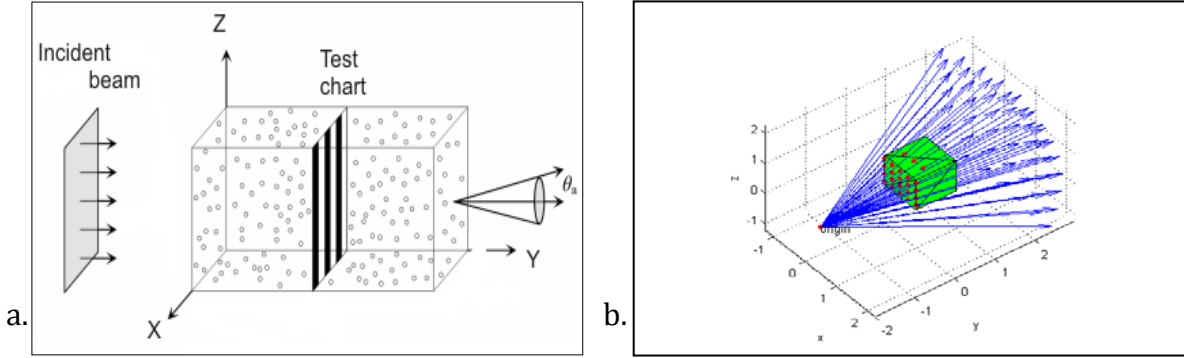


Figure 4.1: (a) Monte Carlo technique [38]; (b) Ray Tracing technique.

4.2 Set-up modeling

In order to simulate an experimental situation representing either a transmission tomography or a fluorescence tomography, various input data and several databases are required. The input parameters that are the geometrical characteristics, the settings for the source, the sample, the collimator and the detector can be defined and specified. The simulation code applies these input parameters during implementation. Then by adjusting these input parameters the optimization phase is executed.

Besides the definition of tools, the physical phenomenon of X-ray interaction with matter and the data collection are implemented with maximum accuracy. Our simulation software is then dedicated to perform the image reconstruction technique. The simulation code was developed to work as per the methodology presented in figure 4.2.

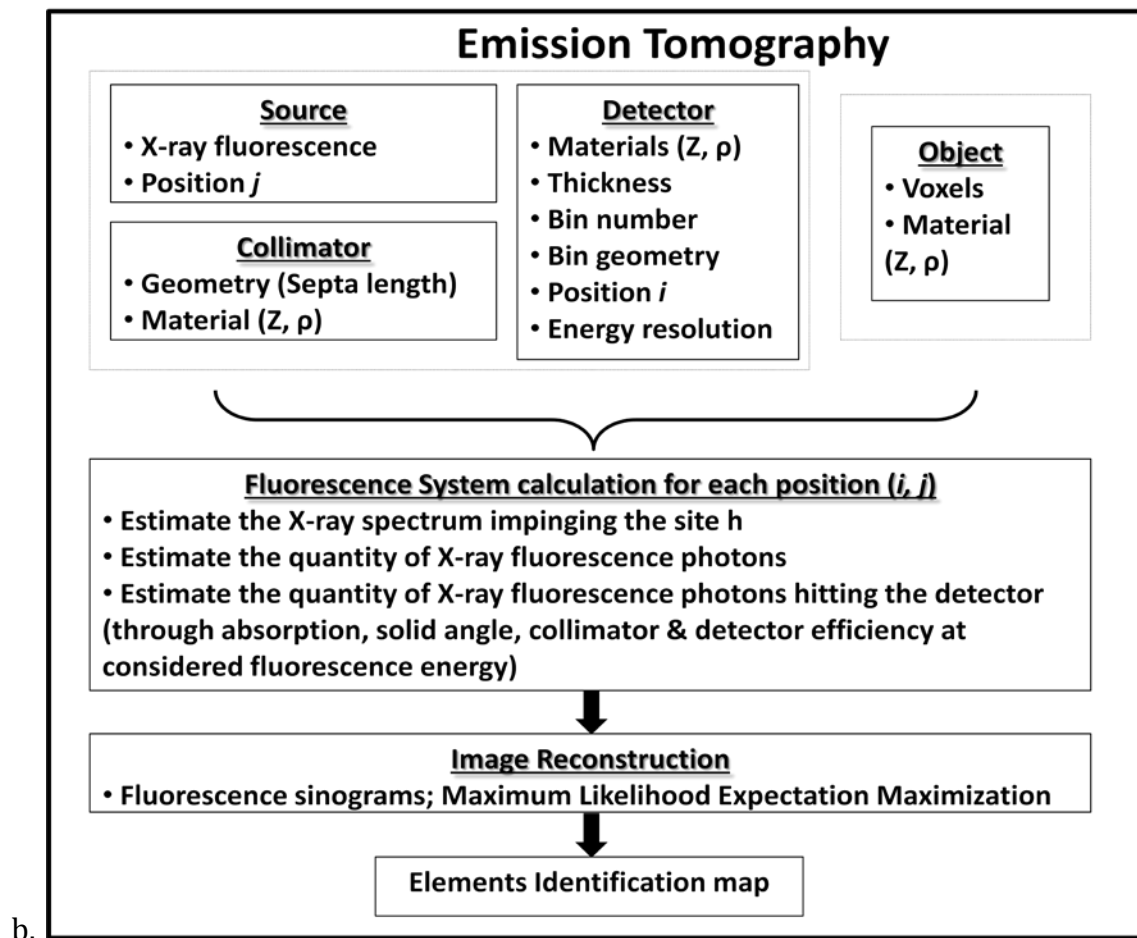
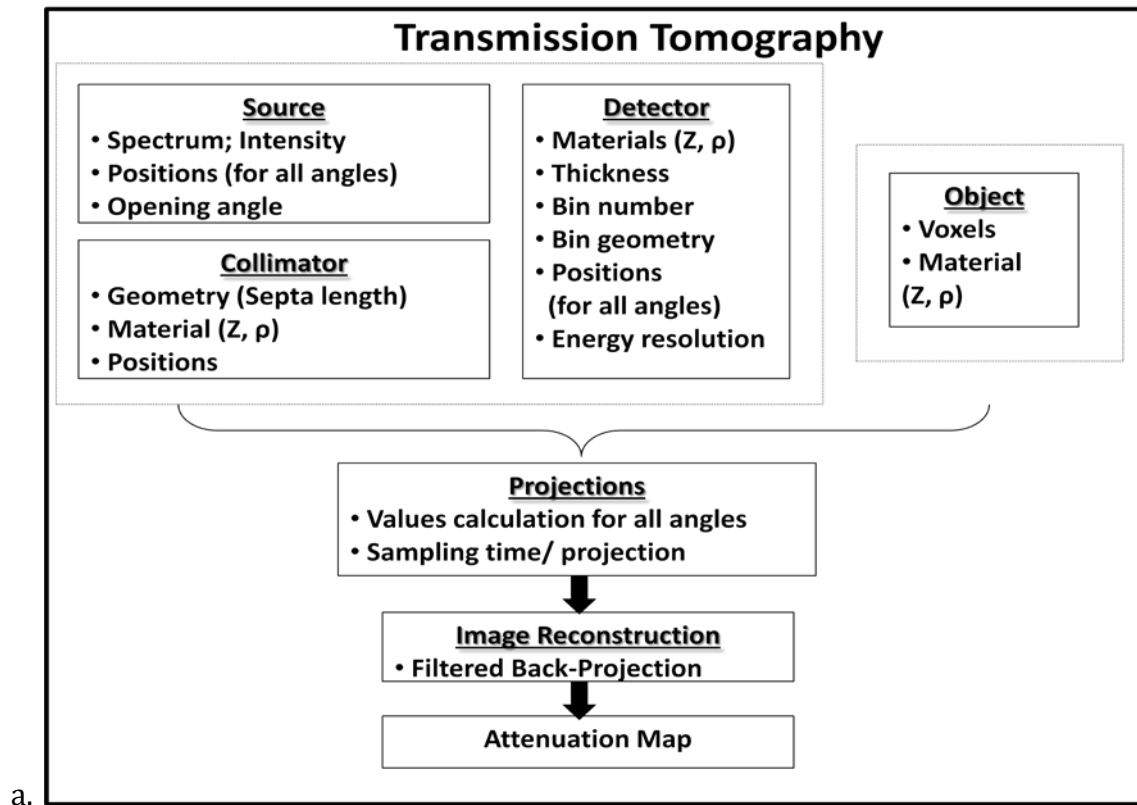


Figure 4.2: (a) CT transmission modeling chart; (b) ET fluorescence modeling chart.

It is designed such that it starts by reading a data file containing the technical parameters of all the imaging components: source, sample, collimator and detector. The data entry file is shown in figure 4.3.

```
source-object-detector specs:

OBJECTSPECS: d:\\Code\\VoxSpecs.txt
object_direction1: 0.0 -1.0 0.0
object_direction2: 0.0 0.0 1.0
object_direction3: 0.0 0.0 -1.0

COLLIMATOR SPECS:

Collimator: d:\\Code\\VoxSpecs_COL.txt

SOURCESPECS:

source_filename: d:\\Code\\Source400160.txt
working_tension: 120.0
source_direction: 0.0 1.0 0.0
Source_Position: 0.0 15.0 -15.0
working_current: 1.0

DETECTOR SPECS:

Detector_Shape: Cube
Rotation_Angle_det: 3.14
Cylinder_Radius_det: 3.0
Base_det: 2
Height_det: 6.0
Cube_Name_det: d:\\Code\\Cubefordet.stl
Det_Direction: 0.0 -1.0 0.0
Det_Position: 0.0 -9.0 -2.5
Det_Pos_sc: 0.0 0.0 0.0
Lenght_det: 1.0
Thickness_det: 1.0
width_det: 5.0
```

Figure 4.3: Data entry file.

4.3 Source definition: Polychromatic source loading

Many important variables determine the effectiveness of an X-ray source such as the X-ray intensity, the generated spectrum of energies and the size of focal spot. As our system simulation adopts the ray tracing technique, the focal spot is determined by the followed line paths. The used polychromatic X-ray source is shown in figure 4.4. For each output source voltage (ranging between 25 kV to 160 kV), a spectrum is displayed over 53 different energies. The spectrum loading consists of associating the values at all energies with a specific working tension.

Usually, the X-ray tube anode type, maximum voltage and maximum current are selected according to the sample that is analyzed and according to a particular task such as having fluorescence emission.

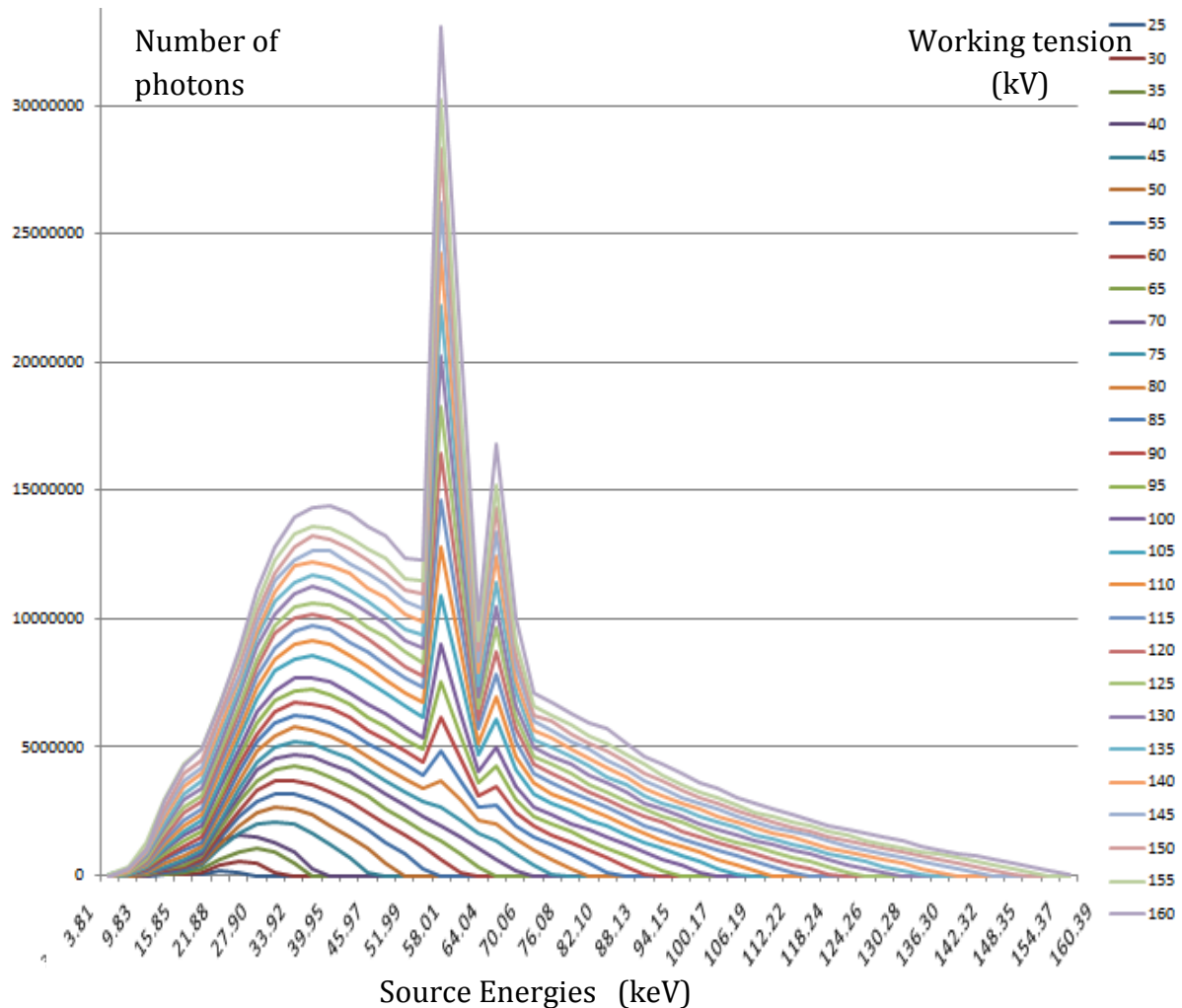


Figure 4.4: A polychromatic X-ray source spectrum representing the number of photons at different working tensions (data file brought from LIST laboratory; CEA-Saclay).

4.4 Object description: Stereo-Lithography (StL) format

It is divided into 3 steps; sample creation, database file saving for each voxel of the sample and implementation.

The utility of the StL format is that a variety of geometrical shapes and dimensions can be created. They can be assigned as sample objects or as detectors. In this project, a disc, a cylinder, a sphere and a cube (seen in figure 4.5) are simulated by defining the number of facets, the radius, the center position and the height and by applying the geometrical equation to each shape.

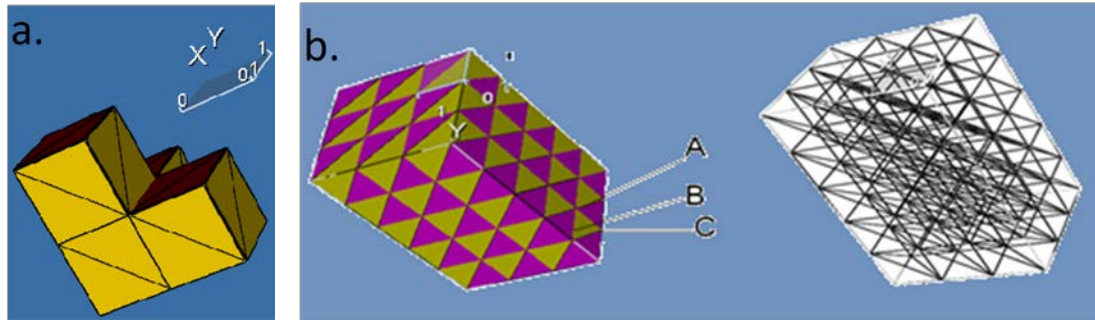


Figure 4.5: (a) Adjacent voxels of 12 facets each. (b) Cube of (x=3; y=3; z=5) dimension.

The “Stereo-Lithography” format or the StL format represents an object by a 3-dimensional surface geometry. The surface is a series of small triangles (facets). Each facet is described by 3 points representing the vertices (corners) of the triangle and a normal, which is a perpendicular direction. As shown in figure 4.6, the normal determines the orientation of the facet in the space. Moreover, the order of the vertices must be defined to precise if the normal is inward or outward.

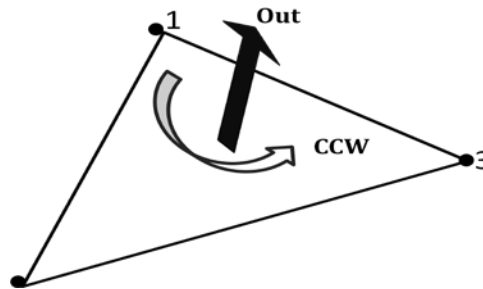


Figure 4.6: The facet orientation defined by the right-hand-rule or the counter clock wise orientation.

During creation of a StL object, some building parameters must be considered. The sorting of the facets is completed such as each triangle shares 2 vertices with its adjacent triangle. In addition, by defining the length of the triangle side, the size of the whole objects is determined. The StL format syntax is described in Annex C.

Other than the dimension, the pre-defined values can assign the resolution. For example, in the case of a cube that is an arrangement of voxels. By varying the length of the facet sides, the voxels resolution is modified (see figure 4.7).

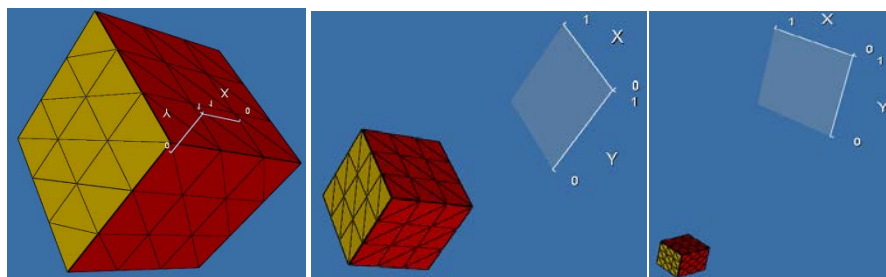


Figure 4.7: An StL cube with resolution 1; 0.3; 0.1 consecutively.

In this project, the sample, the detector and the collimator used for the X-ray fluorescence tomography are created in the StL format. This is illustrated in figure 4.8.

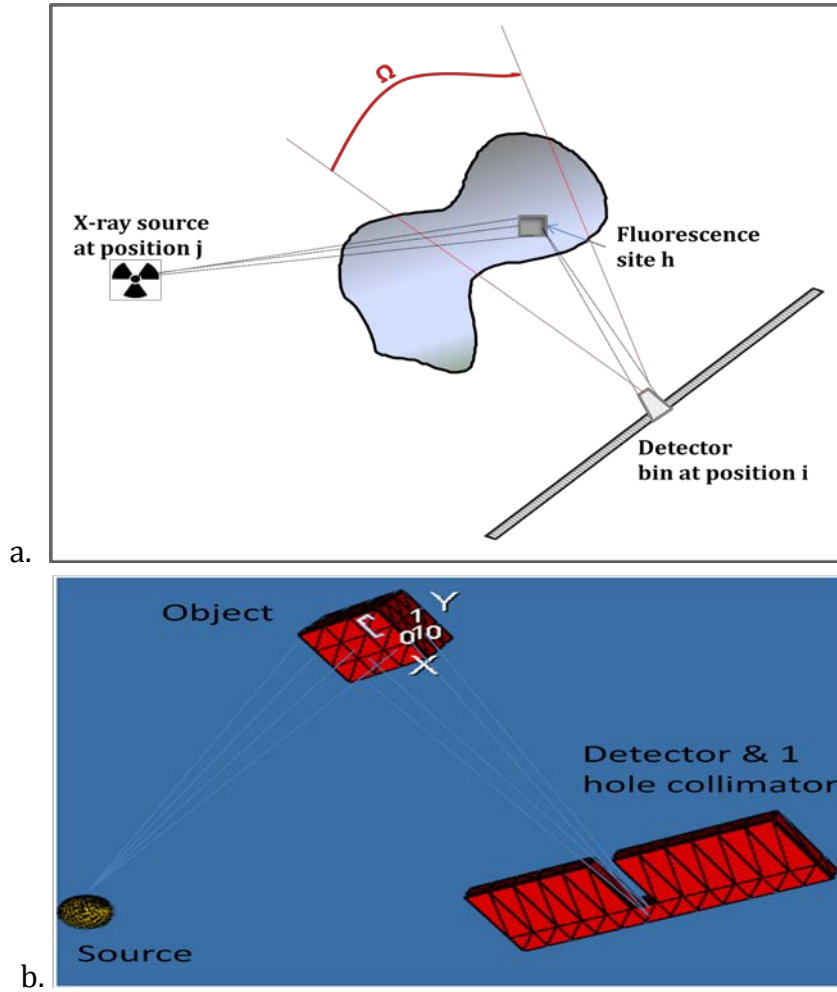


Figure 4.8: (a) Fluorescence emission illustration; (b) Simulation of source-object-collimator-detector.

The implementation of cube creation is as shown in figure 4.9. Referring to the code methodology (figure 4.9 (a)) the sample is created (in the StL format as described in the above matrix). In addition, from the data entry file, the object database file is designated. Upon the chosen geometrical shapes, the data of each voxel is simulated in a separate database file. Then, each voxel is defined by a type (Germanium, Titanium, Lead, etc...) and is processed alone.

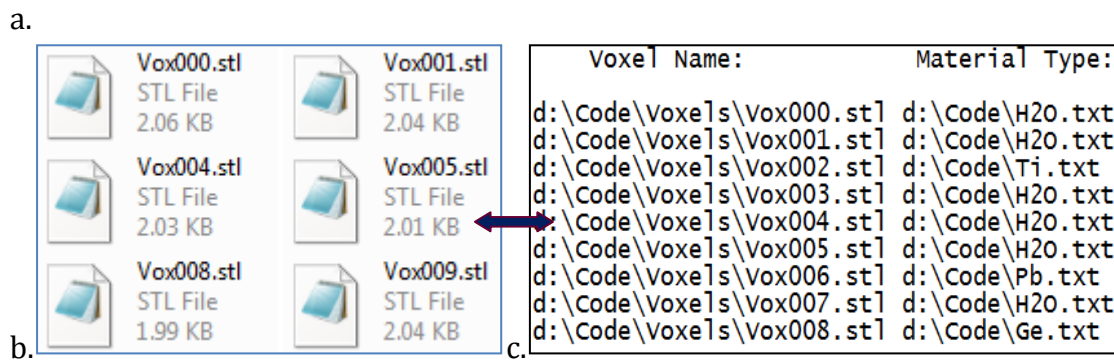
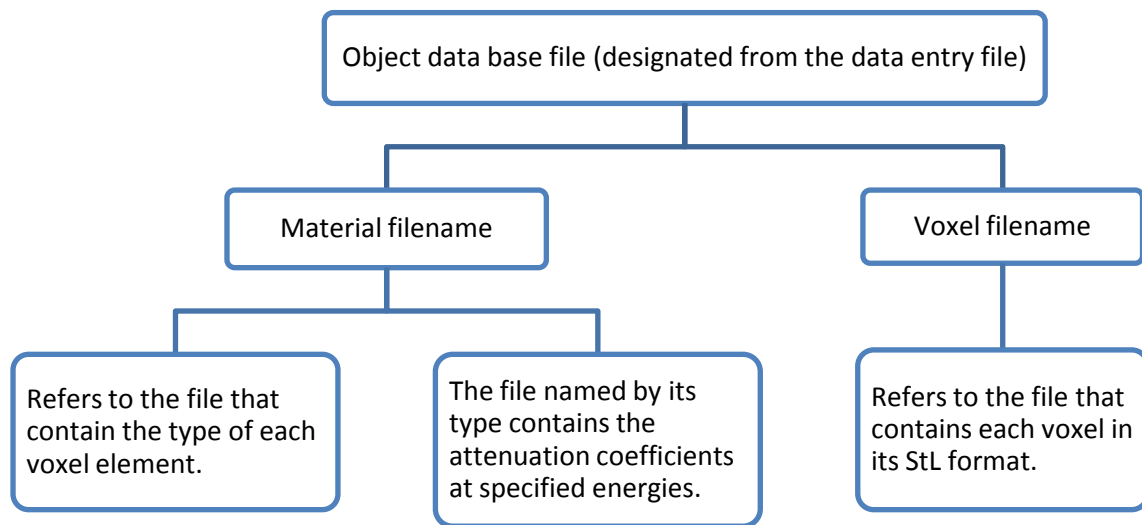


Figure 4.9: (a) Sample preparation and implementation; (b) Voxel filename; (c) Material filename.

4.5 Collimator and detector modeling

The first reason for the detector to be collimated is to avoid scattered photons. Thereby, to focus the emitted rays on the detector, a 1 hole-collimator or a multi-hole collimator is used. After defining the shape of the detector and the collimator, various parameters are taken into account. First, we specify the position and the orientation in space, which is the direction. Regarding the resolution, it is defined during the creation of the detector or the collimator. In our experiment, they are represented by cubical pixels hence the spatial resolution is the size of the pixels (see figure 4.10).

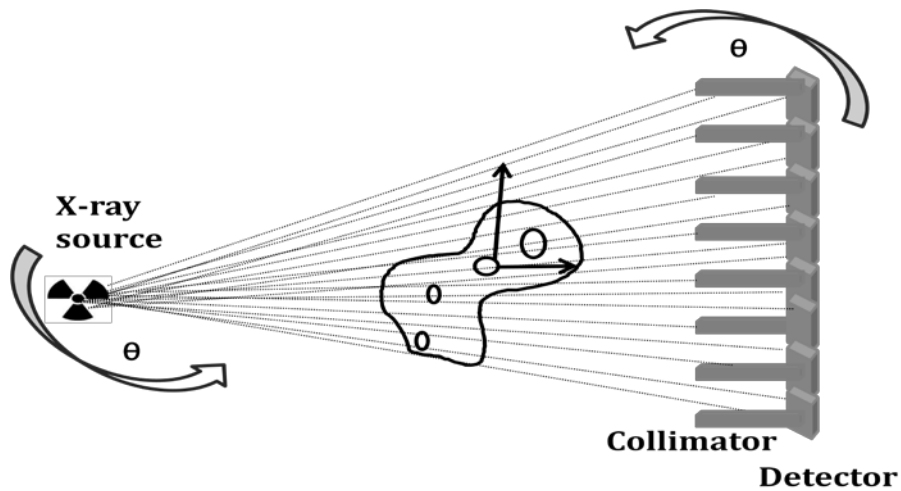


Figure 4.10: Detector-collimator modeling.

Upon the simulation code methodology, the simulation of the collimator requires the following steps:

- From the data entry file, the collimator database file is assigned.
- Upon the chosen geometrical shape where the length of the collimator septa is determined (see figure 4.11), the data of each voxel is simulated in a separate database file.
- Upon the chosen collimation (i.e. number of holes), each voxel of the collimator is defined either by a “Lead” type or by a “Hole” type.

Data acquisition through collimator is done as follows:

- The type of each collimator voxel is checked individually;
- If the voxel is Lead (Pb) the loop will continue checking the voxel type;
- If the voxel is hole, the intersection process is carried on.

In this way, the collimator forms the image by selecting only the rays traveling in a specific direction, namely the direction in which the hole is oriented.

Similarly, the simulation of the detector (shown in figure 4.10) requires the following steps:

- From the data entry file the detector shape is specified. It can be cubical or cylindrical.
- This shape is created depending on the parameters listed in the data entry file.
- In the ray tracing technique, the center of the detector pixel is simulated as the centroid (triangle center) of the facing facet.

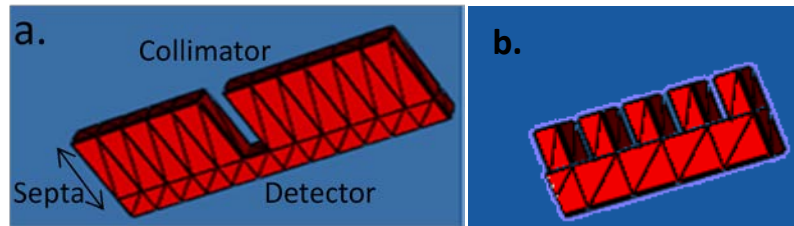


Figure 4.11: (a) Detector and a 1-hole collimator with long septa; (b) Detector and a multi-hole collimator with short septa.

4.6 Simulation process

After creating and defining the imaging tomography elements, the simulation code evaluates the intensity of each projection as stated in the following.

- The intensity reaching the voxel is estimated by:
 - Applying the line-facet intersection (described in Annex D) technique between Source-Sample.
 - Performing the attenuation correction for the area between source and sample (this is also noted as sample self-absorption).
- The intensity interacting within the voxel is evaluated by:
 - Computing the distance between 2 intersection points.
 - Extracting the attenuation coefficient of the corresponding voxel type.
- The intensity of emitted fluorescence is estimated by:
 - Evaluating the fluorescence quantitative analysis including all the probabilistic factors.
- The detected intensity (at the detector level after being collimated) is evaluated by:
 - Applying the line-facet intersection technique between Sample-Detector.
 - Performing the attenuation correction for the area between sample and detector (this is also noted as sample self-absorption).

As for the quantitative analysis of the fluorescence, it is described in section 4.8.

4.7 Attenuation correction

Based on the simulation code methodology, the attenuation phenomenon is corrected. Various attenuation factors must be considered for the attenuation correction between the Source-Object, Object-Object and Object-Detector. For the incident photons, the attenuation coefficients are extracted depending on source energies; whereas for the fluorescent photons, the fluorescence energies are computed then the attenuation coefficients are extracted based on these fluorescence energies.

Beam attenuation inside the sample is based on Beer's Lambert Law:

$$I_{(\lambda)} = I_{0(\lambda)} e^{\Sigma L(-\mu_{(\lambda)} x)} \quad (4.1)$$

where $I_{0(\lambda)}$ is the incident intensity at specific wavelength(s);

L is the scanning line or line of response;

$\mu_{(\lambda)}$ is the attenuation coefficient corresponding to the source wavelength or fluorescence wavelength;

x is the distance traveled by the incident beam inside the sample.

Beer's Lambert equation shows that the attenuation coefficient is specific for each energy or wavelength of the incident ray. This linear attenuation coefficient has as unit [cm^{-1}] and it depends also on the atomic number of the absorber. For this reason, in the fluorescence tomography, the X-ray source energy and the fluorescence energy are associated with the mass attenuation coefficient for every element type. In this way, corrections for absorption are done before and after the fluorescence point.

Cross-sectional attenuation coefficient extraction:

Once the energy is specified, the attenuation coefficient is loaded. In the case of fluorescence energies, an interpolation is needed in order to get an accurate attenuation coefficient value. From the object database file, the designated type of material (Germanium, Lead, etc) refers to a corresponding data file that contains energies with their attenuation coefficient. One example of this file is shown in figure 4.12 (b). During the process for the same atom or material type, the attenuation coefficients are taken from 2 different files. One of them is referring to source energies and the other to fluorescence energies (figure 4.12 (a)).

a.	Voxel file name:	Source energies file:	Fluorescence energies file
	d:\Code\Voxels_Col\Vox005.stl	d:\Code\Pb.txt	d:\Code\Pb_shell.txt
	d:\Code\Voxels_Col\Vox006.stl	d:\Code\H2O.txt	d:\Code\H2O_shell.txt
	d:\Code\Voxels_Col\Vox007.stl	d:\Code\Ti.txt	d:\Code\Ti_shell.txt

Number of Energies: 53	
Energies (Kev)	Attenuation(cm-1)
3.808	15210.93
6.819	3839.97
9.831	1540.53
12.843	785.94
15.854	1519.63
18.866	1130.1
21.877	773.43
24.889	554.1

Figure 4.12: Energies and their corresponding attenuation coefficients (for Lead *Pb* element).

4.8 Simulated fluorescence quantitative analysis

The fluorescence quantitative analysis is established to relate the intensity of the emitted fluorescence to the concentration and distribution of the elements inside the sample [14]. The fluorescence and the number of photons are evaluated at the level of each voxel inside the sample as follows (see figure 4.13):

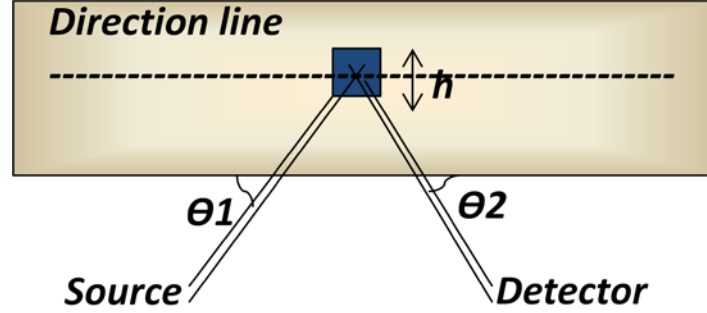


Figure 4.13: Interaction between source, voxel and detector showing the angles.

$$P_i = qE_i\rho hC_i \int_{\lambda_0}^{\lambda_{end}} \mu_{\lambda i} I_{\lambda} d\lambda \quad (4.2)$$

Where P_i is the fluorescence emitted from each voxel;

ρ is the sample element density;

h is the sample element size;

C_i is the sample element concentration;

q is a geometrical factor between source, sample and detector;

E_i is the fluorescence yield;

$\lambda_0 - \lambda_{end}$ is the wavelength spectrum.

$\int_{\lambda_0}^{\lambda_{end}} \mu_{\lambda i} I_{\lambda} d\lambda$, in equation 4.2, is the summation of the attenuation multiplied by the number of photons arrived and attenuated within each voxel.

Concerning q , as shown in figure 4.13, the angle between source and sample direction line is the incident angle θ_1 and the angle formed by the sample direction line and the detector is the take-off angle θ_2 . It is represented by:

$$q = \frac{\sin \theta_1}{\sin \theta_2} \quad (4.3)$$

I_{λ} is the incident intensity (number of photons) interacting inside the element. It is represented by:

$$I_{\lambda} = flux \times e^{\sum \mu_{\lambda i} x_1} \quad (4.4)$$

where: $flux$ is the incident flux from the X-ray source taking a specific tension at all energies;

$\mu_{\lambda i}$ is the element attenuation at a specific wavelength of the source;

x_1 is the intersection distance within each element in the sample taking the line between source and sample.

E_i is the fluorescence probability (yield). This probability gives efficiency to the fluorescence process because not all the ionizations induce an X-ray emission.

There are 2 methods for the fluorescence yield or the probability of fluorescence to be calculated. First by:

$$E_i = \frac{n_f}{n} \quad (4.5)$$

where n_f is the number of primary photons that have induced the ionization;

n is the number of secondary photons that are subsequently emitted [14].

Second, by the following equation that is used in our simulation code:

$$E_i = \frac{Z^4}{A_i + Z^4} \quad (4.6)$$

where i designates the shell involved;

A_i is approximately 10^6 for the K shell and 10^8 for the L shell;

Z is the atomic number.

As the atomic number increases, the fluorescence yield increases and for the elements with $Z > 78$ it is greater than 95 %. As seen in equation 4.6, the atom shell is designated. This is because for a given element, the fluorescence yield decreases from the K series to the L and M series [41]. In this simulation code the fluorescence at the K and L shell are implemented.

Concerning the number of photons reaching the detector, the function associated with the intensity of the X-rays interacting in the detector is:

$$I_{det} = P_i \times \Omega \times e^{\sum \mu_{\lambda f} x_2} \quad (4.7)$$

where I_{det} is the number of photons arriving at each facet's center of the detector.

x_2 is the intersection distance within each element in the sample taking the line between sample and detector.

$\mu_{\lambda f}$ is the element attenuation at a specific wavelength of the fluorescence.

Ω is the solid angle between the sample and the center of detector facets. This factor is explained in details in the following section.

4.8.1 Solid angle

The solid angle is a sector covered by the number of particles reaching the detector. Mathematically, it is an angle created in three-dimensional space that an object subtends at a point. It is considered a measure of how big an object appears to an observer when looking from that point. In our case of tomography the object is the sample voxel ("point S" in figure 4.14) and the point is the detector pixel ("point K" in figure 4.14). It is given by:

$$\text{solidangle}(\Omega) = \frac{\cos(\pi - \theta) ds}{4 \pi r^2} \quad (4.8)$$

where ds is the object surface;

r is the distance between source of incident photon and the pixel. It represents the radius;

θ is the angle between the source object direction and the normal of the object;

It is called the direction angle. Between 2 vectors (a) and (b) it is given by:

$$\text{directionangle}(a, b) = \arccos(a.x \times b.x + a.y \times b.y + a.z \times b.z) \quad (4.9)$$

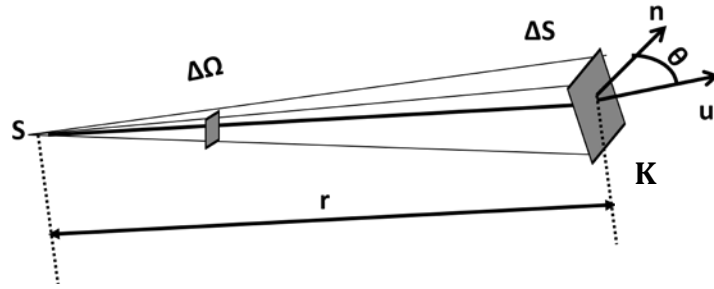


Figure 4.14: Solid angle of an incident photon in the direction of a particular pixel [40].

4.9 Simulated Compton scattering

When an X-ray photon collides with a quasi-free electron, an energy balance takes place. This is given by:

$$h\nu(+e^-) \rightarrow E_{kin}(e^-) + h\nu' \quad (4.10)$$

where $h\nu$ is the incident photon energy and E_{kin} is a kinetic energy. Thereby during the Compton collision, part of the incident energy is lost. Consequently, the scattered photon that continues its travel through the matter has a lower energy. This is in contrast to the photoelectric absorption [42]. Using the conservation of energy principle, the relation between the energy transfer and scattering angles can be derived. Assuming that the electron's binding energy is negligible, it is expressed as [14]:

$$E'_\gamma = \frac{E_\gamma}{1 + \frac{E_\gamma}{m_e c^2} (1 - \cos \theta)} \quad (4.11)$$

where E_γ is the energy of the incident photon or energy before collision;

E'_γ is the energy of the scattered photon or energy after collision;

θ is the scattering angle;

$m_e c^2$ is the rest-mass of the electron, it is equal to 511 keV.

So,

$$E'_\gamma = \frac{511}{(1 - \cos \theta + \frac{511}{E_\gamma})} \quad (4.12)$$

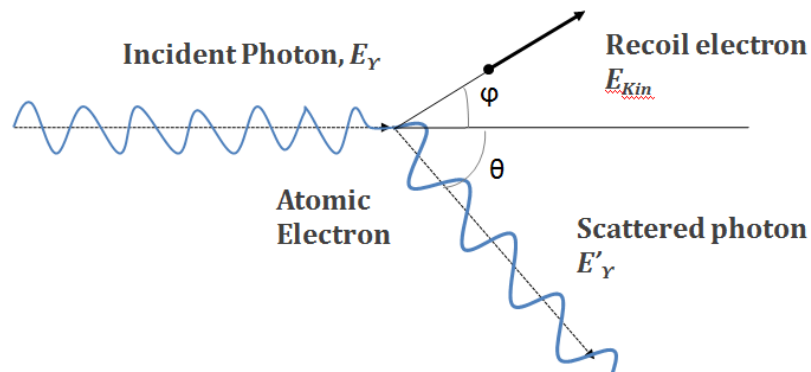


Figure 4.15: Compton scattering process

When an interaction takes place, the loss of incident energy increases with θ . At 0° there is no deviation and no energy loss and the maximum is at 180° . As the Compton scattering angle is unpredictable, the acquisition of the detector (illustrated in figure 4.16) is done over 2π except:

- The position of the fluorescence detector.
- The field of view (FOV) of the source.

So, the angle theta in the Compton scattering equation is restricted in these conditions. Optimization is done to precise in which position the Compton scattering has the highest value.

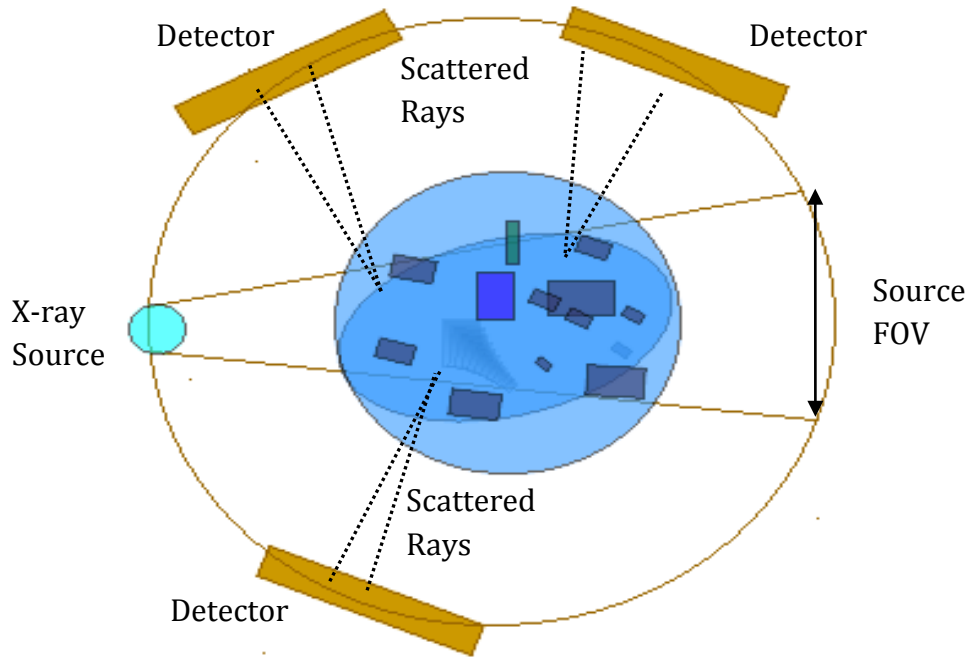


Figure 4.16: Compton scattering acquisition.

4.10 Parameters optimization

The fluorescence detection is a particular technique since the emitted photons must be of sufficient energy to cross the sample. At the same time, elements of low and high atomic numbers must be analyzed. For this reason the employed X-ray source is polychromatic and a convenient working tension must be selected. The range of the tube output used in this project is between 25 kV to 160 kV. The first optimization is that depending on the selected voltage, the output photons when impinged on a sample must react with all elements of the periodic table.

Moreover, in the optimization phase, the geometry of the experiment set-up is of high importance. Usually for each tomography type, “Compton Scattering”, “Transmission”, “Diffraction” and “Fluorescence”, specific geometrical conditions must be established. In our project, the fluorescence is well detected when the source and the detector are placed on the same side from the sample at a distance of 12 cm from the sample. By applying the best geometrical factor including the position and the distance between sample, detector and source, the detection system is better and the image quality can be improved.

Four more factors influence the result and must be optimized accurately. First, the number of holes in the collimator and the collimator septa length are chosen to confine the measurements. Usually, the multi-hole collimator with 1 cm septa length leads to a good acquisition. Then, the resolution and dimension of the detector and the collimator are chosen. The number of pixels that constitutes the array of detector is

selected according to the sample dimension. Generally, it is either 10 or 20 pixels. These sizes determine the system resolution.

The optimization of these parameters is done by applying the whole algorithm of imaging and image reconstruction technique on the same sample. The chosen sample contains elements of high and low atomic number. From the data entry file of the simulation code, we can change the parameters values. So every time a parameter is tested, different values are compared. Once the obtained number of photons leads to an image well reconstructed, the range of values for this parameter is considered.

4.11 Image reconstruction of Transmission tomography & Emission tomography

The basic concepts of image reconstruction algorithms and the supporting theory of each technique had been introduced in chapter 3. The previous simulation covered how to obtain a set of projections taken at different angles. This section will present the adopted and developed method for reconstructing images of fluorescent X-rays arising from the photoelectric effect. In practical application of image reconstruction, the question is which method to use. Either it is analytical or iterative it must be adapted to the collected data. This section will clarify the preprocessing of projection data and the numerical implementation of the mathematical reconstruction formulas and the post processing in case of blurred reconstructed image.

In order to obtain a good-quality reconstructed image, the followed methodology in the implemented algorithms is:

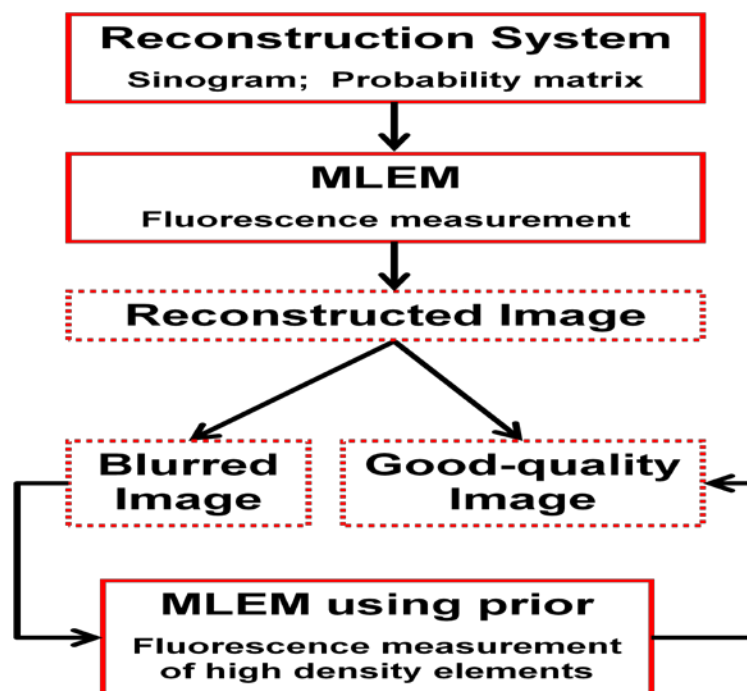


Figure 4.17: Reconstruction algorithms methodology.

4.12 Reconstruction model

The discrete system components used in reconstruction process $g = Af$ is described below.

g : the vector of projection data which is the sinogram ;

f : the vector of image data that is updated until an acceptable resolution image is obtained;

a_{ij} : the value of an element located at i^{th} row and j^{th} column of the system matrix A.

In what follows, these components are detailed along with their implementation method.

4.13 Attenuation map estimation of transmission tomography

4.13.1 Filtered back-projection description, implementation & sinogram creation

Geometrically, the back projection explained in chapter 3 is the propagation of the sinogram back into the image space along the projection paths. In order to avoid blurred image, the de-blurring is performed by applying the image filter operation. Thus, the projections are filtered prior to back-projection.

The filtered data is back-projected over the (x, y) plane. This is written as:

$$f(x, y) = \frac{\pi}{K} \sum_{i=1}^K Q_{\theta_i}(x \cos \theta_i + y \sin \theta_i); \quad (5.1)$$

where k is the total number of projections and Q_{θ_i} is back-projected to a point (x, y) .

Along parallel projections each filtered projection contributes equally to each image point (x, y) .

a) Tomography set-up:

In order to obtain a clear image from the FBP, the measurements employ different settings and parameters than the ones employed in the case of fluorescence.

- Different geometry is used in the FBP. The source and the detector faced each other and not at equal distances from the sample.
- More number of holes is used in the collimator.
- The attenuation is done based on source energies.

- The high working tension of the source is not efficient in the image production. The range that can be applied is between 25 kV and 65 kV maximum instead of 160 kV.
- The solid angle is directly between the source and the detector.

The adopted filtered back-projection procedure is outlined below:

- Establish the sinogram by the number of rays (detector size) and the number of projections (angles);
- Perform “FFT”, the Fast Fourier Transform;
- Perform filtering;
- Perform “IFFT”, the Inverse Fast Fourier Transform;
- Perform Back-projection;

b) Filtering:

During image reconstruction, high frequency components are introduced in the process. As these components are not present originally, they produce an undesirable response. These components are reduced by using smoothing windows. Windows function use point-by-point multiplication process to the input of an FFT to control any spectral artifact. They are used in combination with the ramp filter to suppress the higher frequency noise. Many types of windows can manipulate the input data [45], including Rectangular filter, Bartlett filter, Hanning filter, Hamming filter and Blackman filter.

Most of them smooth out or decrease toward zero the impulse response at each end of data cycle. These filters are detailed as follows:

Ramp:
$$w[n] = \begin{cases} 1, & n < M, \\ 0, & otherwise \end{cases}$$

Rectangular:
$$w[n] = \begin{cases} 1, & 0 \leq n \leq M, \\ 0, & otherwise \end{cases}$$

Bartlett (triangular):
$$w[n] = \begin{cases} 2n/M, & 0 \leq n \leq M/2, \\ 2 - 2n/M, & M/2 \leq n \leq M, \\ 0, & otherwise \end{cases}$$

Hanning (Von Hann):
$$w[n] = \begin{cases} 0.5 - 0.5 \cos(2\pi n/M), & 0 \leq n \leq M, \\ 0, & otherwise \end{cases}$$

Hamming:
$$w[n] = \begin{cases} 0.54 - 0.46 \cos(2\pi n/M), & 0 \leq n \leq M, \\ 0, & otherwise \end{cases}$$

$$\text{Blackman: } w[n] = \begin{cases} 0.42 - 0.5 \cos(2\pi n/M) + 0.08 \cos(4\pi n/M), & 0 \leq n \leq M, \\ 0, & \text{otherwise} \end{cases}$$

Where M is the length of the window w is the window value and n is the number of sampling signals [45]. Since we are working in the frequency domain, filtering is an easy operation done by multiplication instead of convolution. In this project, all of these filters are tested during the filtered back-projection process and the best one that enhances our measured data is the “Hamming filter”.

c) Sinogram creation

As explained in previous chapter the sinogram is the measured data collected around the sample. For each angle position (θ) a projection data is saved on each pixel of the detector. These data are stacked together to form the sinogram. Figure 4.18 shows many rows of the sinogram corresponding to different projections.

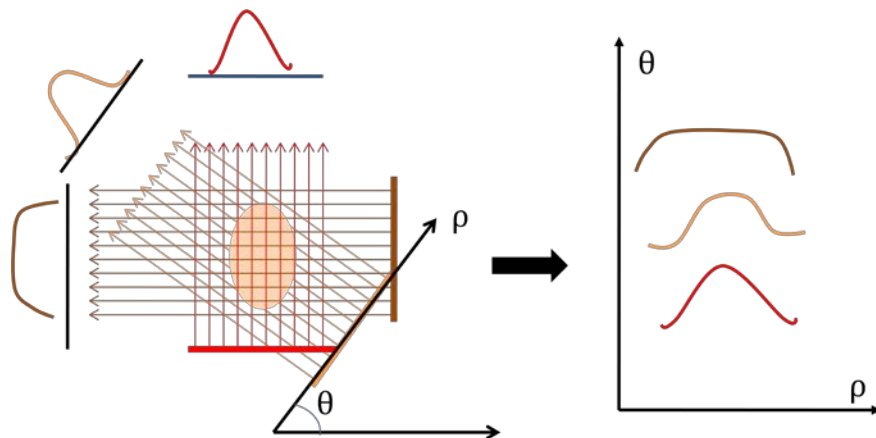


Figure 4.18: Sinogram formation.

4.14 Fluorescence map estimation of emission tomography

The X-ray fluorescence tomography is a well suited non-destructive testing and it is considered an accurate imaging technique for the following reasons:

- It is a useful tool for qualitative and quantitative analysis. Since each element peak occur at a fixed known energy, the element's type can be defined; whereas the peak amplitude is directly related to the concentration of the element.
- It combines emission tomography with transmission tomography to depict the distribution of specific elements inside the sample. The absorption coefficient distribution is obtained using transmission tomography, whereas fluorescence photons emitted from sample elements are detected using emission tomography.

- Self-absorption correction can be completed by measuring the attenuation coefficients.
- Multiple fluorescence lines can be collected due to the sample rotation and the whole geometrical set-up.
- Capability of estimating the elemental composition of unknown samples by providing a spatial distribution of specific elements in the sample.
- It is a non-destructive technique and the sample is examined without any pre-treatment. In addition, the technique is fast and easy-to-use.

4.14.1 Probability matrix estimation

The probability matrix, called also system matrix or reconstruction matrix, is denoted by A in the reconstruction model $g = A f$. The unknown image that we are looking for is represented by pixels. What the matrix data provide, are the probabilities of each photon, emitted from these pixels at a specific X-ray fluorescence energy, to be detected. In addition to the probabilities, it takes into account the geometrical set-up of the system and many physical parameters such as attenuation, scattering and collimation response. Practically, another effect interferes which is the detector dead area. For all these reasons, not all the emitted photons from a pixel i are detected by the bin j of the detector. Therefore, the A_{ij} elements included in the reconstruction process are limited only to those that are actually detected. The remaining is considered as non-detected counts. This is expressed by [44]:

$$A_{ij} = \frac{\text{photons emitted from pixel } i \text{ detected from detector } j}{\text{photons emitted from pixel } i \text{ totally detected}} \quad (5.2)$$

Before evaluating the probabilities, we have to set the matrix dimension. The matrix is recognized as a transition matrix since it represents the relationship between values in both the slice and the sinogram. For example, in figure 4.19 we have 4 projections (at 0° , at 90° , at 180° and at 270°) of an 8 pixels width detector, applied to an image of 64 pixels. The matrix product of this scanning is expressed as:

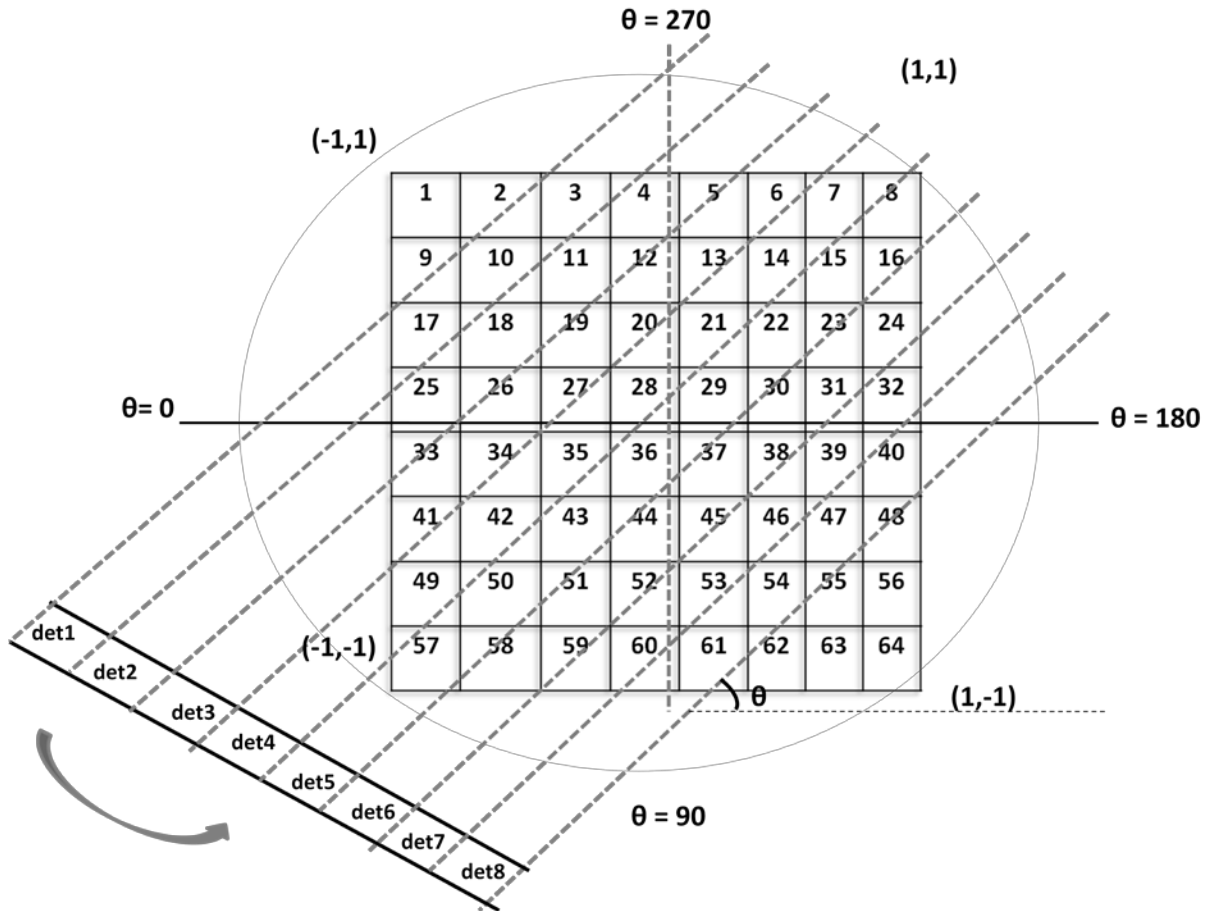


Figure 4.19: The matrix weights formed by the projections on detector bins.

A simplified model of this matrix is given in figure 4.20. Before the implementation of the reconstruction procedure, the matrix elements computation is performed. Many techniques are used during implementation of these elements calculation. Some of them, based on Monte Carlo, require a long computation time. Therefore, another technique, explained in the following section, based on the angle of view and on the geometry of the tomograph is used.

[illegible]

Figure 4.20: The matrix product (done according to figure 4.19).

In the implementation of the probability matrix system, the rows correspond to the detector in all positions angles and the columns depend on the original sample size. Hence, the system matrix is a large matrix to be stored and manipulated in typical application. Its dimension depends on:

- The number of detector pixels multiplied by the number of projection angles (number of rows).
- The number of pixels which is relevant to the size of the reconstructed image (number of columns).

As in the matrix of figure 4.20, we have 32 rows (8 detector width \times 4 projections) and 64 columns corresponding to the 64 pixels of the initial image. Note that the sample or the image we need to obtain is considered as a group of pixels and the detection of radiation emitted from these pixels is implemented as follows.

Calculation of the probabilities is based on the evaluation of the matrix weights. A weight is the probability that a photon emitted in a given voxel contributes to a projection in a given bin on the detector. This principle is illustrated in figure 4.21 where the photons are assumed to be emitted isotropically from each pixel and a linear orbit is considered as the path followed by each photon. In this figure, δ_{ij} is the distance between pixel i and detector j , W_D is the width of each detector and φ is the solid angle.

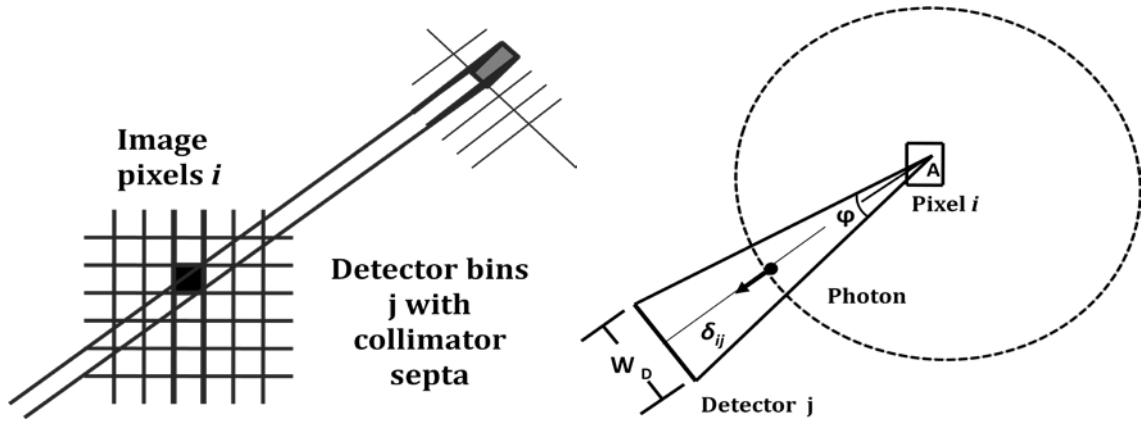


Figure 4.21: The geometry of photons emission from pixel i reaching detector bin j [44].

As it can be seen in figure 4.21, if a photon is emitted from pixel i the probability that it will be detected from detector j depend on the percentage of the intersection area between this pixel and the “detection zone”. In order to calculate the elements of this matrix, we have to compute the common area. This is illustrated in figure 4.22. Each pixel is determined by 4 lines (up, bottom, right and left). The intersection between these four lines and the 2 lines of the detection zone (y_1 and y_2) determines the common area. When one or both of these lines intersect the pixel, the common area is determined from the difference $E = E_1 - E_2$, where E_1 is the area under y_1 and E_2 is the area under y_2 .

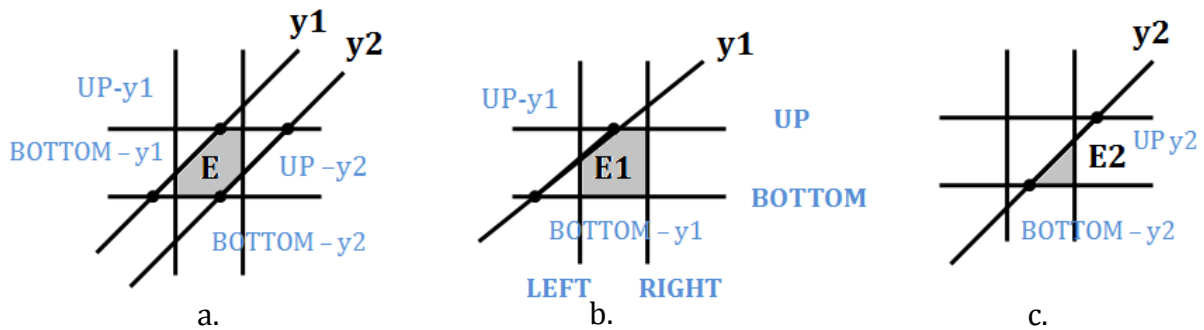


Figure 4.22: Representation of the common area of a pixel i and the detection zone of a detector j [44].

The arrangement steps are:

- Determine, in the original image, the position of each pixel.
- Depending on the rotating angle, adjust the values to be suitable with the detector view.
- Define the limits (up-bottom-right-left) of each pixel.
- Determine the equations (y_1 - y_2) of the detector scanning lines.
- Define the intersection of detector scanning lines with pixel limitations.
- Define the areas E_1 , E_2 as the integral (\int) areas under lines y_1 & y_2 respectively.

Note that these steps are done for each pixel of the image with each pixel of the detector at each rotation step.

Based on these geometrical and statistical factors, the probability of fluorescence detection depends on the percentage of the intersection area between each pixel and the detection zone. It is given by:

$$E_{\%ij} = \frac{E_1 - E_2}{(W_D Det / \pi_\theta \sqrt{N})} \quad (5.3)$$

This intersection area is called the emission probability common area $E_{\%ij}$. So the probability is derived from what each detector can see. The term $W_D Det / \pi_\theta \sqrt{N}$ represents the “width of the pixel”. It is derived from:

- Det , the total number of detectors in all projections.
- W_D , the detector width.
- π_θ , the number of projection angles.
- N , the total number of image pixels.

In the presence of collimator, same steps (indicated in Annex E) are repeated but many more considerations concerning the collimator are taken into account. Collimator width, collimator hole width, distance of capture and relative position of the collimator with respect to the detector are all incorporated in the equations of the probability matrix.

This process is implemented as 2 functions in the simulation code. The first one encloses the probability matrix without collimator and the second encloses the probability matrix with collimator. The probability matrix is simulated having 2 dimensions conforming to the following steps:

- Define the rotation angle step as: $360^\circ / \text{number of projections}$;
- Create the 1st loop over the number of projections;
- For each projection, define each time the increment of rotation angle step named theta as: $\theta = \text{rotation angle step} \times \text{precised projection number}$;
- Create 2nd loop over the pixels of detector;
- Create 3rd loop over the total image pixels;
- Implement the probability matrix having 2 dimensions, the number of detector in each projection angles (1st and 2nd loop), and the number of pixels (3rd loop);

The weights or the matrix values are between 0 and 1. It combines the geometrical factor and the probability factor. Figure 4.23 represents a resulting matrix formed by:

- $\text{an image of } 24 \times 24 = 576 \text{ pixels: number of columns.}$
- $14 \text{ projections} \times 7 \text{ detector pixels} = 98 : \text{number of rows.}$

The detailed probability matrix implementation steps are listed in Annex E.

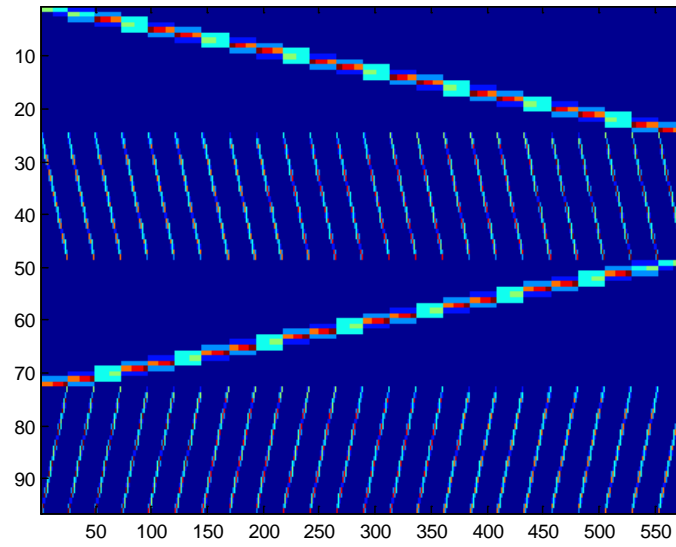


Figure 4.23: Probability matrix values displayed.

4.14.2 MLEM implementation

After establishing the sinogram and the probability matrix, the reconstruction algorithm is implemented. In the case of fluorescence, an algorithm that extracts from the collected measurements the maximum available information is required. The quality of the reconstructed image relies strongly on the chosen reconstruction algorithm. Since the fluorescence measurements are of statistical nature, the best strategy is to use an iterative statistical method in which we can introduce any constraint on the activity distribution. The MLEM has important features to be applied. First of all, the fluorescence emission is of low energy thus the total number of counts is low. Then, fluorescence emission and fluorescence detection are probabilistic. The MLEM takes into account the Poisson nature of emission and the statistical characteristics. For this perspective, the optimization criterion based on the estimation of the maximum likelihood can approach the solution. Bayesian methods can also be implemented in order to improve the results from the unknowns in case of incomplete data.

The implementation of the MLEM algorithm comprises the following steps:

- The set of data collected that produces the sinogram is extracted and implemented in the MLEM equation. It is expressed by " g_i " where " i " is the dimension formed by number of detector pixels multiplied by the number of projection angles.
- The weights values that produce the probability matrix are also extracted and implemented in the MLEM equation. It is expressed by " A_{ij} " where " i & j " are the dimensions of rows and columns respectively:
 - $Rows = Number\ of\ detector\ pixels \times Number\ of\ projections;$

- *Columns = Number of image pixels;*

As explained in the previous section, A_{ij} depends on the irradiated fluorescence and the geometrical factor of detection.

- The number of iteration, expressed by “ k ”, is specified. It is considered as a parameter for image optimization. Usually in the MLEM, it is between 20 and 200.
- The MLEM equation is then applied pixel by pixel to reach the whole image. It is given by:

$$f_i^{k+1} = \frac{f_j^k}{\sum_{i=1}^N A_{ij}} \sum_{j=1}^{Det} \frac{A_{ij} g_i}{\sum_{j'=1}^M A_{ij'} f_{j'}^k} \quad (5.4)$$

where:

f_j^k, f_i^{k+1} is the current and the updated estimate of the image;

$f_{j'}^k$ is an initializing vector that is updated each iteration;

The ratio $g_i / (\sum_{j'=1}^M A_{ij'} f_{j'}^k)$ is a factor that represents the measured numbers of counts to the current estimate of the mean number of counts in bin i ;

$\sum_{j=1}^{Det} (g_i / \sum_{j'=1}^M A_{ij'} f_{j'}^k) A_{ij}$ is the back-projection of this ratio for pixel j ;

The equation model can be interpreted as:

$$Image^{k+1} = Image^k \times \text{Normalized Backprojection of} \\ \left(\frac{\text{Measured projections or number of counts}}{\text{Projection of image}^{(k)} \text{ or current estimate of the mean number of counts}} \right)$$

During the process of one iteration, sinogram values and the probability matrix values are loaded and the result of the MLEM equation is updated. Therefore, an efficient implementation is needed.

Tomography set-up

The resulting image and the image quality and resolution are improved using optimization factors. For each parameter, a value is assigned after verifying the output signal or the image result itself. The settings listed below are of critical importance since our goal is to acquire the highest number of fluorescence photons.

- The geometrical factors for a sample around 3 to 5 cm³ placed in a central position:
The source and the detector are placed from the same side of the sample and not opposite. The angle between source and detector-collimator is almost 45°. Their position is far from the sample at a distance of 15 cm.
- The detector width is 5 cm.

- The adopted collimator holds the maximum number of holes. It has the same width of the detector. It contains 4 to 5 holes, 0.2 cm each.
- Note that the detector and the collimator are close to each other for better performance.
- The collimator septa that confine the beam into one direction is set to 1 cm.
- The attenuation is done based on source energies between source and sample and on fluorescence energies between sample and detector.
- A variety of acceptable results are obtained by varying the working tension. The efficient value for the fluorescence data is 120 kV source output.
- The solid angle is computed between the sample voxels and the detector pixels.
- The sample rotation angle step of 3° over 360° gives an acceptable resolution. Thus, the number of projections is 120.
- In the reconstruction process, the iteration number ranging between 150 and 200 iterations is enough to obtain a well-defined image.

A general illustration of MLEM process is displayed in figure 4.24:

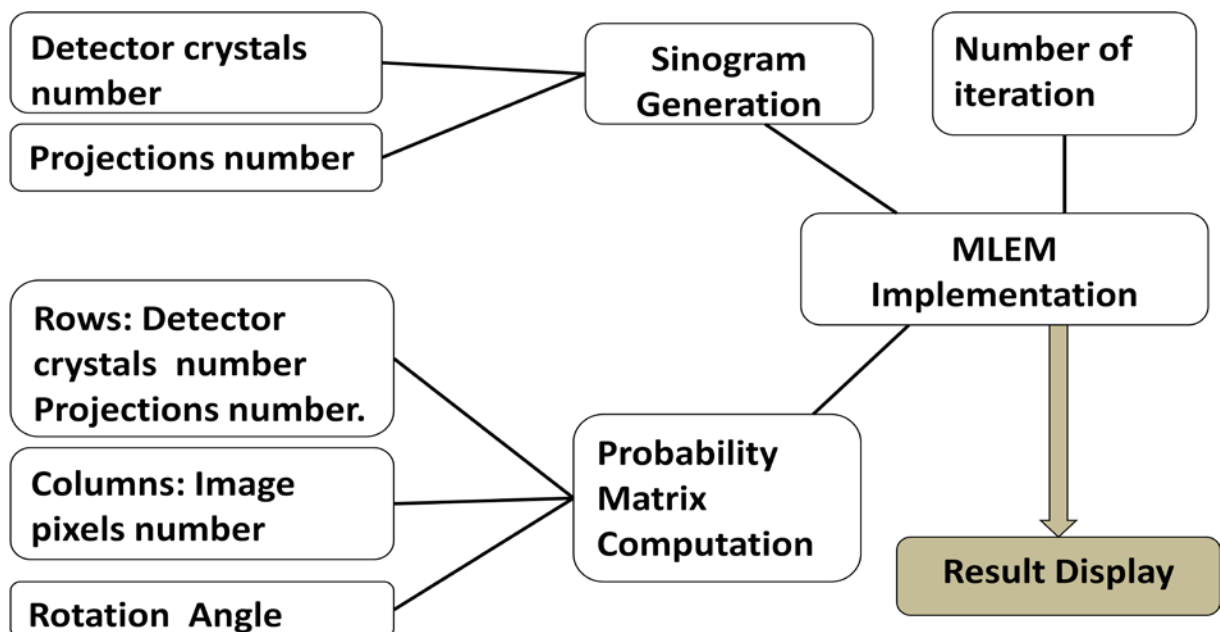


Figure 4.24: MLEM implementation procedure.

4.15 Regularization

The optimization of settings and parameters improves the acquisition and hence the produced image. Although, in some cases, the presence of objects with high atomic number close to each other leads to artifact and discontinuity. This is due to the fact that they strongly attenuate the incident beam and this will lead to a blurred image. In order to improve image quality in this case, it is necessary to incorporate prior information. Usually, prior information about the image is used to optimize the maximum likelihood.

Thus, the distribution of linear attenuation coefficient will be easily found for a set of measurements. This technique is referred to as regularization [43].

Many techniques of regularization can be implemented. In this work two of them are applied. The first one is when the noisy or blurred images are penalized by the prior since it is considered as an assumption of what the true image is. Thus, the prior knowledge is introduced as a constraint in order to favor the convergence of EM process. The second one is the selection of “the number of iterations” to reach convergence. Practically, as explained in chapter 3, the approach of Maximum A posteriori (MAP) technique, based on Bayesian inversion method, can be applied for this task. In this project, the proposed solution for regularization is to obtain the prior image from the FBP, then incorporating it in the MLEM.

4.15.1 Optimization of data acquisition

In order to achieve an accurate image reconstruction, an optimization phase, in which parameters are settled, must be available in the computing system. Many parameters settings contribute to the accuracy of data acquisition and in the quality of the reconstructed image. Therefore, during optimization, the code is adapted to the experiment set-up. Figure 4.25 lists the parameters relevant to scanning, projections and reconstruction techniques.

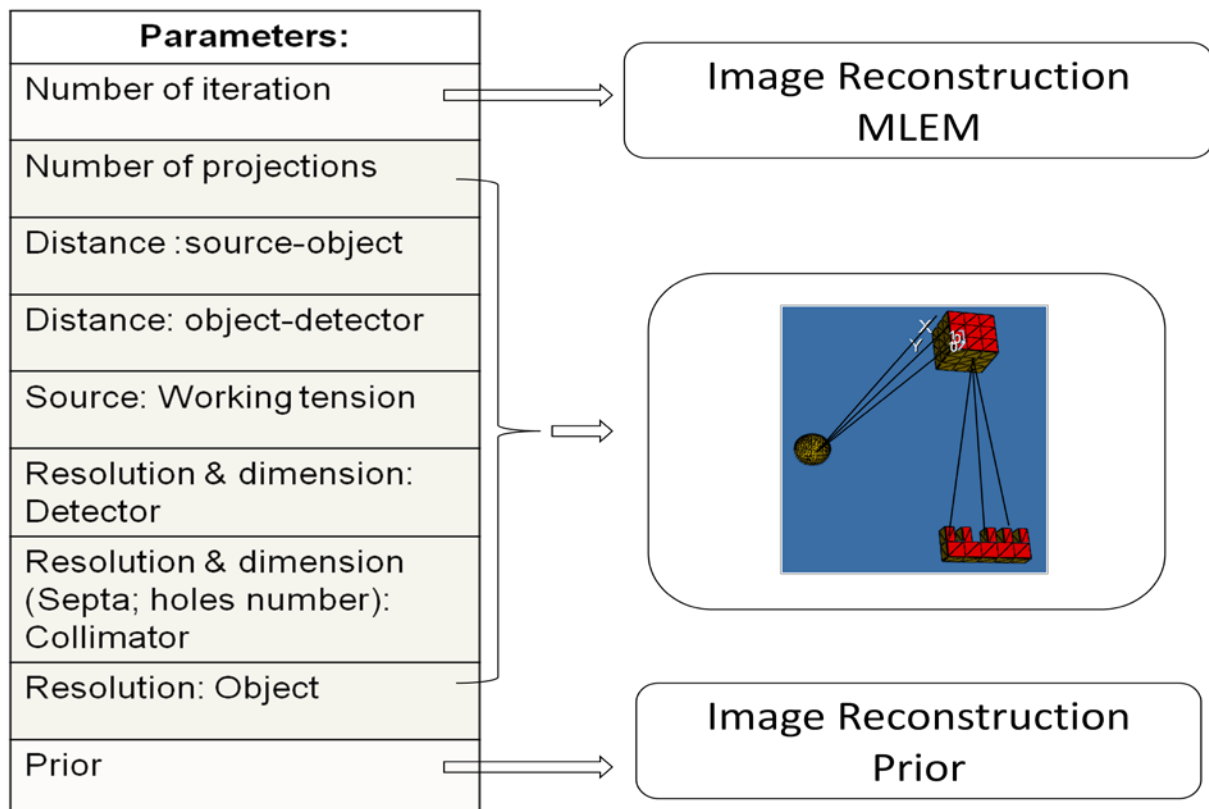


Figure 4.25: Optimization parameters.

4.15.2 MLEM result with prior

The overall implementation of the prior in the image reconstruction is illustrated in figure 4.26.

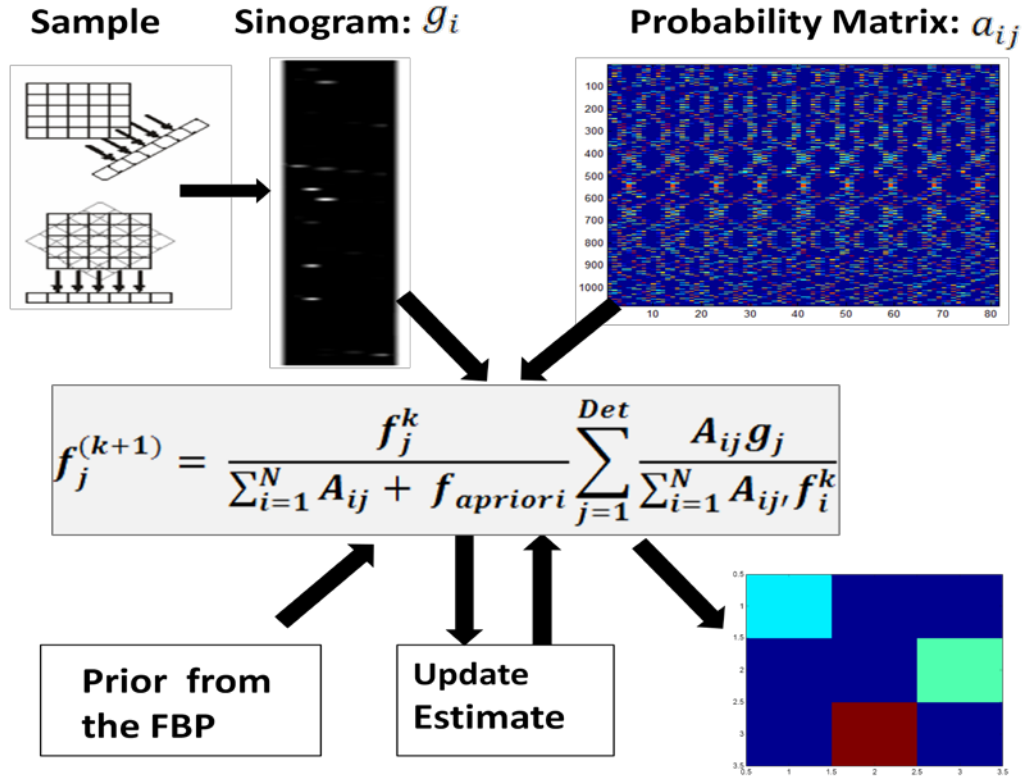


Figure 4.26: Implementation of image obtained from FBP in the image reconstruction process.

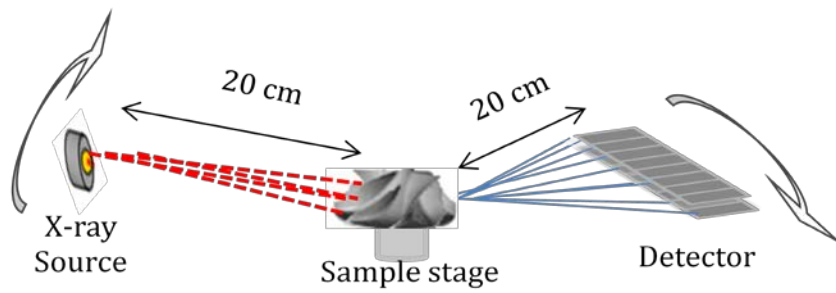
4.16 Methodology of experimental validation

4.16.1 Description of the measurement system used for fluorescence validation

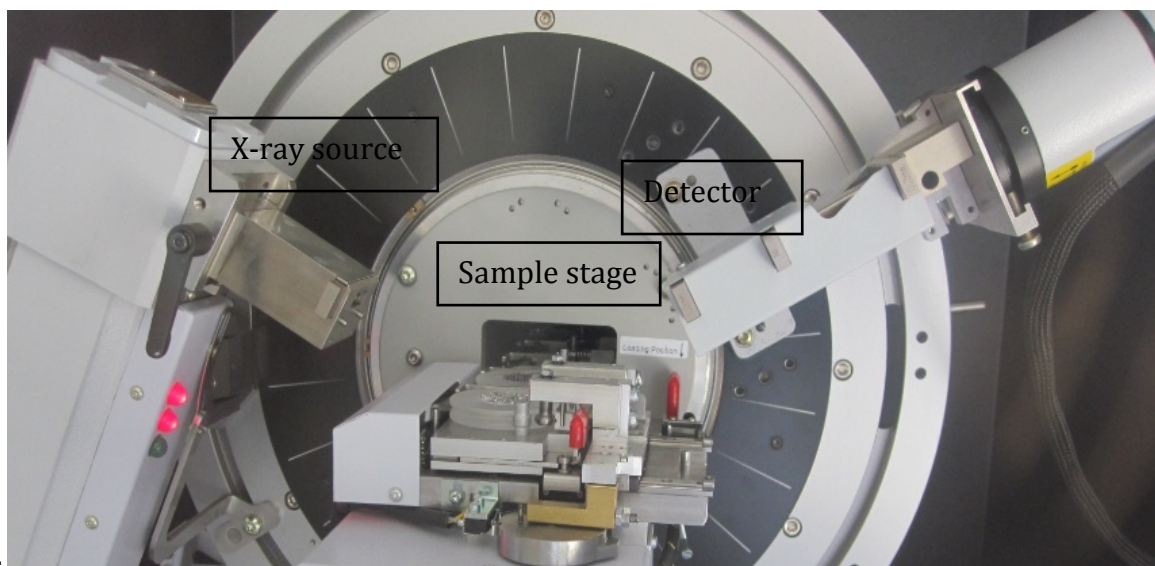
The experimental arrangement for a good acquisition, shown in figure 4.27 is based on the optimization and settings done on the simulation part. The sample is placed at a distance of 20 cm equidistant from the source and the detector.

The emitted beam is exposed to collimation before being detected. The collimator mounted directly in front of the detector is an attenuator that is made of Copper “Cu” and Nickel “Ni”. This type of collimator is an absorber that attenuates the beam by about 2 orders of magnitude.

The angle between source and detector is almost 120°. The source-detector are rotating at 3 degree angle step; thus 120 projections are performed.



a.



b.

Figure 4.27: (a) Geometrical arrangement; (b) Experimental detection system.

a) The X-ray source

The object inside the sample holder is irradiated by an X-ray source shown in figure 4.28 with the following specifications:

- 2.2kW Cu anode long fines focus ceramic X-ray tube.
- 40 kV/40 mA X-ray tube power running conditions.



Figure 4.28: X-ray source.

b) The detector

The emitted beam is exposed to collimation before being detected. The collimator mounted directly in front of the detector is an attenuator that is made of Copper “Cu” and Nickel “Ni”. This type of collimator is an absorber that attenuates the beam by about 2 orders of magnitude. The detector, shown in figure 4.29 has the following specifications:

- A *NaI* dynamic scintillation detector type.
- Detector maximum count rate: $2 \times 10^6 s^{-1}$.
- Detector electronics capability count rate up to $3 \times 10^7 s^{-1}$.
- Detector thickness: 5 cm ; Detector diameter 5 cm.
- Detector pixels: 50 pixels of 0.2 cm.



Figure 4.29: Scintillator detector.

4.16.2 Objects used for experimental validation

The accomplished simulation results show that “Aluminum” and “Water” have very close responses of fluorescence emission and attenuation. Thus, in order to analyze an object in a solution, Aluminum and Lead has been used (figure 4.30(a, b)). Moreover, the Lead, immersed in the Aluminum (figure 4.30(c)), is expected to be well discriminated. Another geological sample which is the “Amber” has been used (figure 4.30 (d)). The amber is a fossilized material that is highly fluorescent when exposed to X-ray. Consequently, the analysis through X-ray fluorescence emission is highly important to specify the type of amber. These elements are placed in a sample holder of 5 cm made of “PMMA” polymethyl-methacrylate which is a thermoplastic material with good sample consistency.

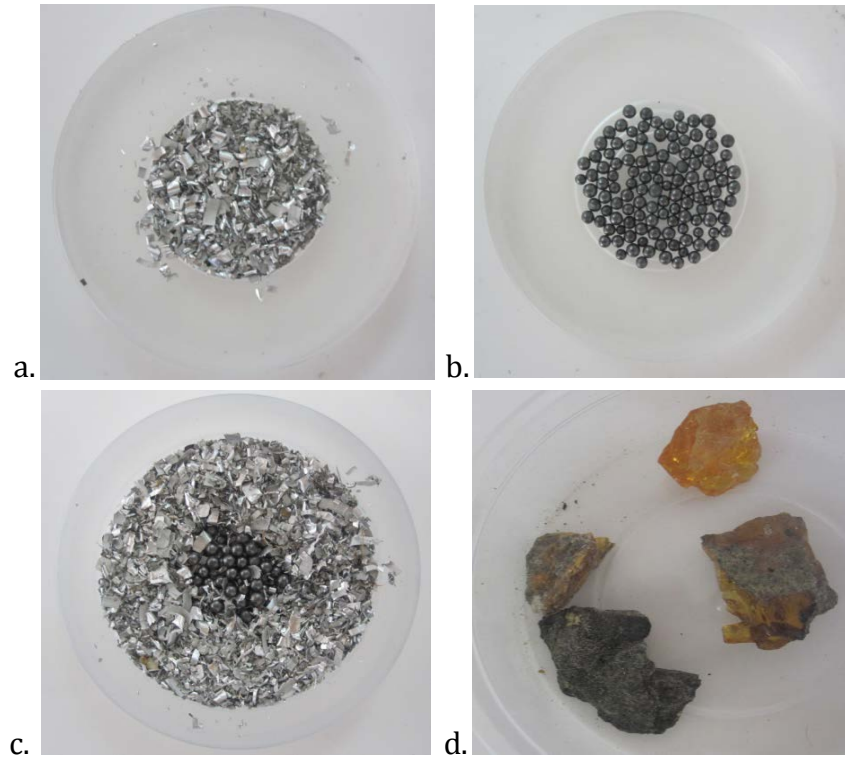


Figure 4.30: (a) Aluminum sample “Al”; (b) Lead sample “Pb”; (c) Lead immersed in Aluminum; (d) Different types of amber.

Information about parameters settings has been extracted from analysis performed via simulation on such samples dimension:

- Source and detector are placed at a distance of 20 cm from the sample.
- The X-ray source is 40 kV/40 mA.
- The source and detector are rotating around the sample at an angle step of 2°.

4.17 Conclusion

The implementation of this code shows a good robustness. This is due to the accurate incorporation of the absorption correction factor and the probabilities factors during scanning. In addition, the StL format, a well-known CAD numerical format, enables the whole experiment system to be simulated and to apply the ray tracing technique. The last step was the optimization in which we find the best settings to have appropriate fluorescence data. The use of simulation code is essential for the set-up arrangement of an experiment. Besides the accuracy, it provides the skills of choosing the appropriate parameters. Then, the fluorescence measurements are processed and a computational reconstruction method is built to reproduce accurate images. The developed reconstruction method must be able to analyze objects of all types, shapes and dimensions based on fluorescence data.

For image reconstruction, the nature of fluorescence emission and the characteristics of events during scanning and detection come up with a statistical and iterative method. The *Expectation Maximization* takes into account these factors. Moreover, the established probability matrix relates the mathematical model of data acquisition system to the probability of fluorescence functions in the object distribution. From the set of measurements and the weights values of the system matrix, we obtained a set of possible images. The image that has the highest probability that the observed data reflects the original object distribution is the *Maximum Likelihood Estimate*. In case of blurred image, regularization or what is called penalization is needed to produce better results. In our case, other than the optimization of parameters and settings, the proposed solution was to incorporate “prior information”. This prior is obtained by applying an analytical image reconstruction technique onto the system. The FBP has been used to produce an image that is considered the “apriori” or “the prior image”. During the FBP process, a proper filter is selected and applied on the raw image. Lastly, the prior information is incorporated in the image reconstruction function.

Chapter 5 Results & Discussion

5.1 Introduction

In this project, an experimental application of the fluorescence tomographic system is performed. First of all, an X-ray transmission computed tomography is used to localize the fluorescing elements. Then, an emission tomography is applied in order to identify and discriminate between different elements. The simulation results, its validation, the resulting data acquisition and the obtained images are displayed and discussed in this chapter.

5.2 Simulation results

Carrying out a simulation code defines a measurement system with a wide range of parameters optimization. In order to maintain control between the software system and the proposed work, a validation is performed by achieving an experimental work. This section presents the simulation and experimental results. Then, the obtained fluorescence spectrums are illustrated in details and compared with the simulated results.

5.2.1 Sinogram validation results

Figure 5.1 shows sinograms of 120 projections and of 50 projections for a short detector and long detector simulated in this project; whereas, figure 5.2 displays clearly the accuracy of the generated sinogram when it reflects the number of objects inside the sample. These 2D arrays of projection data are displayed using the Matlab. The sinogram is considered the input data for image reconstruction.

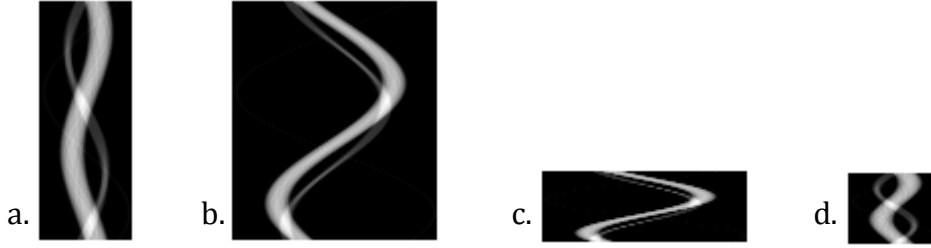


Figure 5.1: (a, b) 120 projections;(c, d) 10 projections; (a, d) 20 cm detector;(b, d) 40 cm detector.

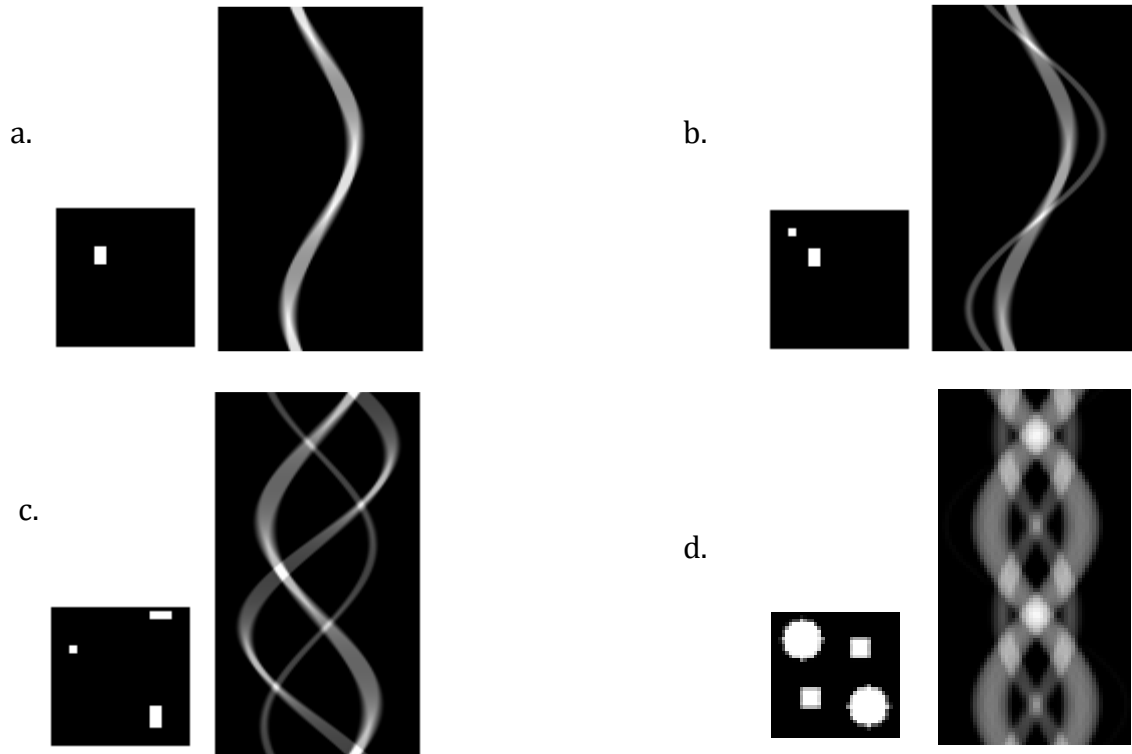


Figure 5.2: Sinogram reflecting 1 object (a); 2 objects (b); 3 objects (c); 4 objects (d).

5.2.2 Simulated transmission tomography results

In order to validate “the intersection mathematical technique” and “the extraction of attenuation coefficient”, a transmission tomography is simulated. An StL geometrical object is placed between the polychromatic source and a 2-Dimension detector. The code is validated at a first stage by simulating the interaction with simple objects representing spheres and cubes of known dimensions as shown in figure 5.3. These objects are 3D distribution situated between the source and the detector at the position shown.

Figure 5.4 represent the obtained simulated images of a sphere and a cube respectively. The simulated results reflected exactly the geometrical specification of the

objects taking into account the distance between the source, object and the detector. Their sinograms obtained at 120 projections are represented in figure 5.5.

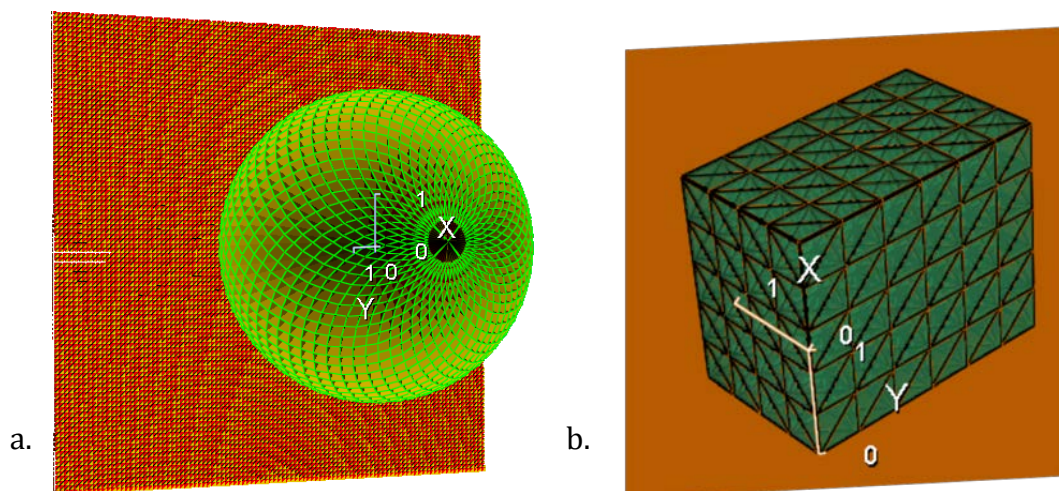


Figure 5.3: STL image of (a) a sphere; (b) a cube.

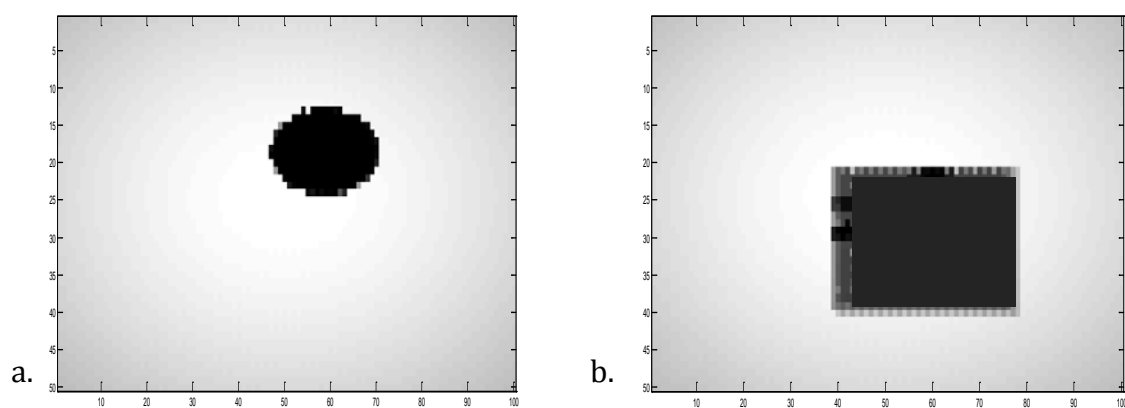


Figure 5.4: Simulated image of (a) a sphere; (b) a cube.

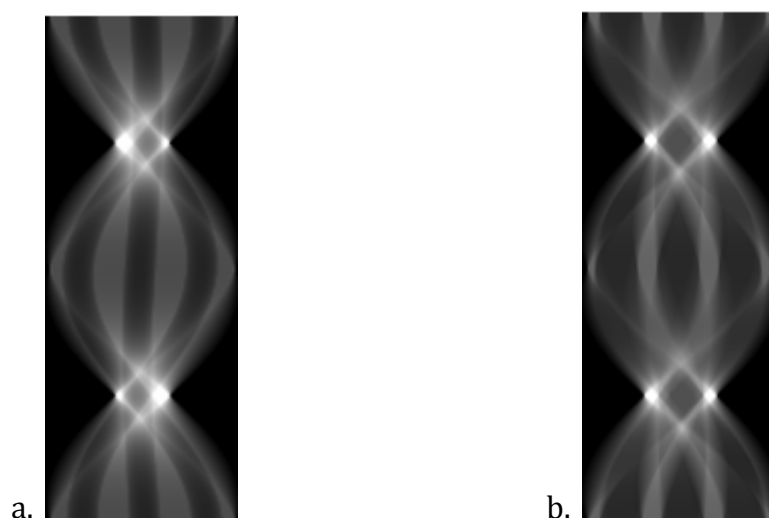


Figure 5.5: Corresponding sinograms of (a) a sphere (b) a cube.

5.2.3 Simulated fluorescence results

a) X-ray fluorescence spectrum

One of the important optimization parameter is to select the source voltage and consequently the X-ray fluorescence spectrum. To test this parameter, a set-up arrangement, shown in figure 5.6, consists of the following components:

- A polychromatic X-ray source used at different working tension;
- A 9-pixel detector width;
- 1-hole collimator same width of the detector and the hole located in the middle.
- A sample of water containing either a Lead element (*Pb*) or a Germanium element (*Ge*).

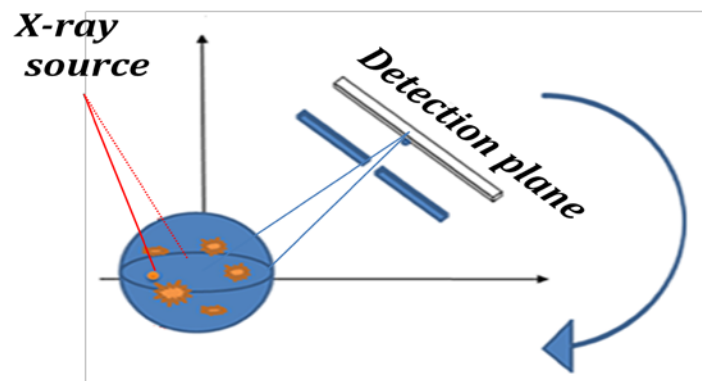
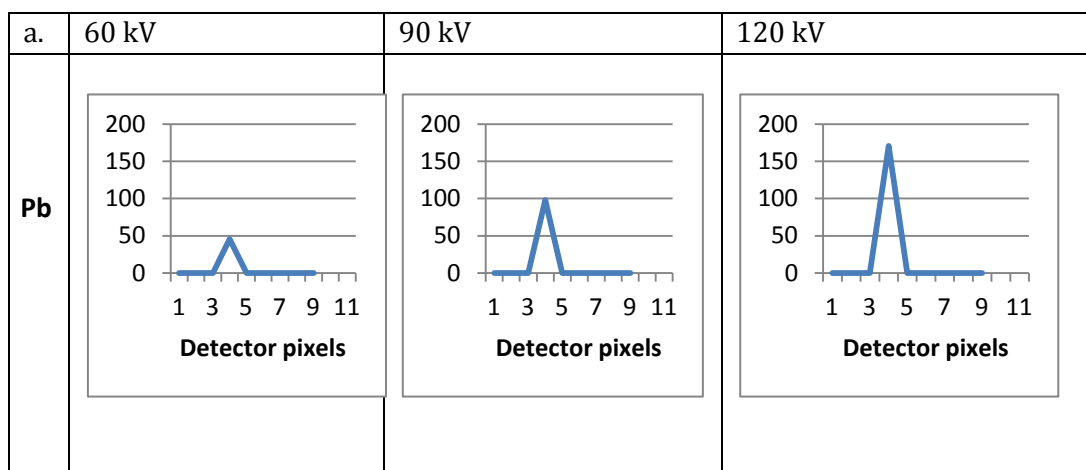


Figure 5.6: Fluorescence emission with 1 hole collimator.

The graphs (in figure 5.7 (a)) show the results of number of photons reaching the detector through the collimator hole. Each column represents a selected working tension of the X-ray source whereas the rows represent 2 different sample elements (Germanium (*Ge*) and Lead (*Pb*)). The final graph, shown in figure 5.7(b), reveals that for both elements the number of photons increases with the increased output voltage.



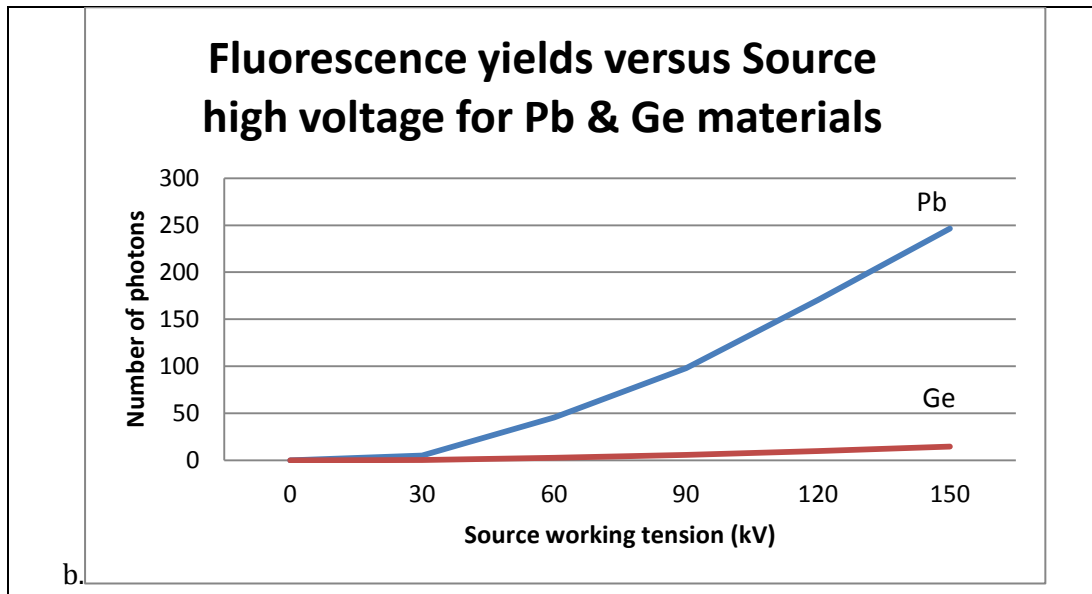
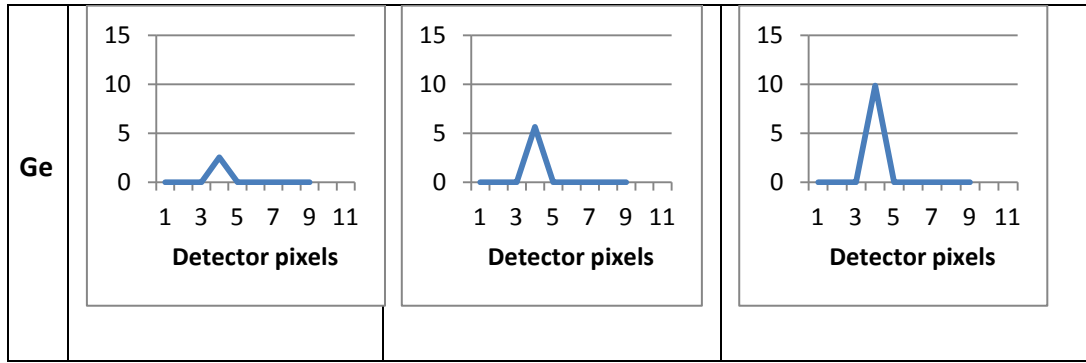


Figure 5.7: Lead & Germanium fluorescence with respect to X-ray source voltage.

Based on Moseley's law, the fluorescence energies are estimated (see table 5.1). The graph in figure 5.8 represents the measured fluorescence values for different elements bombarded by a polychromatic X-ray source. Different elements immersed in water are tested.

Table 5.1: Fluorescence energies based on Moseley's law.

Element type	Atom shell	Fluorescence energy (keV)
Aluminum (Al)	K-shell	1.50048
Aluminum (Al)	L-shell	0.215136
Water (H2O)	K-shell	3.01138
Water (H2O)	L-shell	0.431766
Lead (Pb)	K-shell	68.36562

Lead (Pb)	L-shell	9.802134
Titanium (Ti)	K-shell	4.59522
Titanium (Ti)	L-shell	0.658854

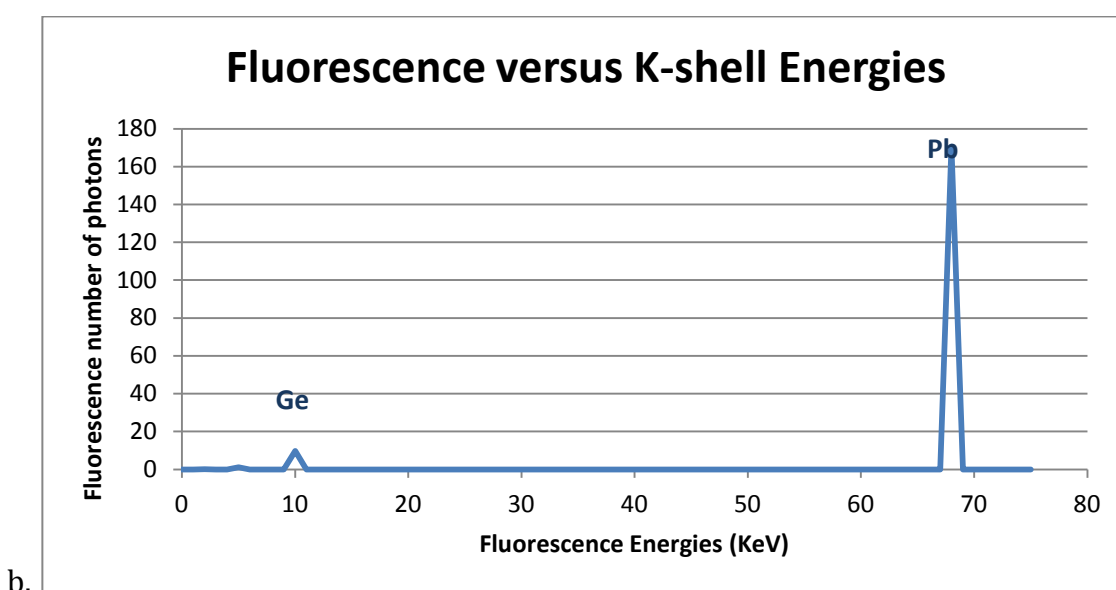
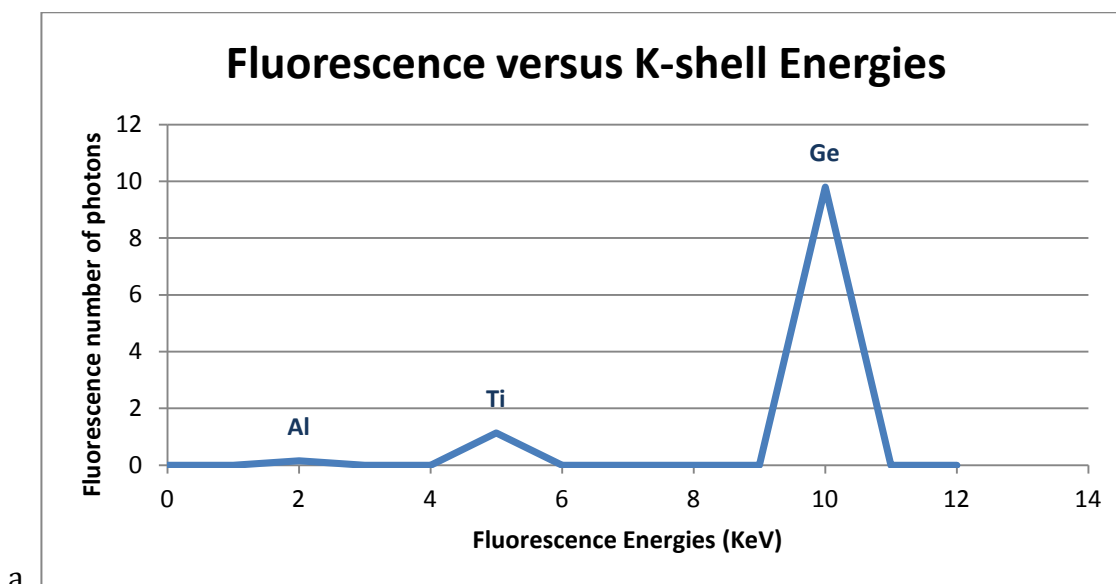


Figure 5.8: Emitted fluorescence of different elements at specific energies.

The number of counts in figure 5.8 (a) shows a spectrum of low atomic number objects like Aluminum (Al: atomic number 13), Titanium (Ti: atomic number 22) and Germanium (Ge: atomic number 32). Whereas in figure 5.8 (b) the spectrum of a high atomic number element like Lead (Pb: atomic number 82) is displayed. The lead recorded a high fluorescence emission value in comparison to the remaining elements. The obtained result comes out with a proof that 'the fluorescence yield' increases with increased atomic number.

b) Testing of fluorescence attenuation

The previous test is a typical X-ray fluorescence analysis for an object in a solution. In order to analyze the self-absorption of a sample, a lead element is placed in different media including *Ge*, *Ti*, *Al*. The obtained fluorescent peaks shown in figure 5.9 are lower and the attenuation of the fluorescent radiation of lead depends on the property of the medium. Note also that the decrease of the fluorescence peak is irrelevant to the decrease of the atomic number of the medium.

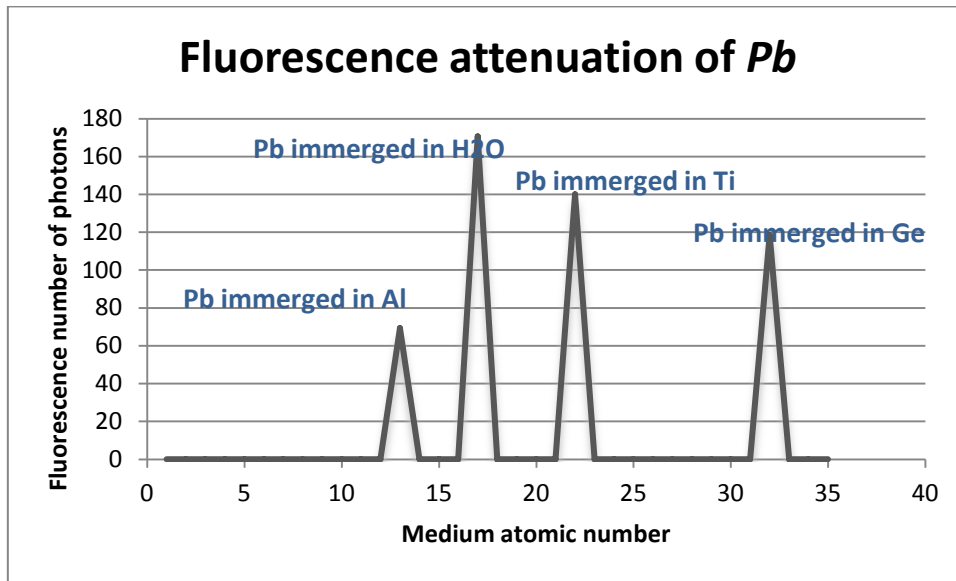


Figure 5.9: Fluorescence counts of lead (Pb) immersed in different medium.

5.2.4 Filtered Back Projection (FBP) validation

Test samples are used to validate the FBP simulated algorithm. The results shown in Figure 5.10 are of 120 projections that represent 3° step angle and 61 rays that correspond to the detector pixels.

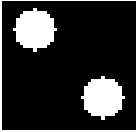
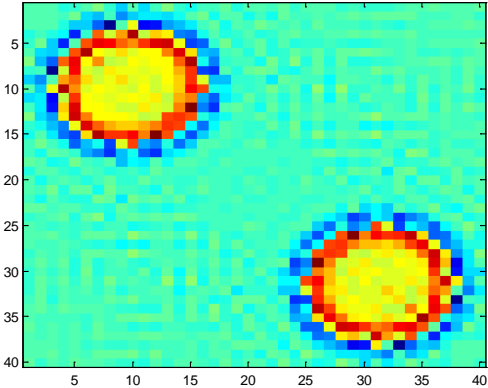
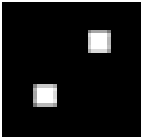
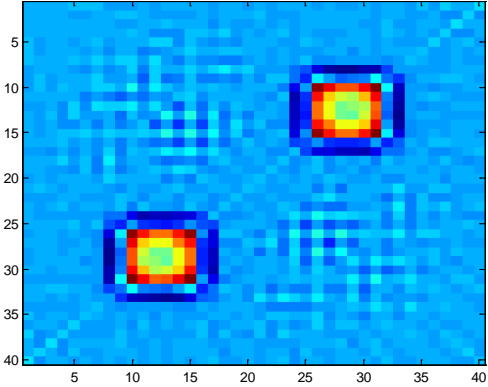
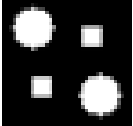
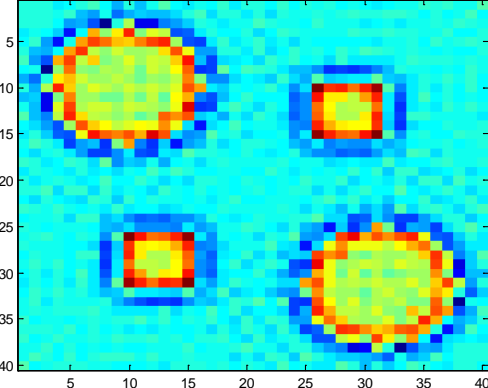
Original Image	Reconstructed image using FBP
	
	
	

Figure 5.10: Reconstructed image of test samples obtained from FBP method.

5.2.5 Maximum Likelihood Expectation Maximization (MLEM) validation

The first step is to validate “the probability matrix computation” and “the MLEM algorithm implementation”. The procedure is to apply the system on a known shape so that the resulting image is predicted. Figure 5.11 illustrates the obtained result with the in below implementation steps.

- An image of known geometrical shapes (sphere and cube) is created in MATLAB in black and white;
- Radon transform is applied on this image using the Radon function found in MATLAB;
- Implement the sinogram resulting from the Radon Transform into the probability matrix function (without collimator) and then in the MLEM function established in the C++ code.

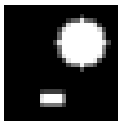
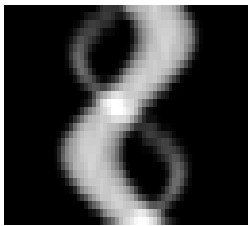
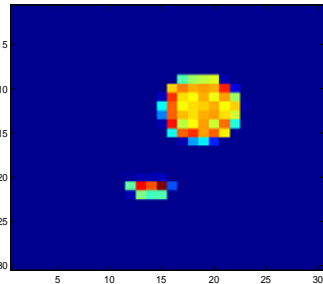
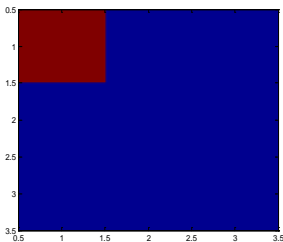
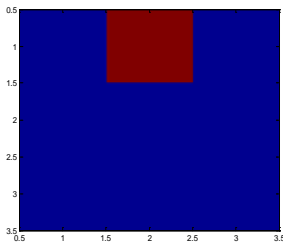
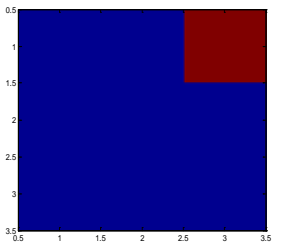
Original Sample created in MATLAB	Sinogram done in MATLAB	Reconstructed Image in C++
		

Figure 5.11: Validation of probability matrix and MLEM algorithm

The second step concerns the reconstruction of the images from fluorescence data. Fluorescence measurements are done with the setup described in previous chapter. The tomography is performed on a lead sample immersed in water. Every time the Lead element in the original sample has a different location then the reconstructed images reflect exactly the spatial distribution of the sample (see Figure 5.12).

Sample	voxel8: Pb	voxel5: H2O	voxel2: H2O	voxel8: H2O	voxel5: Pb	voxel2: H2O	voxel8: H2O	voxel5: H2O	voxel2: Pb
	voxel7: H2O	voxel4: H2O	voxel1: H2O	voxel7: H2O	voxel4: H2O	voxel1: H2O	voxel7: H2O	voxel4: H2O	voxel1: H2O
	voxel6: H2O	voxel3: H2O	voxel0: H2O	voxel6: H2O	voxel3: H2O	voxel0: H2O	voxel6: H2O	voxel3: H2O	voxel0: H2O
Reconstructed Image									

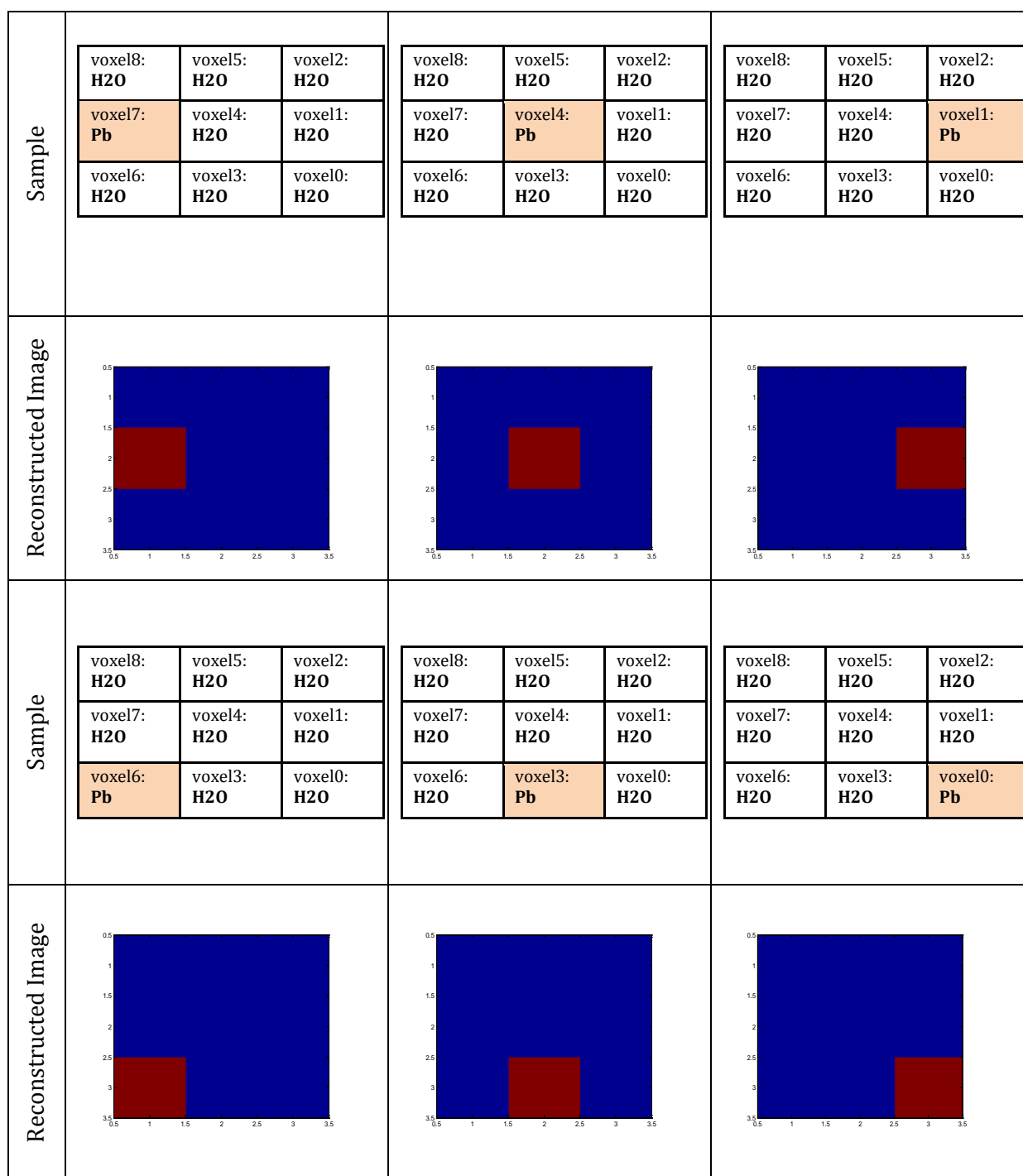


Figure 5.12: Reconstructed images reflecting the spatial localization of fluorescence object.

Other measurements performed on different element types are reconstructed also by applying the MLEM algorithm. The results below distinguish clearly between high atomic number elements and low ones. The spectrum displayed in previous simulation shows higher fluorescence with increased atomic number. What is determined here in the results of reconstructed image is that the intensity of high atomic number reflects high emission of fluorescence. In Figure 5.13, the Lead and Germanium are well discriminated (red and orange color) while the Titanium and Aluminum are not well distinguished from the medium (blue and light blue color).

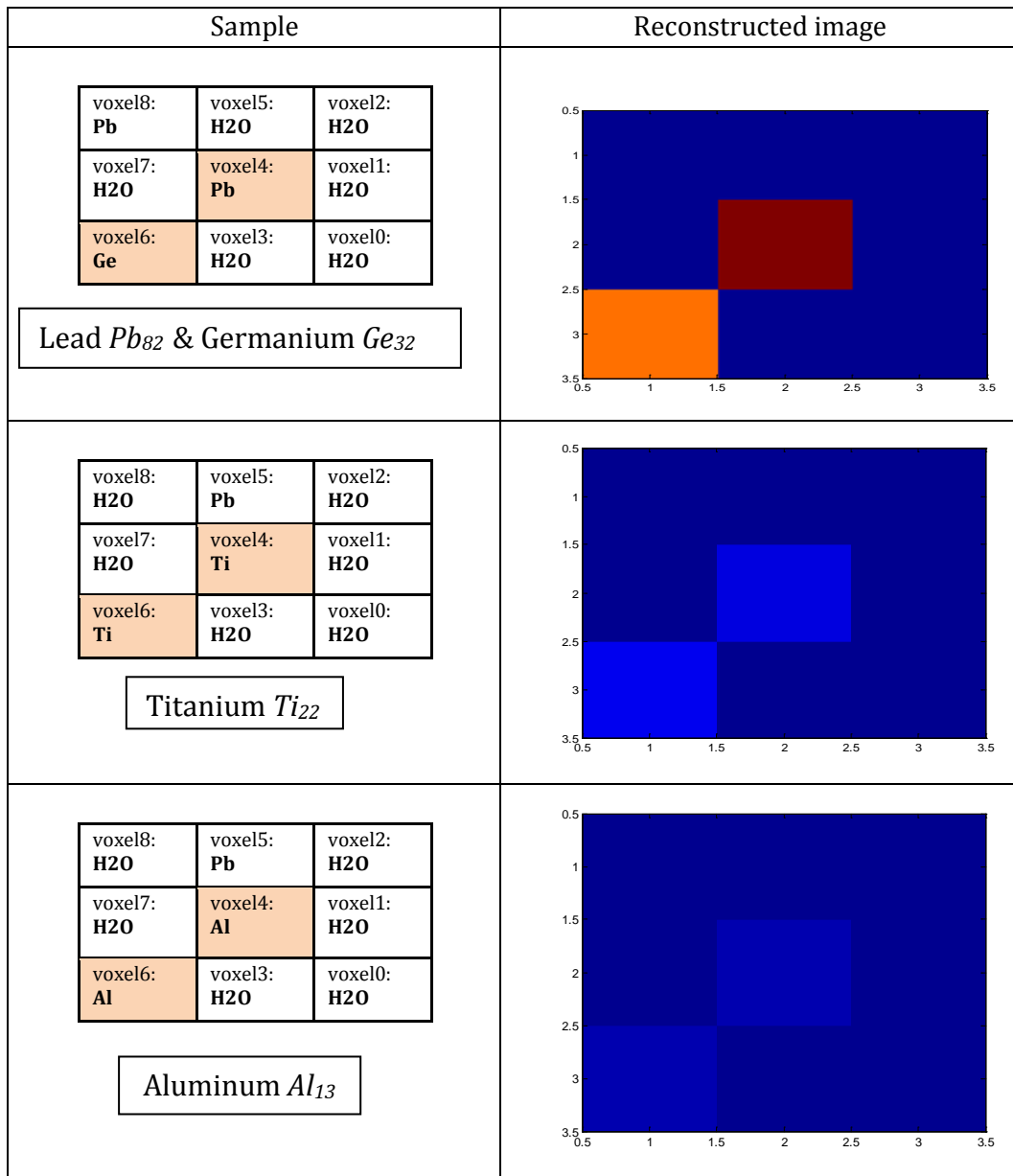


Figure 5.13: Reconstructed images based on same settings for a variety of elements.

5.2.6 Parameter impact study

a) Number of projections

During optimization, tests show that the image quality is proportional to projections. This is shown in the results of Figure 5.14.

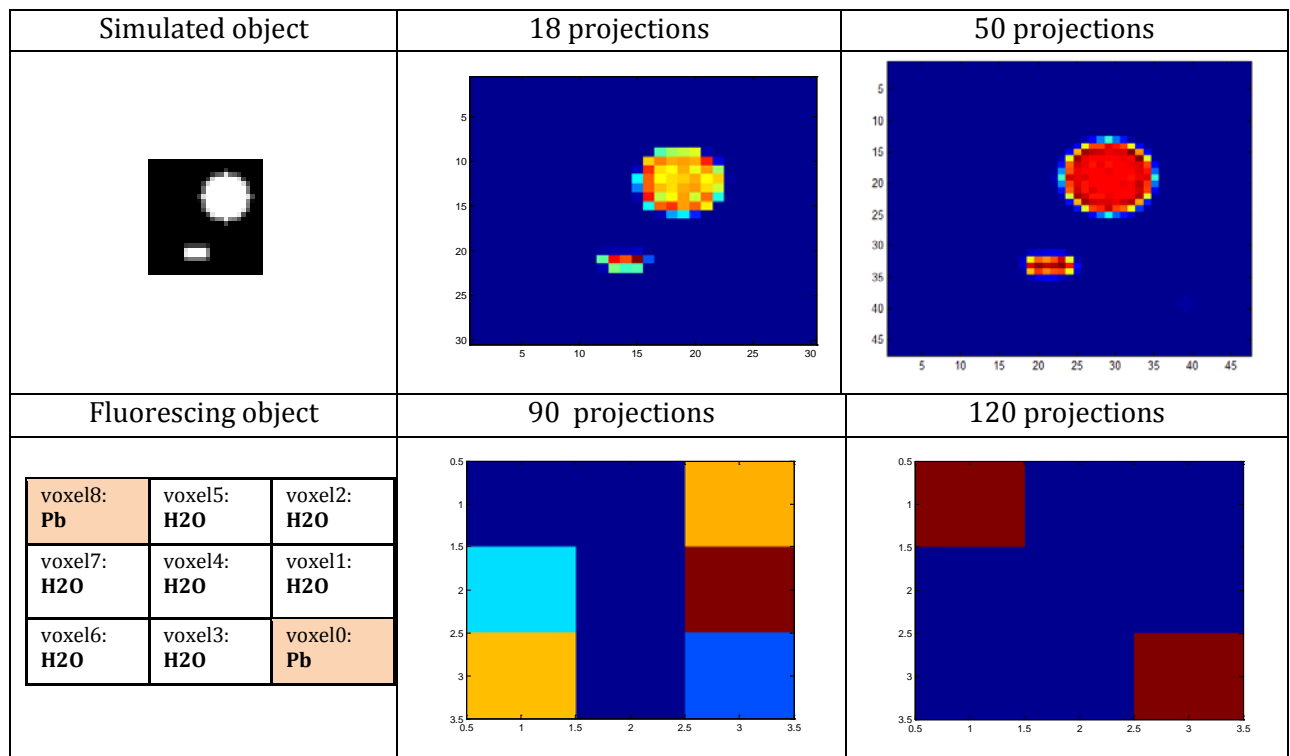


Figure 5.14: Results according to number of projections.

b) Number of iterations

There is a limit for the number of iterations. This is done under testing. For simulated image, 10 to 15 iterations complete the reconstruction process; whereas for the fluorescence data, higher number of iterations is needed (see Figure 5.15).

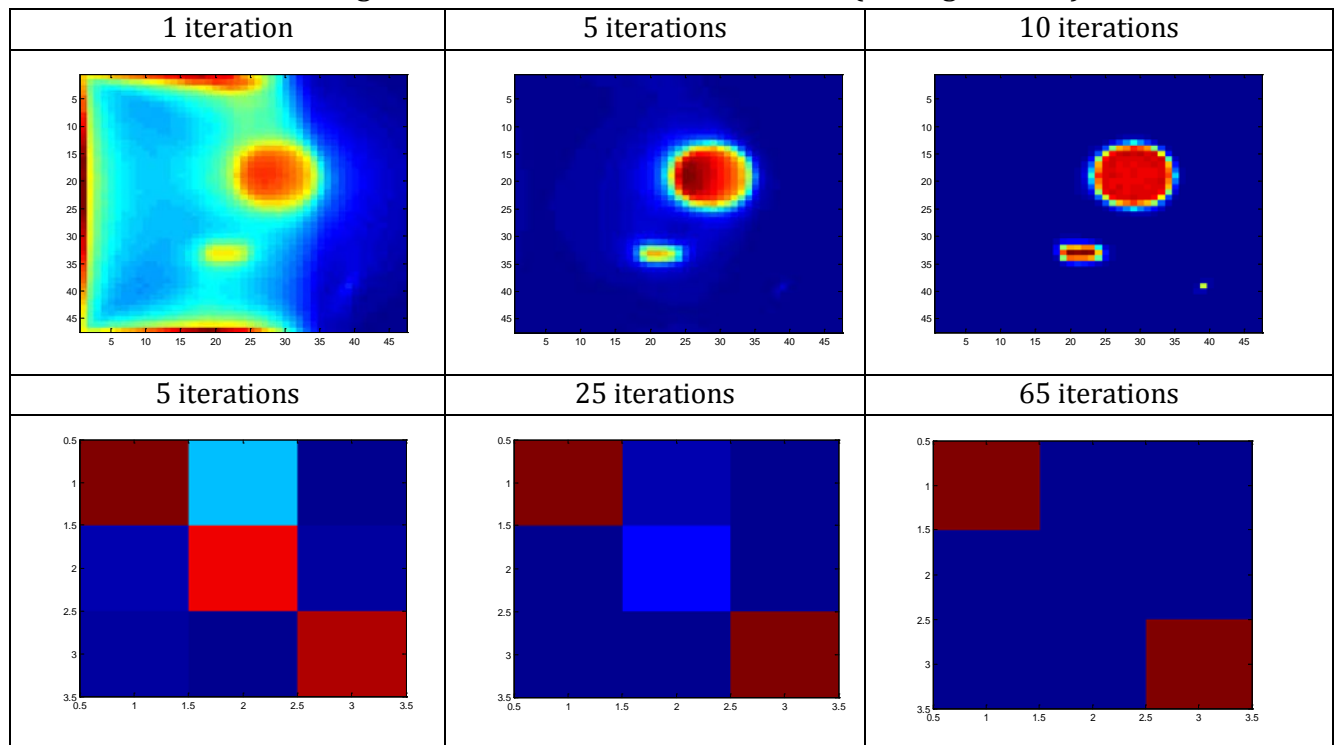


Figure 5.15: Results according to number of iterations.

c) Resolution

The spatial resolution is the capability to distinguish objects close to each other. In order to test the MLEM algorithm on fluorescence objects that are close to each other inside a sample, the following test is done. The algorithm is applied on three images. The first one is a white square inside a black square (Figure 5.16(a)). In the second image (Figure 5.16(b)), the sides of the white square moved closer to each other then they will be closer to the center. The third image contains squares close to each other (Figure 5.16 (c)). The aim is to control how the MLEM algorithm and the applied settings show the center of the square.

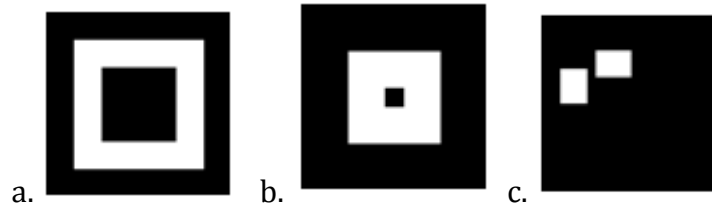


Figure 5.16: (a) White wide box inside a black box; (b) White narrow box inside a black box; (c) Close objects.

The corresponding sinograms are shown in figure 5.17.

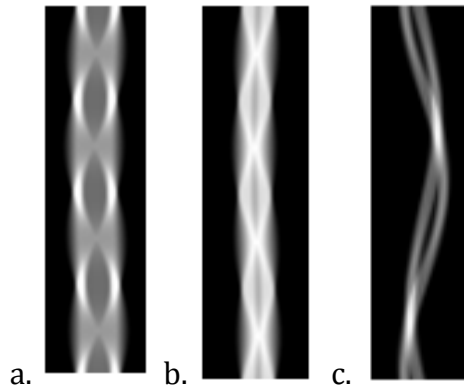


Figure 5.17: (a) Sinogram of a white wide box; (b) Sinogram of a white narrow box; (c) Sinogram of close objects.

Figure 5.18 is the image reconstruction of these boxes. It is the result of 120 projections and 65 iterations of MLEM. The transition matrix dimensions are of “33 *detector pixels* \times 120 *projections*” for the rows and “33 \times 33 as *number of pixels*” for the columns.

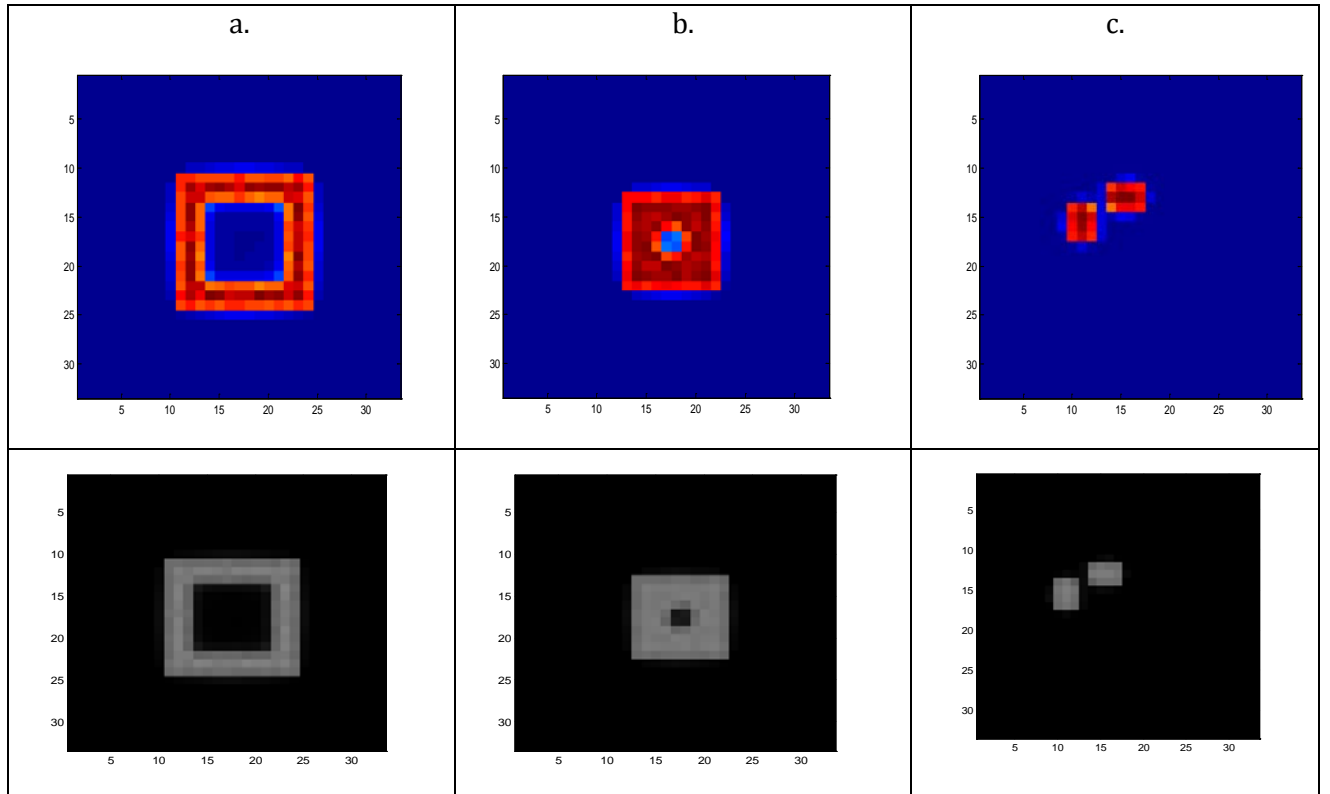


Figure 5.18: Reconstructed images through MLEM algorithm.

Increasing image resolution requires different set-up arrangements during data acquisition. Few samples are shown in Figure 5.19. The images displayed more than one object with high atomic number.

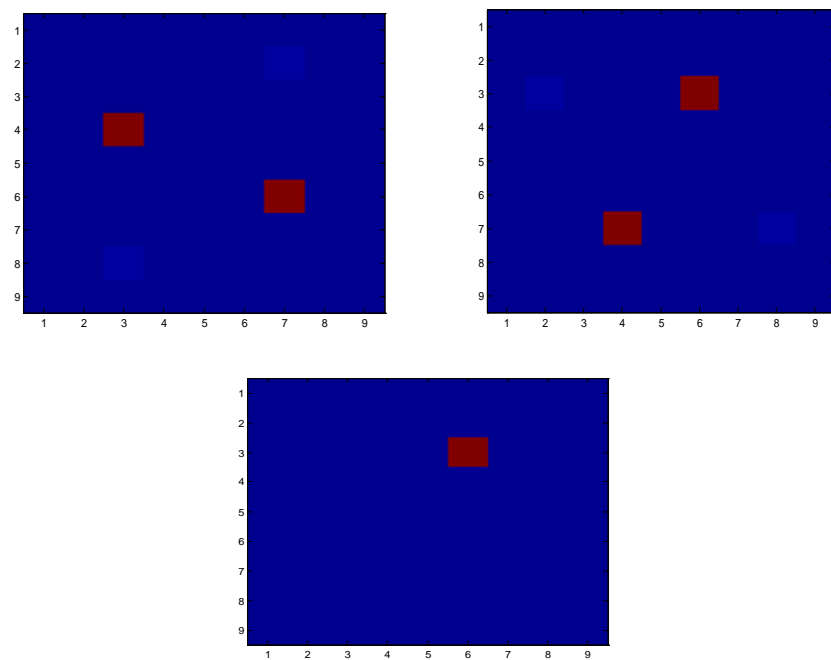


Figure 5.19: Reconstructed images of sample containing Lead elements with high resolution.

The recorded spectrum for two objects is well employed in the MLEM. Well, a sample containing many objects (3 and more) of high atomic numbers lead to a blurred image like the one shown in Figure 5.20. For this reason, a prior is needed to regularize the results. As discussed in the previous chapter, the prior information is the result of FBP algorithm.

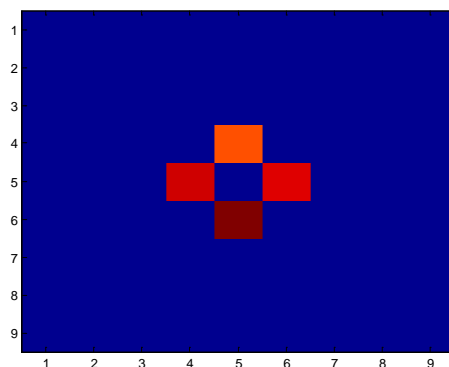


Figure 5.20: Blurred image.

The discontinuity problem due to the presence of high atomic number elements close to each other is solved. The FBP algorithm gives a clear image result for this type of samples. The image obtained from FBP is implemented in the MLEM process. Figure 5.21 represents the regularization technique. Figure 5.22 represents the produced image where the fluorescence activity of high density elements close to each other is well reflected.

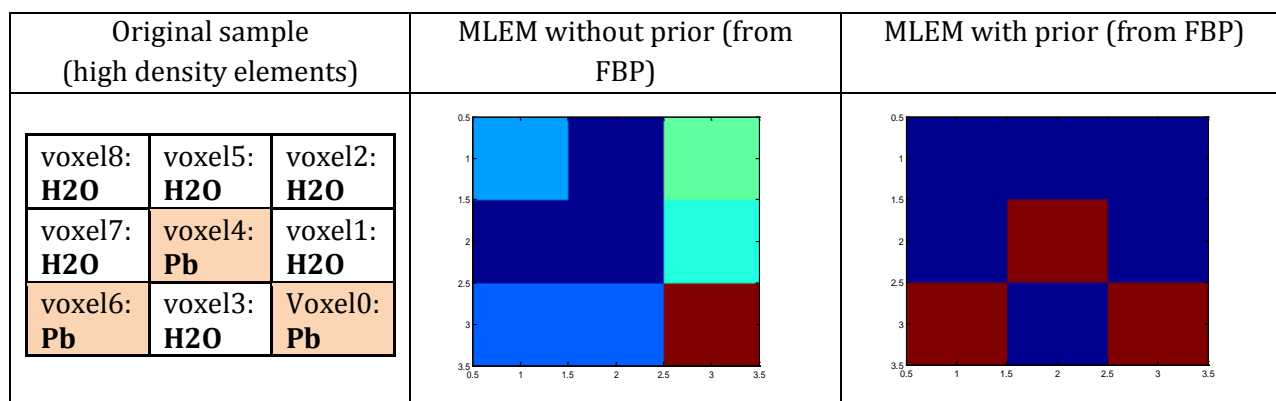


Figure 5.21: MLEM result before and after implementing an image from FBP.

Sample description	Original sample	Sinogram	Reconstructed image									
One object: (type: Lead Pb) immersed in water.	<table><tr><td>voxel8: H2O</td><td>Voxel5: H2O</td><td>voxel2: H2O</td></tr><tr><td>voxel7: H2O</td><td>voxel4: H2O</td><td>voxel1: H2O</td></tr><tr><td>voxel6: H2O</td><td>voxel3: H2O</td><td>voxel0: Pb</td></tr></table>	voxel8: H2O	Voxel5: H2O	voxel2: H2O	voxel7: H2O	voxel4: H2O	voxel1: H2O	voxel6: H2O	voxel3: H2O	voxel0: Pb		
voxel8: H2O	Voxel5: H2O	voxel2: H2O										
voxel7: H2O	voxel4: H2O	voxel1: H2O										
voxel6: H2O	voxel3: H2O	voxel0: Pb										
Two objects: (type: Lead Pb) immersed in water.	<table><tr><td>voxel8: Pb</td><td>voxel5: H2O</td><td>voxel2: H2O</td></tr><tr><td>voxel7: H2O</td><td>voxel4: H2O</td><td>voxel1: H2O</td></tr><tr><td>voxel6: H2O</td><td>voxel3: H2O</td><td>voxel0: Pb</td></tr></table>	voxel8: Pb	voxel5: H2O	voxel2: H2O	voxel7: H2O	voxel4: H2O	voxel1: H2O	voxel6: H2O	voxel3: H2O	voxel0: Pb		
voxel8: Pb	voxel5: H2O	voxel2: H2O										
voxel7: H2O	voxel4: H2O	voxel1: H2O										
voxel6: H2O	voxel3: H2O	voxel0: Pb										
Three objects: (type: Lead Pb) immersed in water.	<table><tr><td>voxel8: H2O</td><td>voxel5: H2O</td><td>voxel2: Pb</td></tr><tr><td>voxel7: H2O</td><td>voxel4: Pb</td><td>voxel1: H2O</td></tr><tr><td>voxel6: H2O</td><td>voxel3: H2O</td><td>voxel0: Pb</td></tr></table>	voxel8: H2O	voxel5: H2O	voxel2: Pb	voxel7: H2O	voxel4: Pb	voxel1: H2O	voxel6: H2O	voxel3: H2O	voxel0: Pb		
voxel8: H2O	voxel5: H2O	voxel2: Pb										
voxel7: H2O	voxel4: Pb	voxel1: H2O										
voxel6: H2O	voxel3: H2O	voxel0: Pb										
Three objects: (type: Lead Pb) immersed in water.	<table><tr><td>voxel8: Pb</td><td>voxel5: H2O</td><td>voxel2: H2O</td></tr><tr><td>voxel7: H2O</td><td>voxel4: Pb</td><td>voxel1: H2O</td></tr><tr><td>voxel6: H2O</td><td>voxel3: H2O</td><td>Voxel0: Pb</td></tr></table>	voxel8: Pb	voxel5: H2O	voxel2: H2O	voxel7: H2O	voxel4: Pb	voxel1: H2O	voxel6: H2O	voxel3: H2O	Voxel0: Pb		
voxel8: Pb	voxel5: H2O	voxel2: H2O										
voxel7: H2O	voxel4: Pb	voxel1: H2O										
voxel6: H2O	voxel3: H2O	Voxel0: Pb										

Figure 5.22: Reconstructed image of fluorescent samples obtained from FBP method.

5.2.7 Experimental validation of simulation

a) Elements results

The following results represent the fluorescence peaks (number of photons) of different samples tested under the same settings such as the geometrical position between source and detector and using the same X-ray source parameters such as the working tension. These peaks are detected on each projection angle between 0° and 180° . In figure 5.23, a homogeneous sample of Aluminum recorded close values on all projections and the maximum amplitude is almost 20. For this reason it is considered to have a low emission of fluorescence.

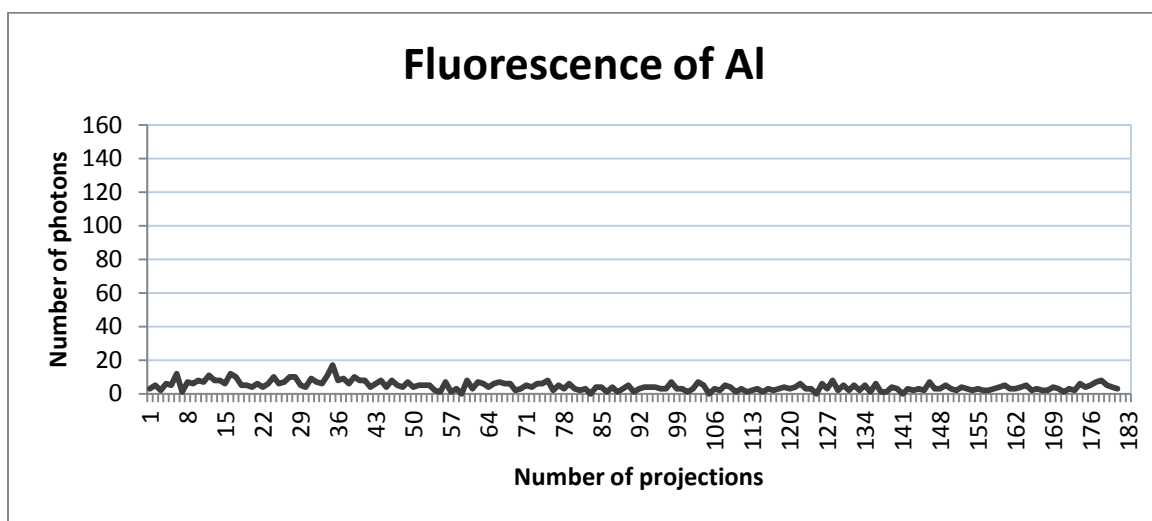


Figure 5.23: Aluminum fluorescence.

In figure 5.24, a homogeneous sample of Lead is tested. The “Lead” peaks recorded higher values of 80 and 100 at different projections. Thus higher peaks are recorded with higher atomic number elements. In addition, it is considered to have high emission of fluorescence.

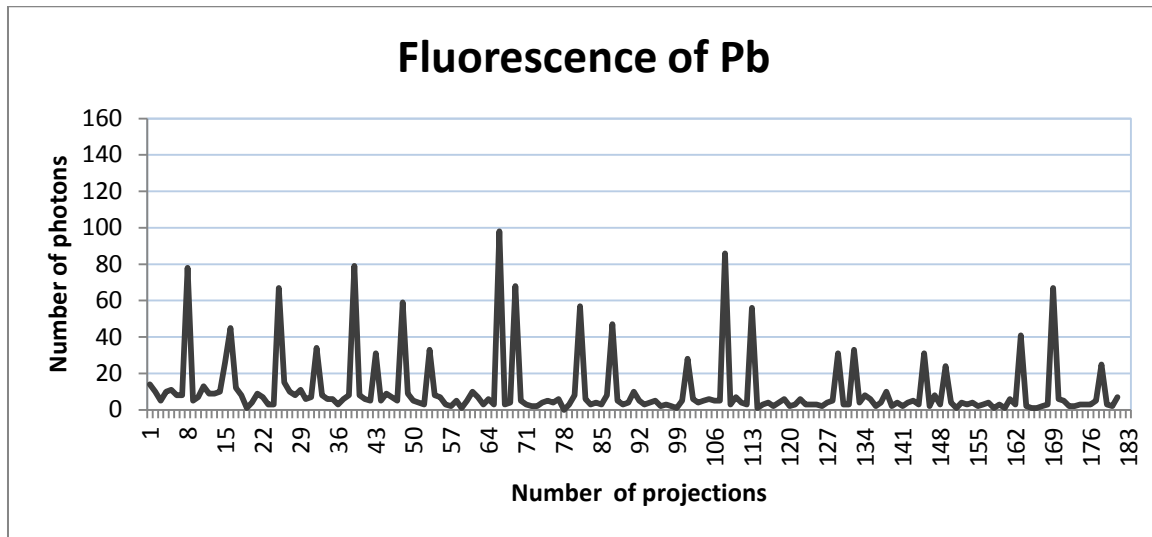


Figure 5.24: Lead fluorescence.

Whereas figure 5.25, represents the result of lead sample immersed in Al. We noticed that the peaks values are increasing to 120 and 140. This proves that for a homogeneous Lead sample, the emitted fluorescence has been attenuated.

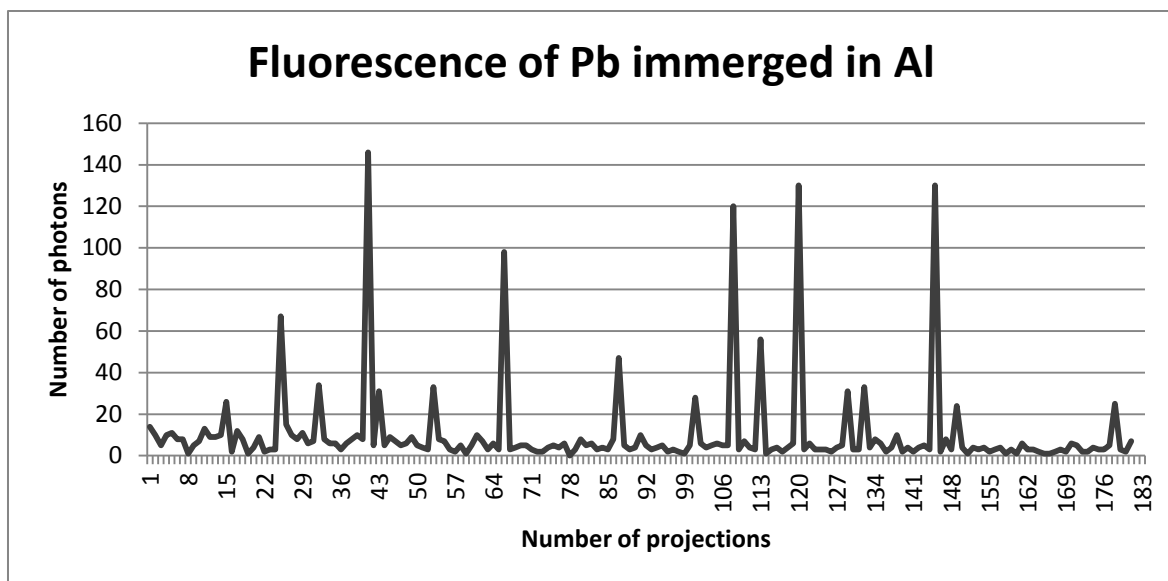


Figure 5.25: Lead immersed in Aluminum.

The “Amber” samples result is addressed in figure 5.26 and 5.27 for ‘Red Amber’ type and a ‘Black amber’ type respectively. The black Amber type is porous and the recorded amplitude peaks reach 40 whereas the red amber type reaches 100. Therefore the black amber showed less fluorescence compared with the red Amber sample.

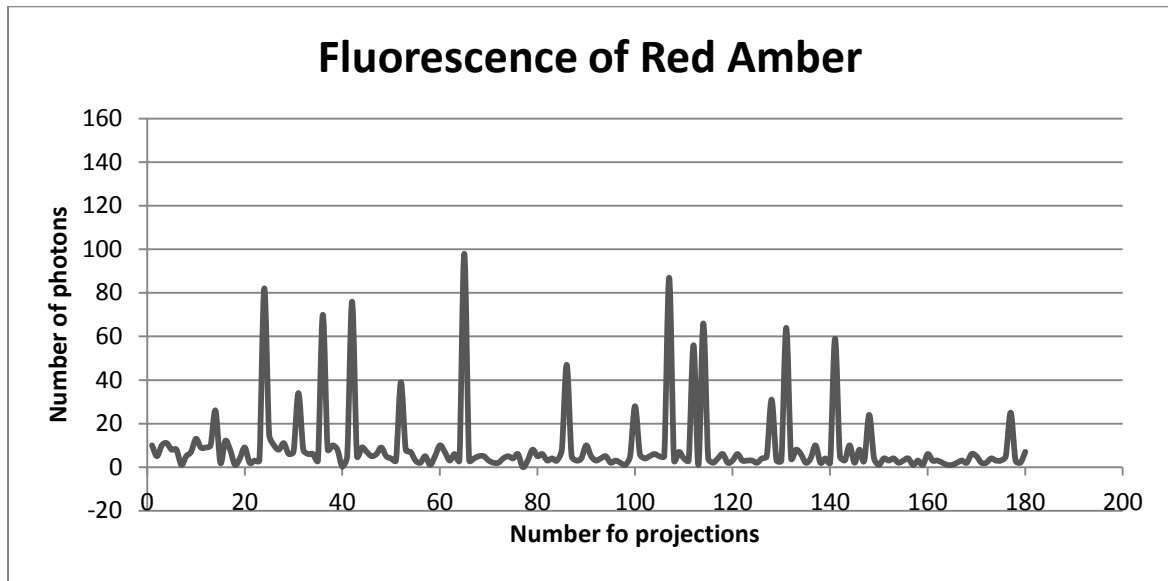


Figure 5.26: Red Amber fluorescence.

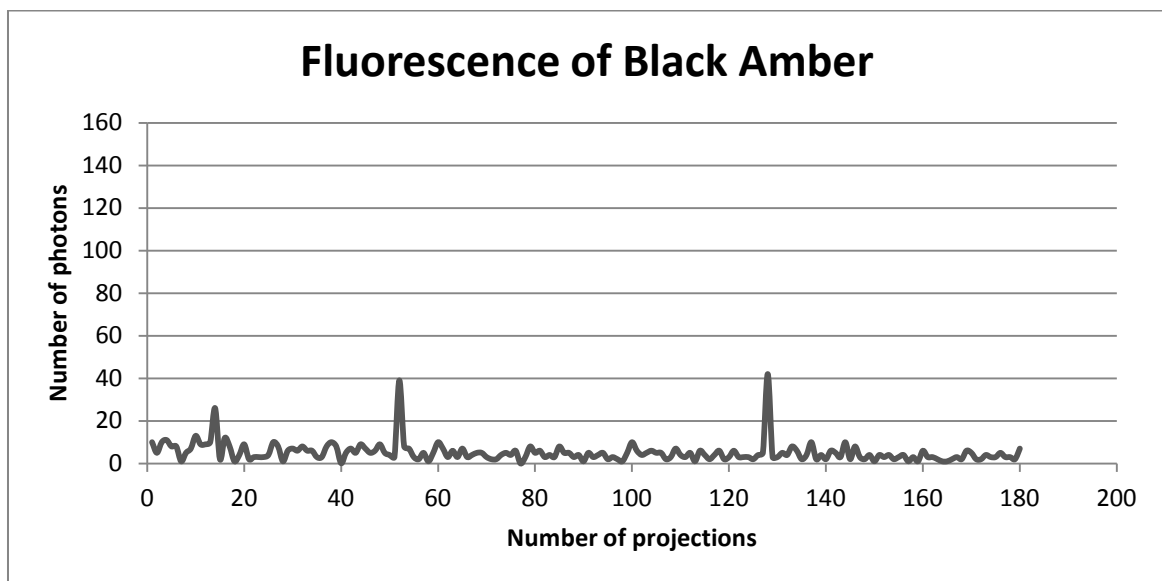


Figure 5.27: Black Amber fluorescence.

b) Comparison between simulation and experimental results

A comparison between the experimental results and simulated result is done on two homogeneous samples of 'Aluminum' and 'Lead'. Results shown in figure 5.28 reveal the simulated fluorescence (blue line) and the experimental emitted fluorescence (red line). The two full spectrums are obtained at the same settings and parameters. The resulting number of photons, for Al at 1.5 keV and Pb at 68.4 keV, represent very close peaks between the simulated and the experiments. For the remaining spectrum values

the resulting number of photons is zero in the simulated result and close to zero in the experimental result. The error is estimated for both elements as follows:

$$e \% = \left| \frac{\text{simulated} - \text{experimental}}{\text{experimental}} \right| \times 100\% = 8 \% \quad (4.13)$$

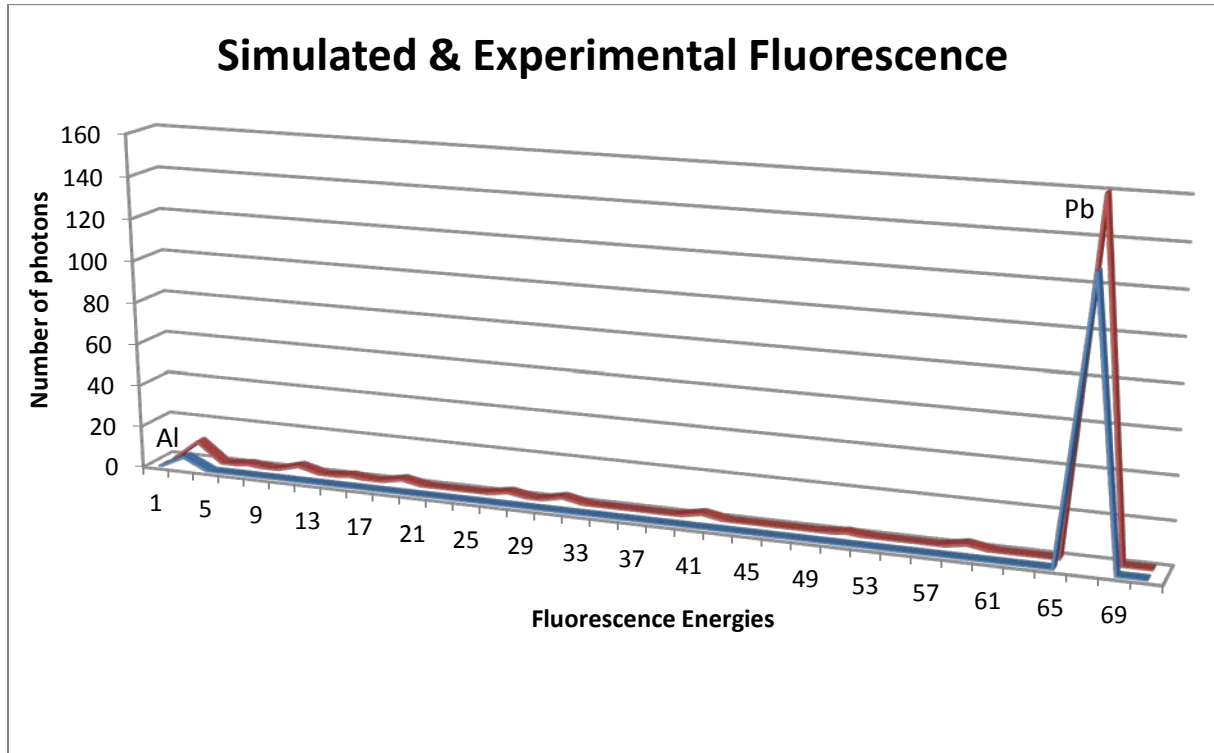


Figure 5.28: Comparison between simulated and experimental fluorescence.

5.3 Experimental Computed Tomography (CT) results

In the following experiment a computed tomography image result is obtained by applying convenient operating settings with the FBP as an image reconstruction algorithm. The test sample contains elements such as rectangular piece of Gold (*Au*), bullets of iron (*Fe*) with different sizes, cylindrical piece of Aluminum (*Al*) in addition to circular piece of copper (*Cu*).

5.3.1 CT obtained image

Different elements are placed in a sample holder of 6 cm diameter that contains a jelly material. The obtained image, shown in figure 5.29, proves that different elements are localized and that the main features of the sample are well-distinguished.

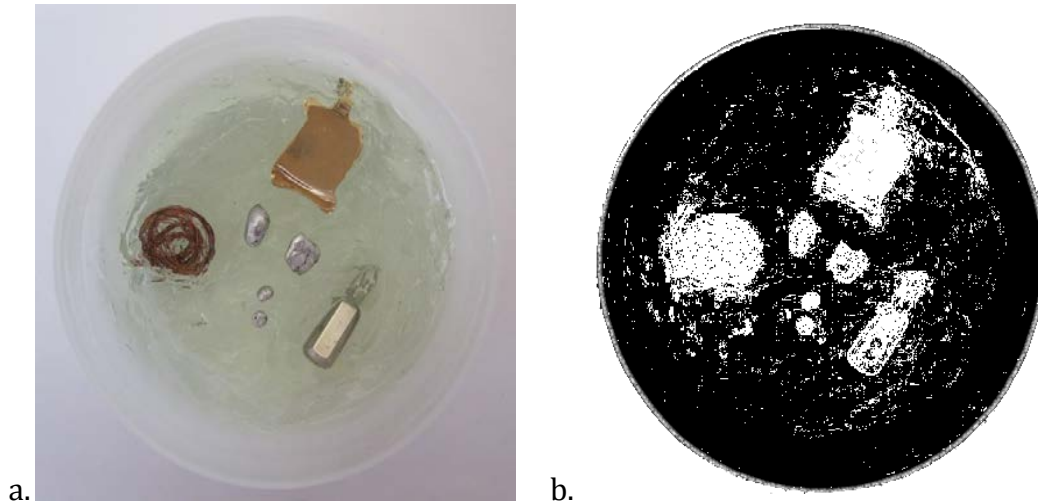
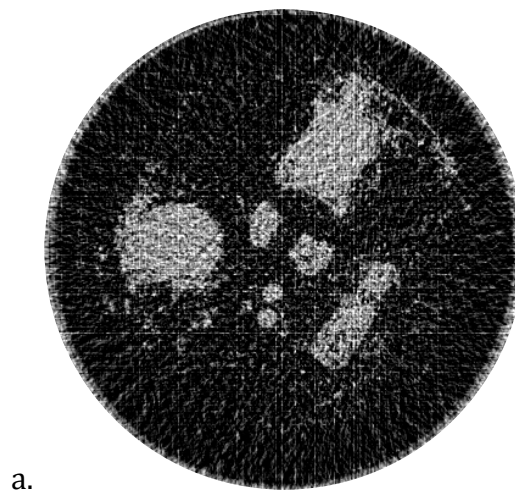


Figure 5.29: (a) Original sample; (b) Computed Tomography image result.

5.3.2 Filtered image

In the simulation part many filters were tested and the Hamming filter was selected to be most convenient in our application. Figure 5.30 shows the image enhancement after filtering. And in Figure 5.30(c) a post-processing filter applied in MATLAB leads to a smoothed image in which the contrast and the brightness have been changed.



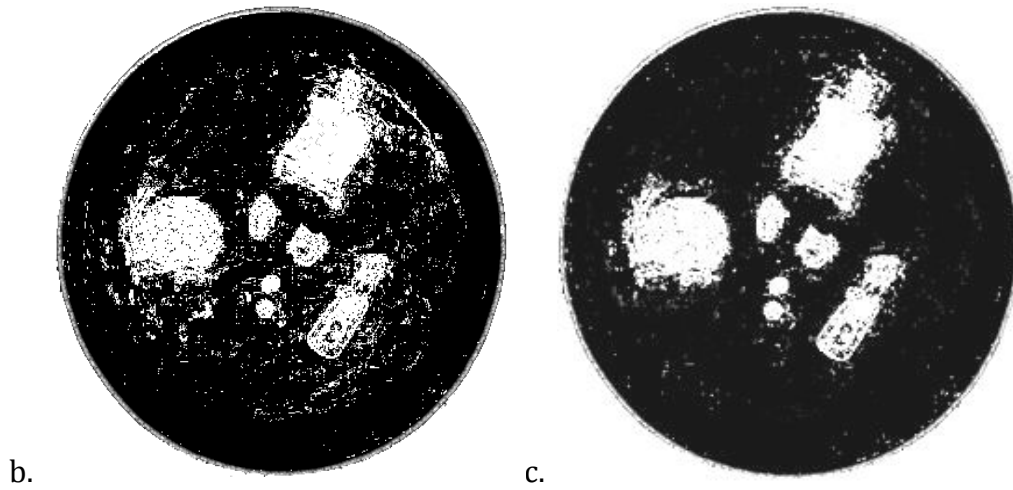


Figure 5.30: (a) Non-filtered image; (b) Filtered Computed Tomography image result; (c) Smoothed image.

5.3.3 Spatial resolution

Figure 5.31 proves that the obtained image has a good resolution. The original sample and the obtained image are overlaid by a grid. Every pixel is a scale of 0.25cm; by comparing the number of pixels covering each element in the 2 images, a small difference can be noticed. Thus, by comparing the elements localization over the 2 grids, an error of 2 % is computed as follows:

$$\text{Error} = \left| \frac{\begin{array}{c} \text{pixels covering each element} \\ \text{in the original image} - \text{pixels covering each element} \\ \text{in the reconstructed image} \end{array}}{\text{pixels covering each element in the original image}} \right| \times 100\%$$

Thus, the system proves an acceptable resolution concerning the distribution of sample elements on the x-y axis of the grid.

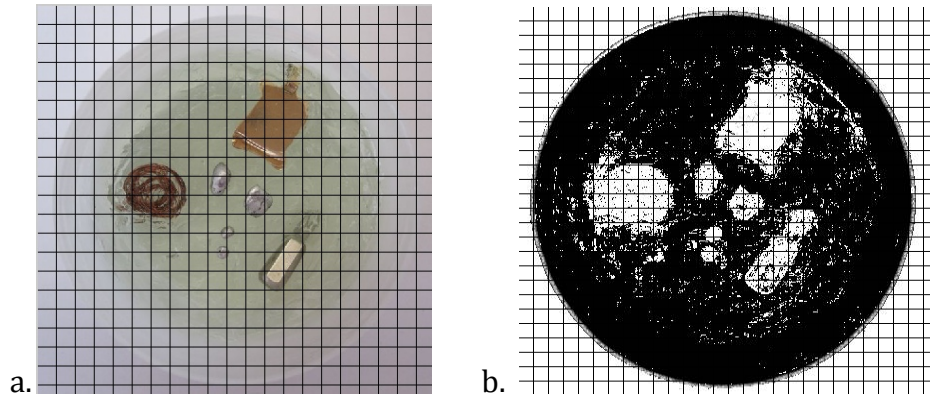


Figure 5.31: A superimposed grid over the original sample (a) and the CT image (b).

In figure 5.32 the distances between the elements is measured in the original sample and the reconstructed image. The distance measurements are close.

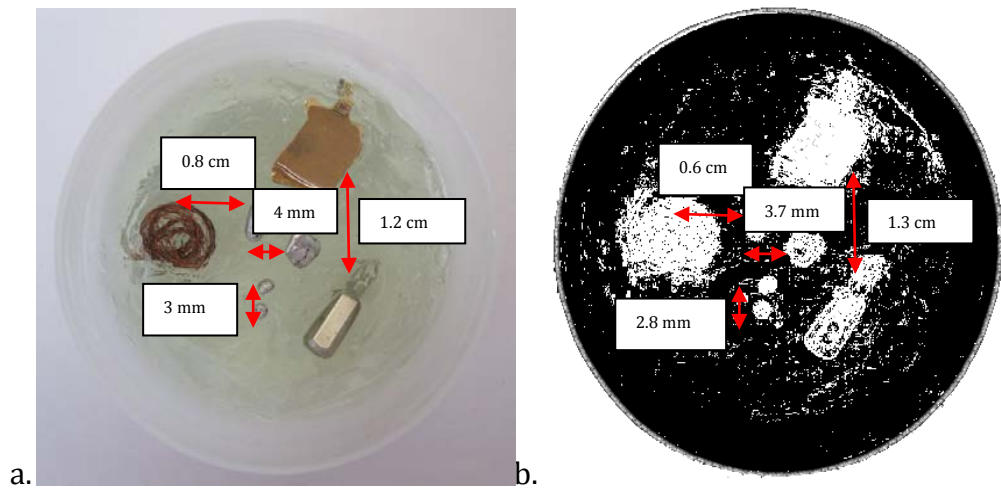
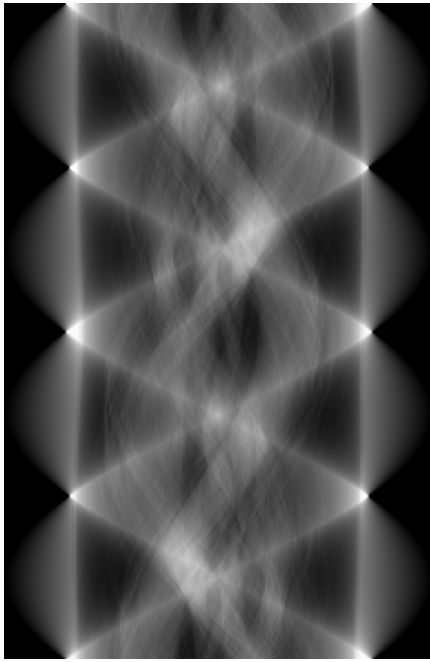
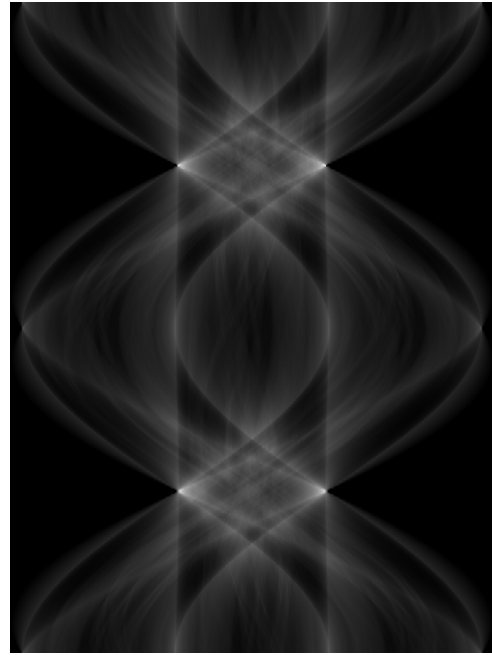


Figure 5.32: Distances between elements in the original sample (a) and the CT image (b).

Figure 5.33 represents the comparison of sinograms between experimental and reconstructed having same number of projections and same number of detector pixels. The reconstructed sinogram from simulation shown in figure 5.33(a) is shown clearer than the sinogram reconstructed from experimental data shown in figure 5.33 (b). The number of objects inside the sample is more reflected and different densities are more obvious.



a.



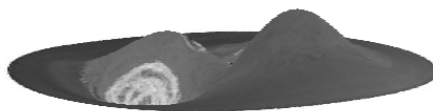
b.

Figure 5.33 : Sinograms comparison between (a) reconstructed and (b) experimental.

5.4 Experimental Fluorescence tomography results

The acquired data from CT image is considered as the input data for an emission tomography. The energies, represented in figure 5.34, have a major contribution in sample analysis and identification. Emission of characteristic fluorescence differs from light element like “Aluminum” to heavy metal like “Gold”. Figure 5.34 (a) displays the energy peaks in a cross-sectional view whereas in figure 5.34 (b) the energy peaks are displayed according to their spatial distribution. The Aluminum and Iron reaches a maximum amplitude of 180 whereas the Copper 210 and the Gold 230.

Once the fluorescence peaks are obtained, the image reconstruction is performed using MLEM with a prior from the FBP. The obtained image in figure 5.35 reveals well-discriminated elements and the different colors yield to element identification.



a.

b. Fluorescence energies re-scaled as per reconstructed pixel

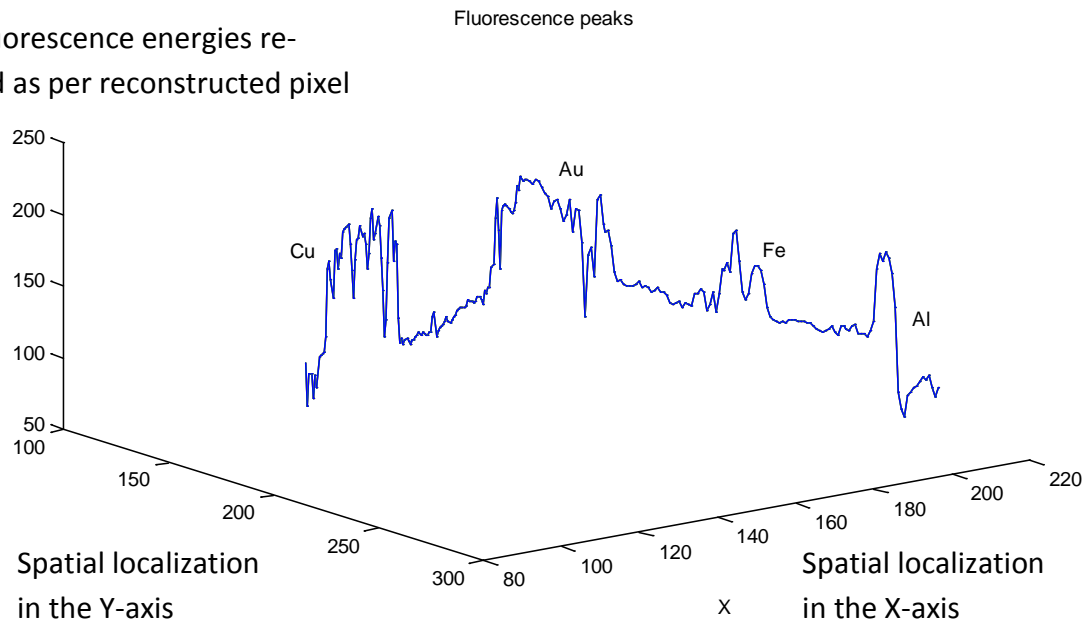


Figure 5.34: Energy peaks.

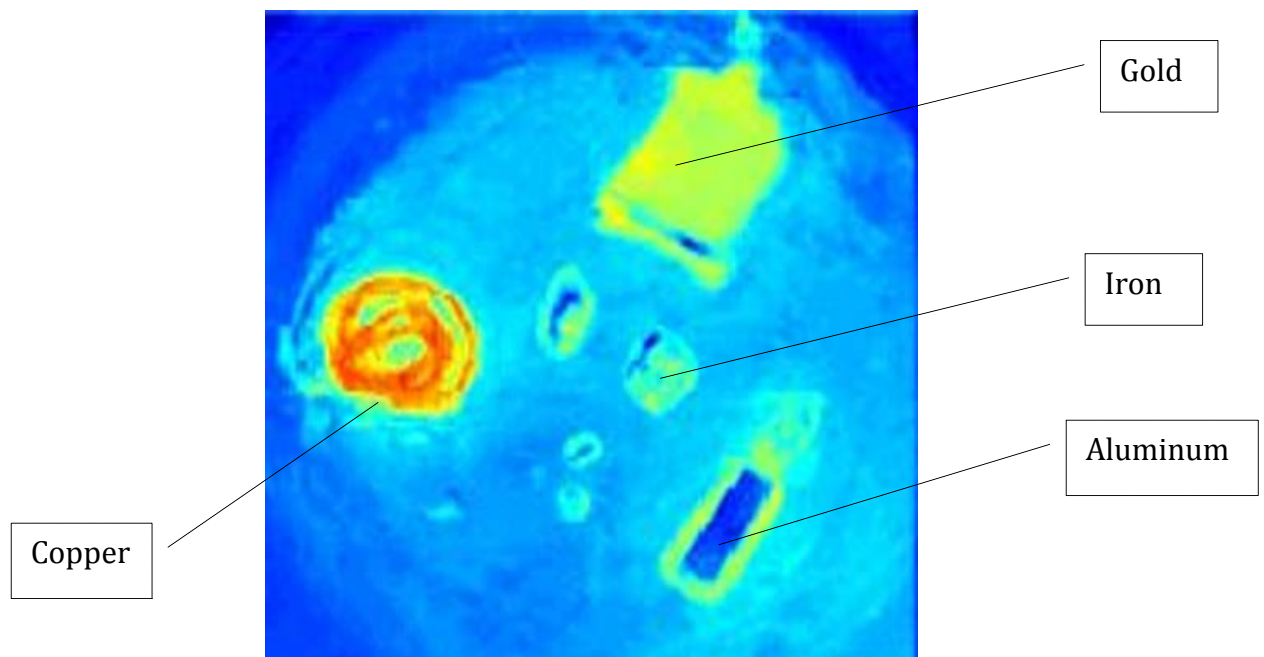


Figure 5.35: Emission tomography image result.

The resulting emission tomography image (shown in figure 5.35) has the following properties:

- RGB (Red; Green; Blue) image;

- Pixels Number [400 × 400];
- At the copper level:
Pixel position is at (91, 229);
Pixel color value is: [Red: 255; Green: 131; Blue: 26]
- At the Gold level:
Pixel position is at (260, 100);
Pixel color value is: [Red: 183; Green: 255; Blue: 65]
- At the Aluminum level:
Pixel position is at (301, 303);
Pixel color value is: [Red: 0; Green: 108; Blue: 226]
- At the Iron level:
Pixel position is at (236, 208)
Pixel color value is: [Red: 18; Green: 135; Blue: 246].

5.4.1 Spatial resolution

In figure 5.36, the red curve is the ideal profile of a vertical line in the image. The black curves have the same profile in the reconstructed image. Thus for a distance of 2.8 mm the separation between objects is possible.

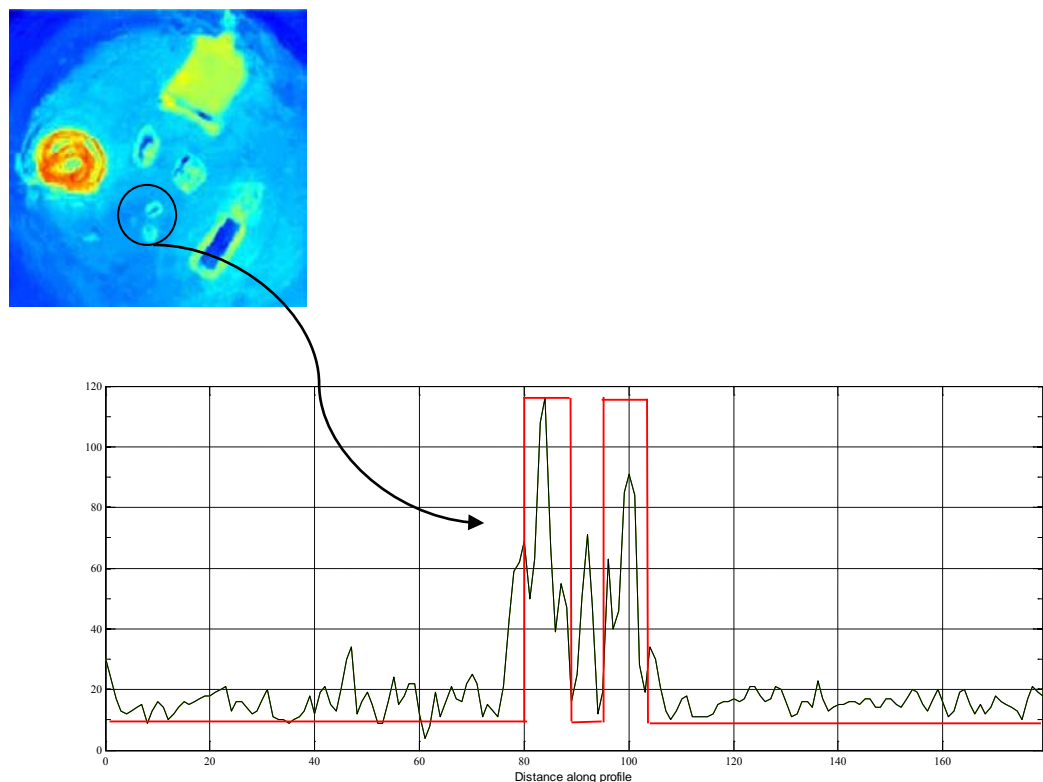


Figure 5.36: The registered values along the distance.

5.4.2 Influence of iterations' number

The elements of the resulting image are discriminated when the convenient number of iterations has been applied in the MLEM reconstruction algorithm. Figure 5.37 shows the resulting image at 50 iterations (figure 5.37(a)) where the 'Iron' is not shown and part of the 'Aluminum' appears. At 100 iterations (figure 5.37 (b)) the edges of Aluminum and Iron elements are revealed. At 150 iterations (figure 5.37(c)), there is no contrast for the 'Iron' elements whereas a good image is obtained at 230 iterations (figure 5.37(d)).

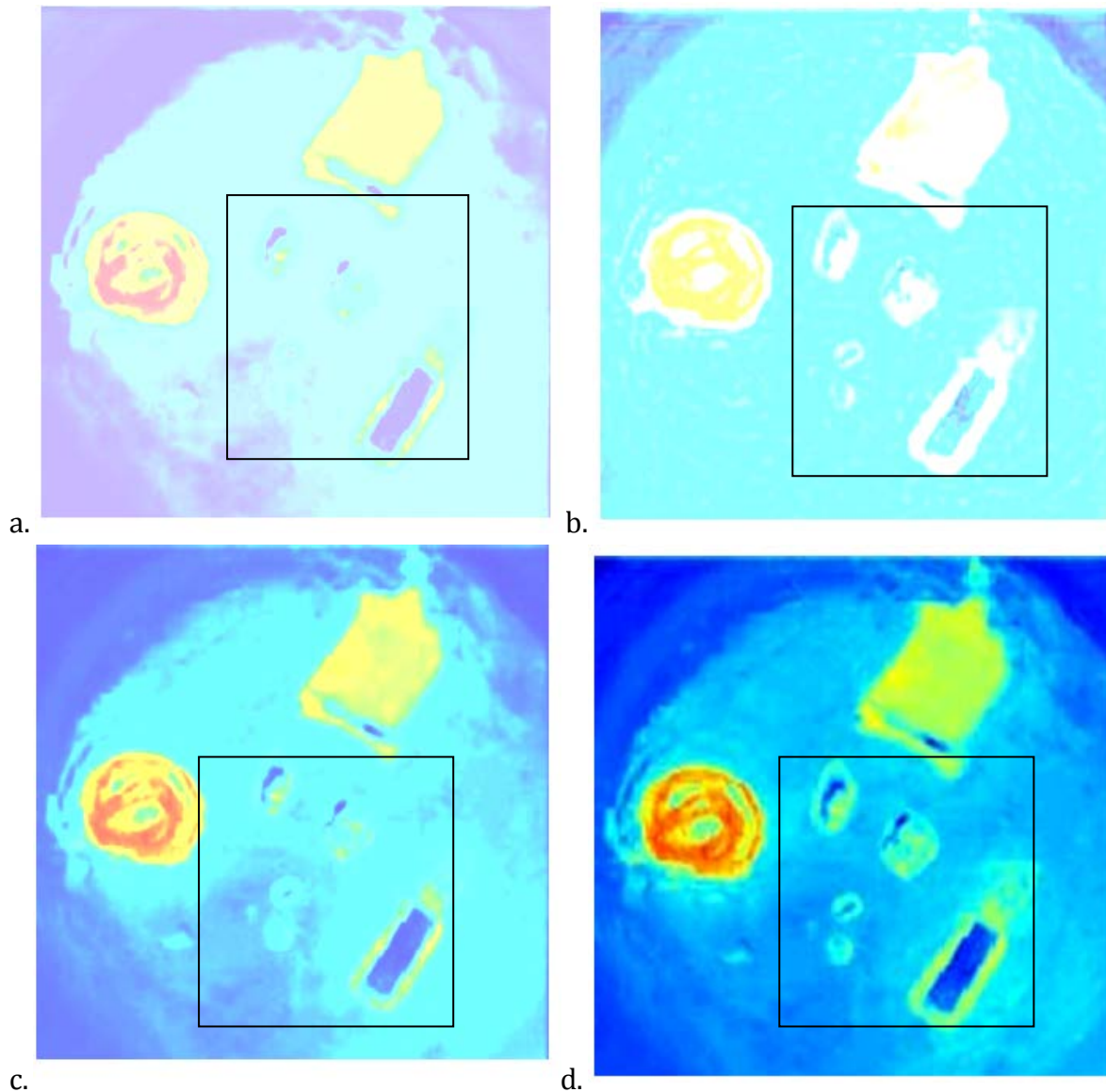


Figure 5.37: MLEM results showing increasing number of iterations.

5.4.3 Emission Tomography spatial resolution

The optimization of the acquisition system enhances the image up to a limit. In order to report the detection limits, an acquisition is done for the same element type but

with different sizes. Samples of Iron (Fe) with different diameters, shown in figure 5.38, are selected and tested. The results of CT and EM are displayed in figures 5.39 to 5.43.

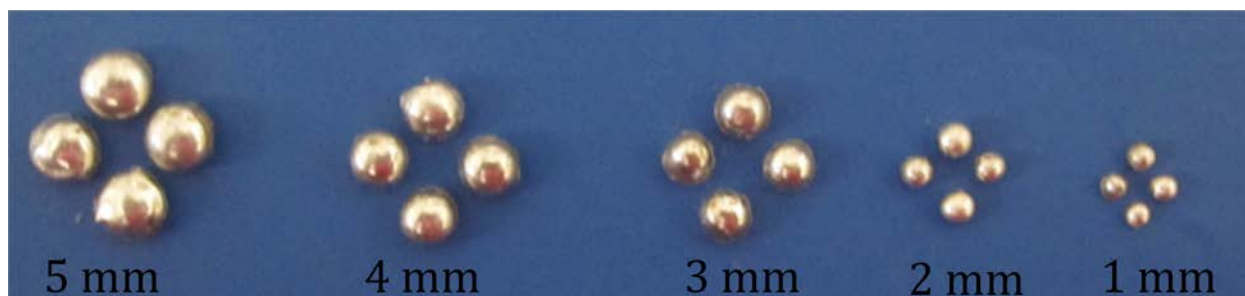


Figure 5.38: Iron material with diameters ranging from 1 to 5 mm.

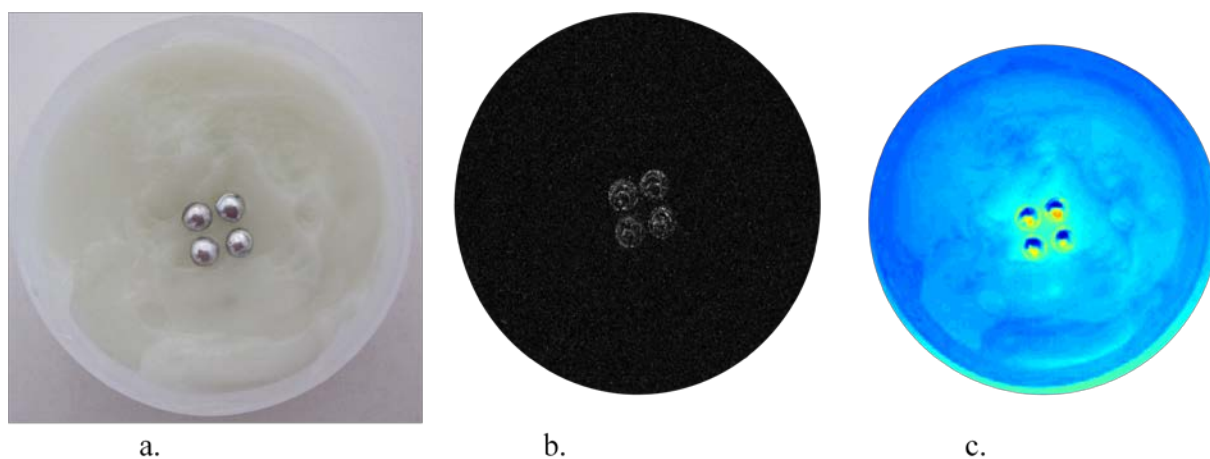


Figure 5.39: Images of 5 mm diameter of Iron material; (a) original sample; (b) CT image; (c) ET image.

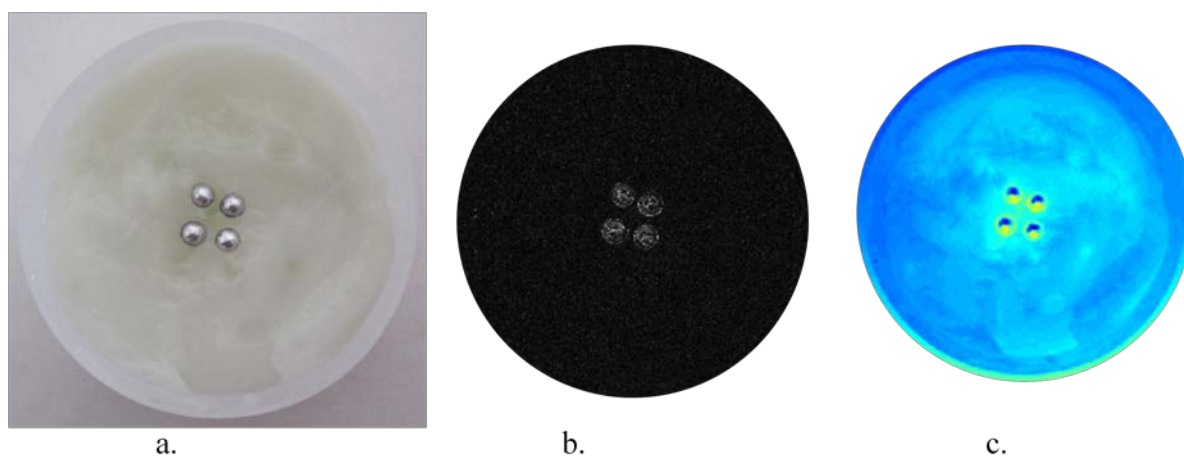


Figure 5.40: Images of 4 mm diameter of Iron material; (a) original sample; (b) CT image; (c) ET image.

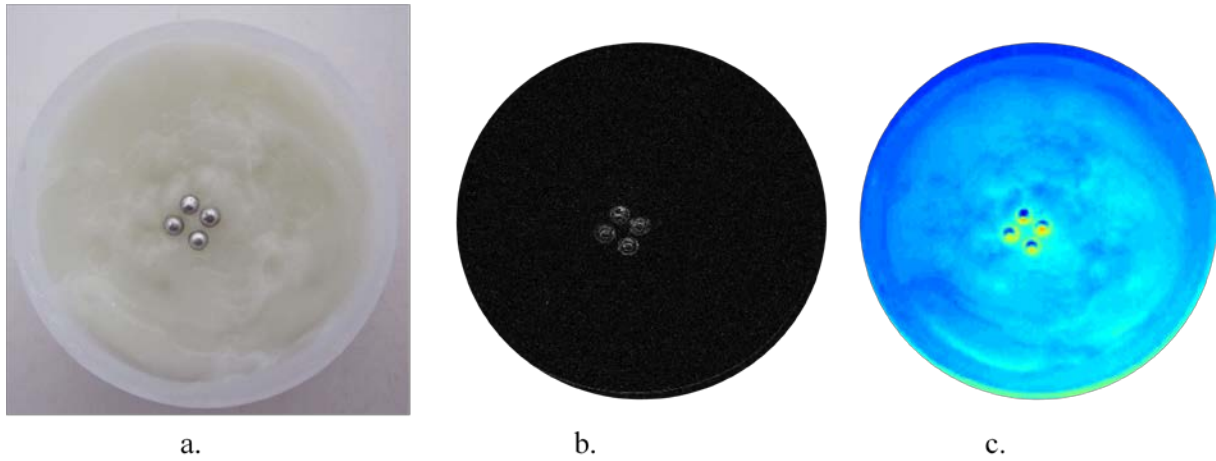


Figure 5.41: Images of 3 mm diameter of Iron material; (a) original sample; (b) CT image; (c) ET image.

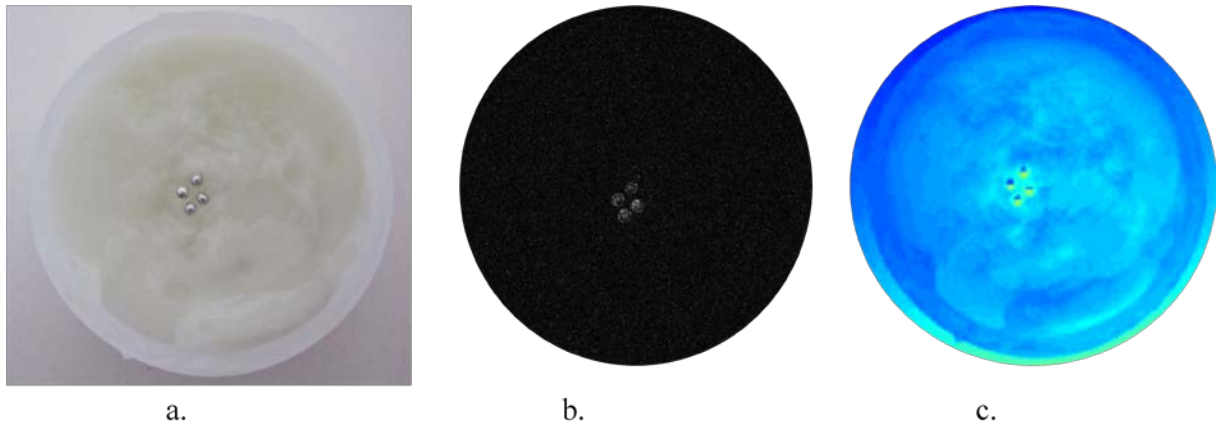


Figure 5.42: Images of 2 mm diameter of Iron material; (a) original sample; (b) CT image; (c) ET image.

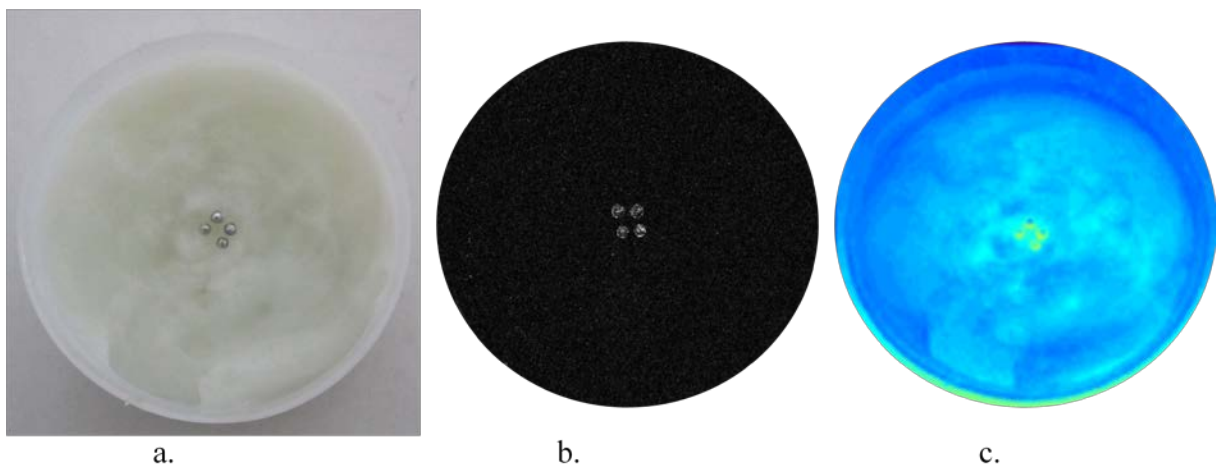


Figure 5.43: Images of 1 mm diameter of Iron material; (a) original sample; (b) CT image; (c) ET image.

The qualitative element identification depends on the emission tomography energy peaks. For this reason, the collected number of photons is compared to provide a valuable analysis. Figures 5.44 to 5.48 represent the response of different diameters samples.

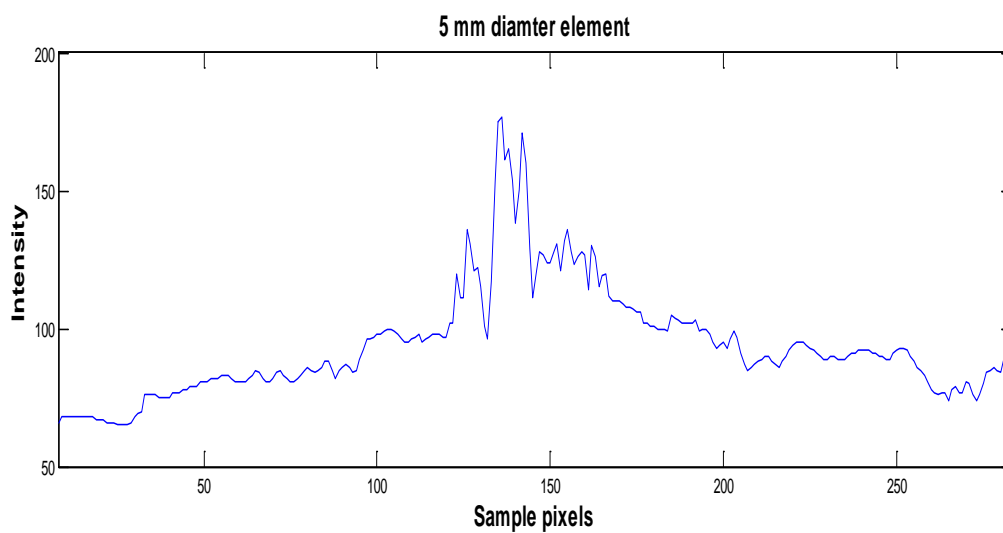


Figure 5.44: Fluorescence emission of 5 mm diameter element.

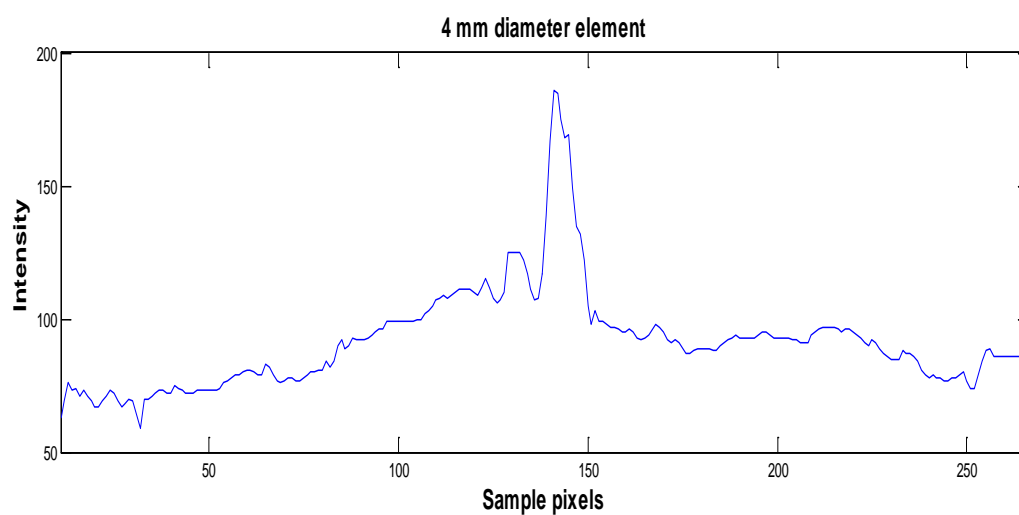


Figure 5.45: Fluorescence emission of 4 mm diameter element.

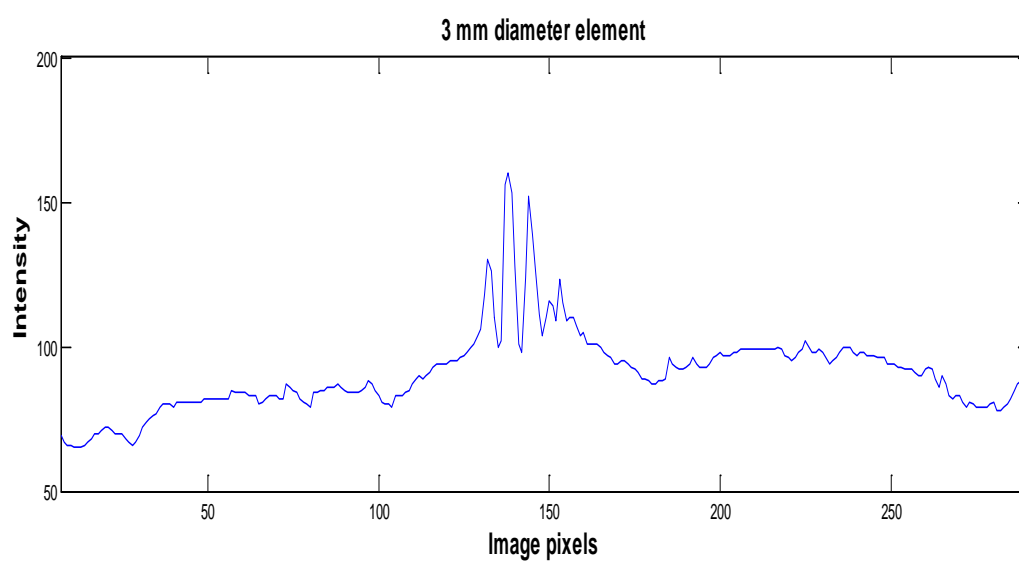


Figure 5.46: Fluorescence emission of 3 mm diameter element.

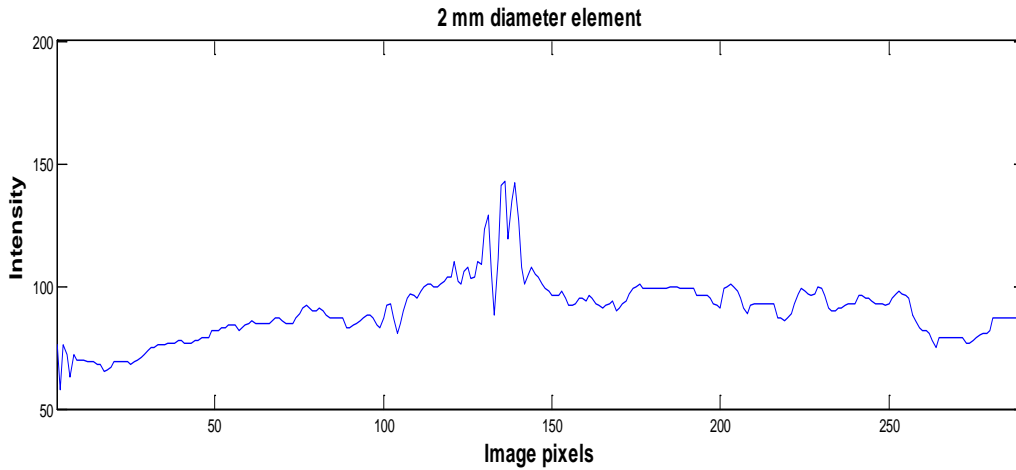


Figure 5.47: Fluorescence emission of 2 mm diameter element.

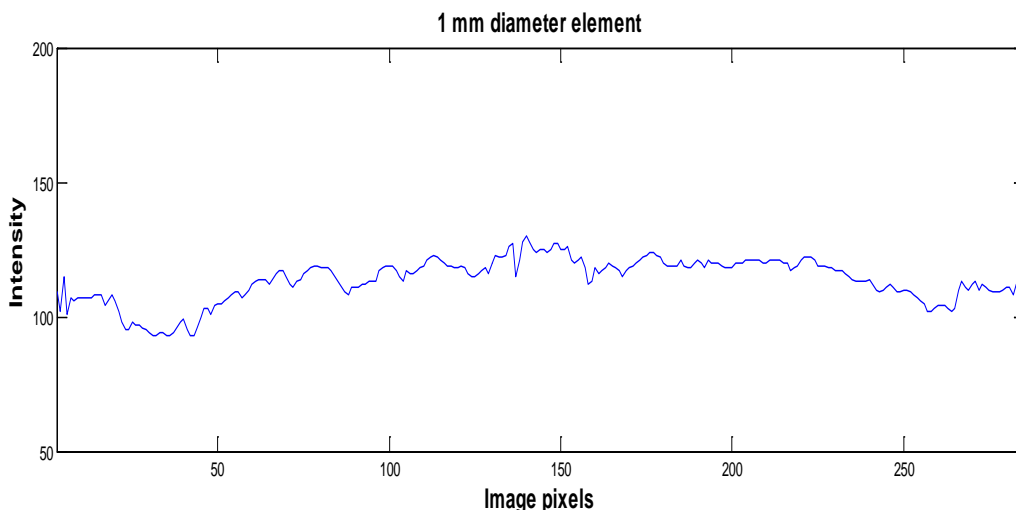


Figure 5.48: Fluorescence emission of 1 mm diameter element.

Sufficient energy has been applied on the different diameters samples. As much as the peak is clear, the element identification is defined. The corresponding values for the peaks are increasing with increased diameter. This is shown in the chart of figure 5.49.

The reported results are necessary to study the system accuracy. The emission tomography images, resulting from the emanated characteristic fluorescence, have high precision response. Starting by a 5 mm diameter up to 2 mm, the obtained images discriminate the sample elements clearly. While for the 1 mm diameter, the obtained “Emission Tomography” image is not well defined. This is revealed in figure 5.43 and 5.48. The current sample situation suggests many optimization settings to be employed. Even though, the results for diameter elements less than 2 mm do not represent a well-defined peak, thus the obtained emission tomography image doesn’t provide a detailed sample analysis.

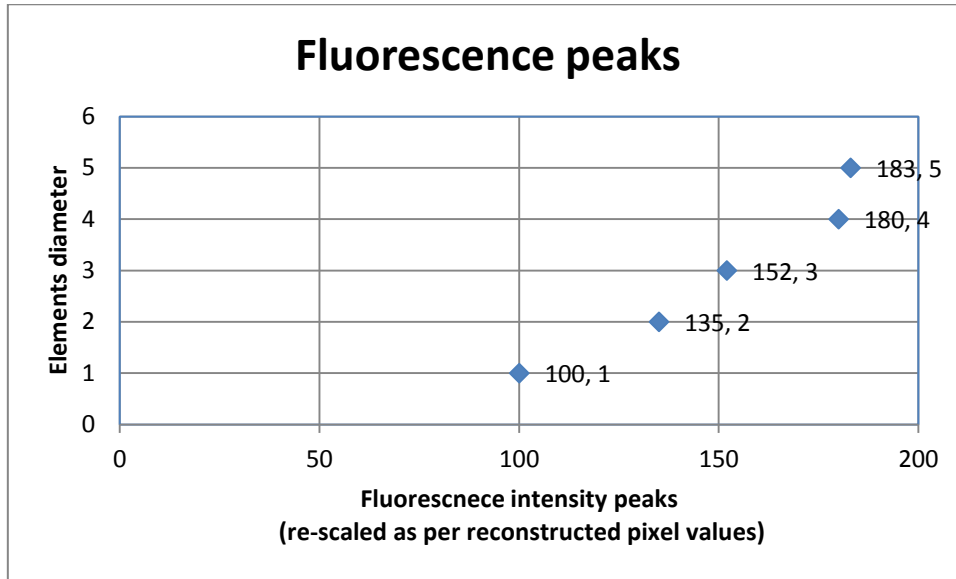


Figure 5.49: Fluorescence peaks at different diameters elements.

The most accurate analysis is performed when the set-up is optimized. For this reason the detection limits must be known and taken into consideration. For instance, the simulation and the experiment prove that the self-absorption, the material size and the material atomic number have a great effect on the detection and consequently on the obtained emission tomography.

5.5 Conclusion

The physical quantity that is measured through experiment is the number of photons emitted along the projection lines. These acquired measurements are compared with simulated results having same settings and parameters. The results are close; which means the system is reliable and the obtained fluorescence data is able to determine a well-defined image. Moreover, from the measurements of the computed tomographic modality, an accurate distribution of a particular physical quantity is estimated in the sample. The obtained energy peaks, representing the emitted fluorescence, determine the sample composition. This identification is performed with an acceptable resolution. Consequently, this experimental part demonstrates the development of the proposed technique towards an accurate analytical study.

As image reconstruction, the obtained results have an acceptable resolution of a spatial distribution. The acquired cross-sectional image is able to locate particles in a solution in a millimetric order due to adapted MLEM algorithm. A good position affinity is shown for particles and elements of low density in a fluid. As for high density elements, the implemented regularization has optimized the result. The prior-data obtained from the FBP reflected the sample with high precision. Thus, when it is incorporated in the reconstruction process, accuracy in the reconstructed image is reached. This proves that the proposed solution realized its objective.

Chapter 6 : Conclusion & perspectives

In this thesis project, the developed technique and method of X-ray fluorescence tomography meet the needs of a non-destructive testing in different applications. Thus the objective of this work was reached. The presented measurement system is a simple technique in which the polychromatic X-ray source shows efficiency in increasing the probability of fluorescence emission. Moreover, before performing the real measurement system itself, an accurate simulation code is carried out and the established algorithm offers an important conception of parameter estimation. These parameters are optimized to scan and derive data from various samples of different shape and size and under different conditions. Another strong point in this measurement system is the consideration of Compton scattering effect. This robust simulation measurement provides complete set of tools for an experimental arrangement and consequently for an image reconstruction technique.

During analysis and inspection of fluorescence peaks reaching the detector, the problem of sample self-absorption is observed. For this reason, more attention is given to the output source voltage settings. Hereafter, the completed quantitative analysis takes into account “the attenuation of the incident X-ray beam” and at the same time “the attenuation of the emitted fluorescence”. As follows, an absorption correction is done. Furthermore, the sample elements fluorescence has low energies. Despite this, the heterogeneity is well reflected in the obtained tomographic sections. However, this part of work was the most critical. First, the image reconstruction technique is adopted based on the information collected from emitted fluorescence. These data are probabilistic and statistical. Consequently, the reconstruction algorithm is achieved using the Poissonian model. To be more realistic, not only the emission of fluorescence is probabilistic but the detection as well. Accordingly, the transfer system matrix between the measured fluorescence values and the updated image is created upon two criteria, the detection probability and the solid angle geometrical factor.

Under these circumstances, the obtained results are reliable and have an acceptable resolution. Although in some cases, while detecting high atomic number elements, prior information is needed. To accomplish this task, an analytical method is

adopted as a transmission method to get a prior image. So, a Bayesian inversion method is used to incorporate the prior information in the iterative statistical method. This is a type of regularization that can also be optimized.

For future perspectives, two approaches can be studied and applied. In the current work, the X-ray fluorescence spectrum in a liquid flow has been well detected. Thus, more effort can be done for setting an experimental set-up to detect X-ray fluorescence spectrum of elements in gaseous medium for instance in gaseous host. Moreover, the developed algorithm in image reconstruction leads to a well determined image in 2-Dimension. Further work in the acquisition procedure and in the image reconstruction part can build a 3-Dimensional image.

The experimental results and the simulation validation prove that our X-ray fluorescence tomography is capable to be a faithful imaging technology.

Annex A

Fourier Transform:

The Fourier theory is used to arrive at a closed form solution.
The Discrete Fourier Transform is given by:

$$F(u) = \frac{1}{N} \sum_{x=0}^{N-1} f(x) e^{-i 2 \pi u x / N} \quad (\text{A.1})$$

for $u = 0, 1, 2, \dots, N - 1$;

The Inverse Discrete Fourier Transform is given by:

$$f(x) = \sum_{u=0}^{N-1} F(u) e^{i 2 \pi u x / N} \quad (\text{A.2})$$

for $u = 0, 1, 2, \dots, N - 1$;

Annex B

Figure B.1 represents the chart of the created simulation code including the creation of all imaging components and physical phenomena [47].

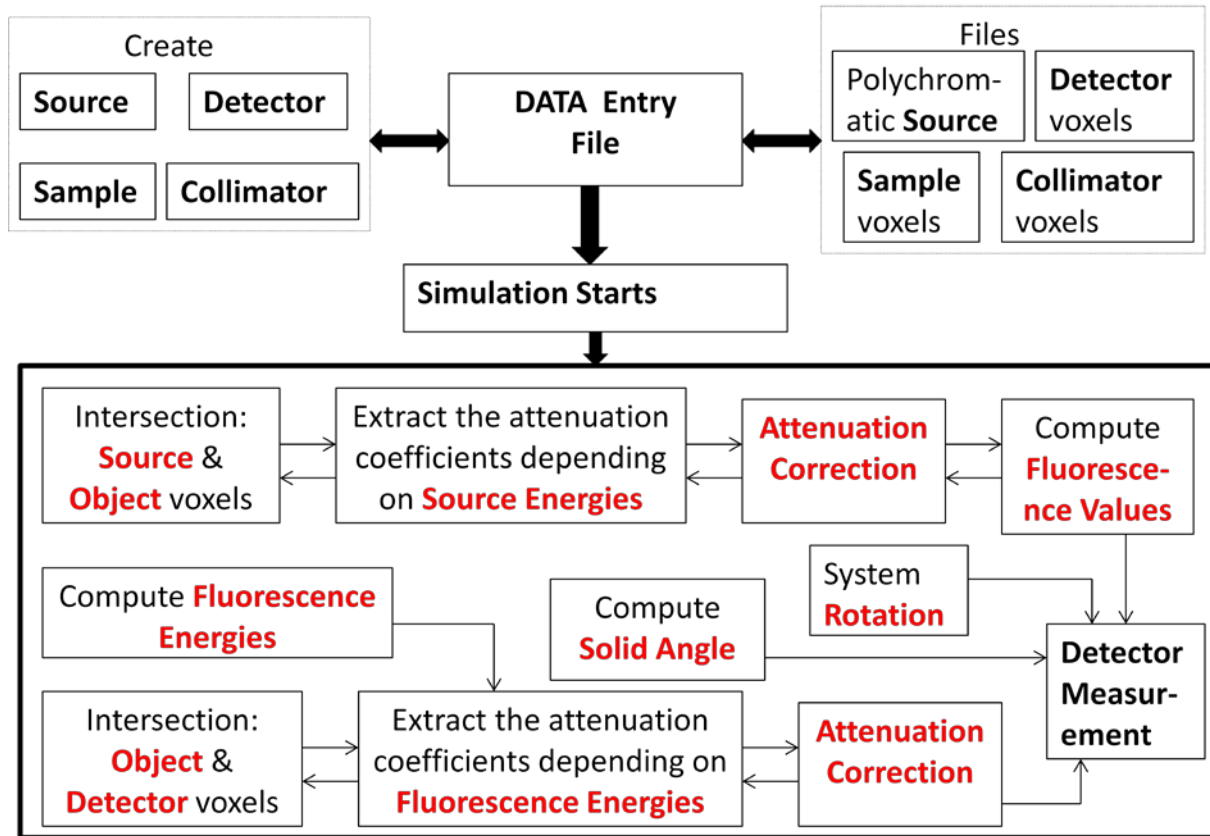


Figure B.1: Simulation code chart.

Annex C

StL format syntax:

Two data formats are included in the StL standard, the binary and the ASCII. The ASCII used in our simulation has the following syntax.

$$\begin{array}{c}
 \textit{solidname} \\
 \left\{ \textit{facetnormal} n_i n_j n_k \right\}^+ \\
 \quad \textit{outerloop} \\
 \quad \textit{vertex} v_1 x v_1 y v_1 z \\
 \quad \textit{vertex} v_2 x v_2 y v_2 z \\
 \quad \textit{vertex} v_3 x v_3 y v_3 z \\
 \quad \textit{endloop} \\
 \quad \textit{endfacet} \\
 \textit{endsolidname}
 \end{array}$$

The notation “{...}+” means repetition of the contents of the brace brackets. The symbols, represented in *italic*, in “facet normal” and in “vertex”, are the numerical values of the variables. Usually these values are floats [46].

Annex D

Intersection Line-Facet:

Based on the simulation code methodology, simulation begins and the intersections between the source and the object as well as the object and the detector are determined.

In order to simulate the intersection of the incident source beam with the sample and the emitted fluorescence rays with the detector and collimator, a mathematical model is used. As the experiment components are of StL format, the mathematical model consists of the intersection of line with a plane that is defined by the facet of the StL object. The procedure is explained in figure D.1 [36].

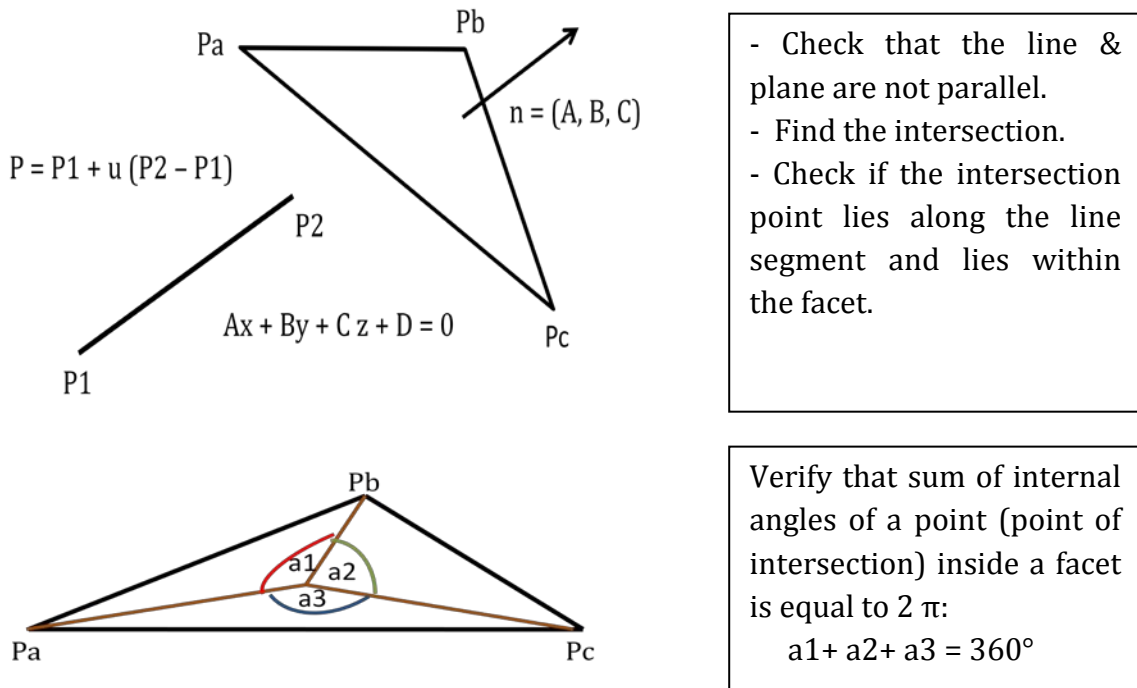


Figure D.1: The mathematical procedure of intersection line-facet.

The intersection process is elaborated not only to find the coordinates of the points of intersection inside the sample. In fact, two basic steps are included:

- Computing the distance between 2 intersection points. This distance is called the linear dimension (see figure D.2).
- Specifying the type of the voxel in which the intersection point lies. This is done in order to extract the attenuation coefficient corresponding to each voxel.

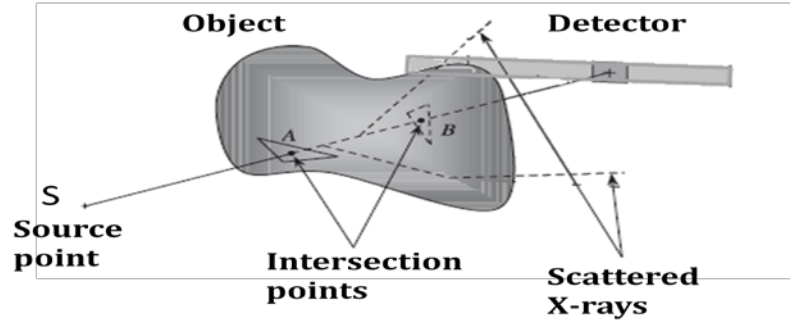


Figure D.2: For each scanning line the distance is computed between 2 intersection points.

Annex E

Probability matrix implementation steps:

The implementation steps are:

- Determine the pixel area:

$$Pixel\ Area = Pixel\ Width^2 = \left(\frac{Total\ Image\ Size}{Number\ of\ the\ Detector\ Pixels} \right)^2; \quad (E.1)$$

- Determine the position of the pixel of interest:

Inside a loop going through all the image pixels, we compute for each pixel the column position and the row position:

$$Pixel\ Column\ position = \left(\frac{Image\ Pixel\ number - 1}{Detector\ Pixels\ number} \right) + 1; \quad (E.2)$$

$$Pixel\ Row\ position = ((Image\ Pixel\ number - 1) \% Image\ Pixel\ number) + 1; \quad (E.3)$$

- Determine the 4 lines that defines each pixel:

$$LEFT = \frac{Total\ Image\ Size \times (Pixel\ Row\ position - 1)}{Number\ of\ the\ Detector\ Pixels} - 1; \quad (E.4)$$

$$RIGHT = LEFT + \frac{Total Image Size}{Number of the Detector Pixels}; \quad (E.5)$$

$$UP = \frac{Total Image Size \times (1 - Pixel Column position)}{Number of the Detector Pixels} + 1; \quad (E.6)$$

$$BOTTOM = UP - \frac{Total Image size}{Number of the Detector Pixels}; \quad (E.7)$$

- Determine the 2 equations of y1 and y2 (shown in figure 4.22) that defines the detection zone of each detector:

$$\begin{aligned} y_1 &= \left(\frac{Nbr of the Detector Pixels}{Total Image Size} - Defined Pixel Nbr of the detector + 1 \right) \\ &\times \frac{Total Image Size}{(Nbr of the Detector Pixels \times \cos(Rotation Step Angle))}; \end{aligned} \quad (E.8)$$

$$\begin{aligned} y_2 &= \left(\frac{Nbr of the Detector Pixels}{Total Image Size} - Defined Pixel Nbr of the detector \right) \\ &\times \frac{Total Image Size}{(Nbr of the Detector Pixels \times \cos(Rotation Step Angle))}; \end{aligned} \quad (E.9)$$

- Define how the scanning lines 'y1' or 'y2' (represented in the following equations by 'y') intersect with the pixel area as shown in figure 4.22:

$$UP_y = \frac{(UP - y)}{\tan(Rotation Step Angle)}; \quad (E.10)$$

$$BOTTOM_y = \frac{(BOTTOM - y)}{\tan(Rotation Step Angle)}; \quad (E.11)$$

$$LEFT_y = \tan(Rotation Step Angle) \times LEFT + y; \quad (E.12)$$

$$RIGHT_y = \tan(Rotation Step Angle) \times RIGHT + y; \quad (E.13)$$

- Check weather lines 'y1' and 'y2' (represented by 'y' in the following equations) intersect the pixel or not:

If (BOTTOM_y < LEFT) then BOTTOM_y = LEFT;

If (BOTTOM_y > RIGHT) then BOTTOM_y = RIGHT;

If (UP_y < LEFT) then UP_y = LEFT;

If (UP_y > RIGHT) then UP_y = RIGHT;

If (UP_y2 <or =LEFT) and (LEFT_y2 >or = UP) or (BOTTOM_y1 >or= RIGHT) and (RIGHT_y1 <or= BOTTOM) then there is no intersection.

- As shown in figure 4.22, when both or one of the lines ('y1' and 'y2') intersect with the pixel i , the common area E is given from the difference:

$$E = E1 - E2; \quad (\text{E.14})$$

where E1 and E2 corresponds to the intersecting lines 'y1' and 'y2', respectively. Thus E1 or E2 is given by:

$$E1 = \left(\frac{\tan(\text{Rotation Step Angle})}{\text{Total Image Size}} \right) \times (UP_y^2 - BOTTOM_y^2) + (y - BOTTOM) \times (UP_y - BOTTOM_y) + \text{Pixel Width} \times (RIGHT - UP_y); \quad (\text{E.15})$$

- Finally, the common area is:

$$E_{\%ij} = \frac{E1 - E2}{\text{Pixel Area}}; \quad (\text{E.16})$$

References

- [1] CESAREO. Roberto, MASCARENHAS. Sergio, **A new tomographic device based on the detection of fluorescent X-rays**, ELSEVIER Nuclear Instruments and Methods in Physics Research A277, November 1989, pp.669-672.
- [2] HOGAN. J.P., GONSALVES. R.A., KRIERGER. A.S., **Fluorescent computer tomography: a model for correction of X-ray absorption**, IEEE Trans. Nucl. Sci.38, 1991, pp.1721-1727.
- [3] BRUNETTI A., GOLOSIO. B, **Software for X-ray fluorescence and scattering tomographic reconstruction**, ELSEVIER Computer Physics Communications 141, 2001, pp.412-425.
- [4] SCHROER. G. Christian et al., **High resolution element mapping inside biological samples using fluorescence micro-tomography**, Proceedings of the SPIE, Developments in X-Ray Tomography III, Bonse ed., 2002, vol. 4503, pp. 230–239.
- [5] MIQUELES. X. Eduardo, DE PIERRO. R. Alvaro, **C-library raft: Reconstruction algorithms for tomography; Applications to X-ray fluorescence tomography**, ELSEVIER, Computer Physics Communications 182(12), 2011, pp.2661-2673.
- [6] MENG. L. J., NAN Li, LA RIVEIRE. P. J., **X-ray fluorescence emission tomography (XFET) with novel imaging geometries - A Monte Carlo study**, IEEE Trans. Nucl. Sci. 58(6), December 2011, pp.3359-3369.
- [7] HENDEE R. William, RITENOUR E. Russel, **Medical imaging physics**, 4th ed., New York: Wiley-Liss, Inc., 2002.
- [8] Electromagnetic Spectrum figure, "*Lawrence Berkeley National Laboratory*. Web. 26 Apr.2012. <http://www.lbl.gov/MicroWorlds/ALSTool/EMSpec/EMSpec2.html>
- [9] SPRAWLS, Perry. **The physical principles of medical imaging X-ray production**, 2nd ed., USA: Medical Physics Publishing Corporation, 1995.
- [10] X-ray tube figure, Medical Encyclopedia: www.larousse.fr
- [11] PIPATSRISAWAT. T. et al., **Performance analysis of the filtered backprojection image reconstruction algorithms**, in Acoustics, Speech, and Signal Processing, March 2005, Proceedings ICASSP 05, vol. 5, pp. 153-156.
- [12] BUZUG. Thorsten M., **Computed Tomography, From Photon Statistics to Modern Cone-Beam CT**, Germany: Springer 2008, doi: 10.1007/978-3-540-39408-2.
- [13] GOLOSIO. Bruno, SIMIONOVICI. Alexander et al., **Internal elemental microanalysis combining x-ray fluorescence, Compton and transmission tomography**, Journal of applied physics, 2003, vol. 94, Issue 1, pp. 145, doi: org/10.1063/1.1578176.

- [14] DIETZEL. Knut Ingvald, **On-line X-ray fluorescence analysis applied to industrial processes and environmental monitoring**, Norway: University of Bergen, Department of Physics, October 2000.
- [15] CHEN. Z. W., WALTER. M. G., HUANG. H., **High Definition X-Ray Fluorescence: Principles and Techniques**, Hindawi Publishing Corporation, X-Ray Optics and Instrumentation, March 2008, vol. 2008, Article ID 318171, doi: 10.1155/2008/318171.
- [16] RANGER. T. Nicole, **Radiation Detectors in Nuclear Medicine**, 1999, Pubmed, Radiographics, vol. 19, Issue 2, pp. 481-502.
- [17] KNOLL, Glenn F., **Radiation Detection and Measurement**, 3rd ed., USA: John Wiley & Sons, Inc., January 2000.
- [18] KATSIKINI, M. Katsikini, E. C. Paloura, **X-ray Absorption Fine Structure, XAFS for Materials characterization**, Greece: Aristotle University of Thessaloniki, School of Physics, Department of Solid State Physics.
- [19] LEPY. Marie-Christine, **Total Efficiency calibration for coincidence-summing corrections**, Elsevier, Nuclear Instruments and Methods in Physics Research Section A, 2007, vol. 579, Issue 1, pp. 284-287, doi: 10.1016/j.nima.2007.04.081.
- [20] **Radiation measurement, Detection Efficiency**, Britannica Encyclopedia: www.britannica.com
- [21] SUETENS. Paul, **Fundamentals of Medical Imaging**, 2nd ed., USA: New York, Cambridge University Press, 2009.
- [22] CESAREO Roberto, BRUNETTI Antonio, **X and γ -Ray Tomography for Non-Destructive material testing**, Proceedings of the SPIE, Developments in X-Ray Tomography II, 1999, vol. 3772, pp. 292, doi: 10.1117/12.363732.
- [23] KAK, Avinash C., SLANEY. Malcolm, **Principle of Computerized Tomographic Imaging**, USA: New York, IEEE Press, Inc., 1989.
- [24] PEREIRA. R. Gabriela, LOPES. T., **X-ray fluorescence microtomography in biological applications**, Elsevier, 2007, Nuclear Instruments and Methods in Physics Research A 580, pp.951-954.
- [25] CHARBONNIER. Pierre et al., **Deterministic Edge-Preserving Regularization in Computed Imaging**, IEEE Transactions on Image Processing, 1997, vol. 6, no. 2, pp. 298-311.
- [26] BRUYANT. Philippe, **Analytic and Iterative Reconstruction Algorithms in SPECT**, The Journal of Nuclear Medicine, October 2002, vol. 43, No 10.
- [27] SAKARI. Alenius, RUOTSALAINEN. U., **Bayesian Image Reconstruction for Emission Tomography based on Median Root Prior**, European Journal of Nuclear Medicine, March 1997, vol. 24, pp. 258-265.
- [28] SMITH. Steven, **The scientist & Engineer's guide to Digital Signal Processing: Special Imaging Techniques/Computed Tomography**, San Diego, California Technical Publishing, 2002.
- [29] GROCH. MW, ERWIN. WD., **SPECT in the year 2000: basic principles**, Journal of Nuclear Medicine Technology, December 2000, vol. 28, pp. 233-244.

- [30] KRIZ. Ronald D. et al., **Parallel Implementation of the Filtered Back-projection algorithm for tomographic imaging**, © Copyright Raman Rao.
- [31] ZENG. G.L., **Image Reconstruction – a tutorial**, Pergamon, Computerized Medical Imaging and Graphics, 2001, vol. 25, pp. 97-103.
- [32] WERNICK. Miles, AARSVOLD. John, **Emission Tomography, the Fundamentals of PET and SPECT**, USA: California, UK: London, Elsevier Academic Press, 2004, Chapter 20 & 21.
- [33] KING. Micheal, GLICK. Stephen, **Attenuation, Scatter, and Spatial Resolution Compensation in SPECT**, book chapter in: WERNICK. Miles, AARSVOLD. John, **Emission Tomography, the Fundamentals of PET and SPECT**, USA: California, UK: London, Elsevier Academic Press, 2005, Chapter 22, pp. 74-89.
- [34] ERDOGAN. Hakan, FESSLER. Jeffrey, **An Ordered Subsets Algorithm for Transmission Tomography**, Physics in Medicine & Biology, December 1999, vol. 44, no. 11, pp. 2835, doi: 10.1088/0031-9155/44/11/311.
- [35] REILHAC Anthonin et al., **Simulation-based evaluation of OSEM iterative reconstruction methods in dynamic brain PET studies**, Elsevier, NeuroImage, 2008, vol. 39, pp. 359-368.
- [36] BOURKE. Paul, **Determining whether a line segment intersects a 3 vertex facets**, <http://astronomy.swin.edu.au/phourke/geometry/sphereline/> (Web page consulted on January 8th 2008).
- [37] VINEGONI. Claudio, **High Throughput Transmission Optical Projection Tomography Using Low Cost Graphics Processing Unit**, Optics Express 22322, December 2009, vol. 17, No. 25.
- [38] LEWERENZ. Marius et al., **Quantum Simulations of Complex Many-Body Systems: From Theory to Algorithms**, Germany: John von Neumann Institute for Computing, NIC Series, Lecture notes, 2002, vol. 10, pp. 1-24.
- [39] AY. M.R. ; GHAFRAIN. P. ; ZAIDI. H. , **A hybrid approach for fast simulation of Xray computed tomography**, IEEE, Nuclear Science Symposium, NSS '07, 2007, vol. 4, pp. 3155-3160.
- [40] DUVAUCHELLE. P., FREUD N., KAFTANDJIAN. V., BABOT D., **A Computer Code to simulate X-Ray Imaging Technique**, Nuclear Instruments and Methods in Physics Research B170, pp. 245-258, 2000.
- [41] CHUKALINA. M., SIMIONOVICI. A., **Quantitative characterization of microsamples by X-ray fluorescence tomography**, John Wiley & Sons, Ltd., X-Ray Spectrometry, December 2002, vol. 31, Issue 6, pp. 448-450.
- [42] BUZUG. Thorsten M., **Computed Tomography, From Photon Statistics to Modern Cone-Beam CT**, Germany: Springer 2008.
- [43] DESAI. Shrinivas D., KULLARNI. Lingangouda, **A quantitative comparative study of analytical and iterative reconstruction techniques**, International Journal of Image Processing (IJIP), January, 2010, vol. 4: Issue 4.
- [44] LOUDOS. GK, **An efficient Analytical calculation of probability matrix in 2D SPECT**, Comput Med Imaging Graph (2007) doi:10.1016/j.compmedinag.2007.08.003.

- [45] JOHNSON J. R., **Introduction to Digital Signal Processing**, 4th ed., India, Prentice-Hall of India Private Limited, pp. 85-95, 1997.
- [46] BURNS Marshall, **Automated Fabrication: Improving Productivity in Manufacturing, StereoLithography Interface Specification: 3D Systems**, USA: Prentice Hall, July 1993, section 6.5.
- [47] HAMAWY L., HASSAN W., BARRE S. and LEGOUPIL S., **Development of an Accelerated High Resolution Simulation Code for X-Ray Fluorescence Tomography**, Journal of Electrical Engineering, December 2013, vol. 1, no. 1, 10 pages.